An InGaAlAs-InGaAs two-colour detector, InAs photodiode and Si SPAD for radiation thermometry

Xinxin Zhou

A thesis submitted for the degree of Doctor of Philosophy

Department of Electronic and Electrical Engineering
The University of Sheffield

November 2014

Acknowledgement

I would like to thank my supervisor, Prof. Chee Hing Tan for giving me the opportunity to research on avalanche photodiode in University of Sheffield and his encouragement, guidance and advice throughout my MSc and PhD life. I have also benefited a lot from Dr. Pin Jern Ker and Dr. Ian Sandall for offering experience and suggestions in fabrication and characterisation of InAs photodiode. I am grateful to Prof. John David and Dr. Jo Shien Ng for sharing their expertise and mentoring support during the project years. I sincerely thank Dr. Shiyong Zhang and Dr. Andrey Krysa for their effort in wafer growth.

I appreciate time spent by Dr. Ken Kennedy and Dr. Rob Airey for training of equipment operation and suggestions in device fabrication. I would also like to express my gratitude to the Department of Electronic and Electrical Engineering Department and EPSRC for my research funding.

I would thank Dr. Shiyu Xie, Dr. Jingjing Xie, Dr. James Green, Dr. Jennifer Ong, Dr. Rajiv Gomes, Dr. Perter Vines, Dr. Yu Ling Goh, Dr. Daniel Ong, Dr. Siewli Tan, Dr. Rahman Mohmad, Dr. Matthew Hobbs, Xiao Meng, Syahrin Idris, Simon Dimler, Benjamin White, Akeel Auckloo, Jeng Shiuh Cheong, Liang Qiao for their useful conversations and friendship and my gratitude also go out to Dr. Siming Chen, Dr. Kejia Zhou and Xiao Jin for bringing joy and hope in Sheffield.

Last but not least, it has been my fortune to meet my boyfriend in Sheffield and deeply appreciate the love and support from him. I am indebted to my parents, sister and brother for their truly immense love and continuous support during my PhD life.

Abstract

This work aims to develop infrared detectors and to introduce a new measurement technique for infrared radiation thermometry. It consists of two-colour detectors for ratio thermometry, InAs photodiode for 3.43 μm narrow band thermometer and photon counting thermometer using a Si single photon avalanche photodiode (SPAD). In addition to research in these detectors, a Monte Carlo model for modelling impact ionisation in Si was also developed.

InGaAlAs is attractive material for multi-colour detection at wavelengths up to 1.7 μm, as it is lattice matched to InP substrate. InGaAlAs-InGaAs two-colour detector was evaluated as a ratio thermometer. When compared to a commercial Si-InGaAs detector, the InGaAlAs diode produces slightly higher (lower) output than Si at temperature below (above) 500 °C, while the InGaAs diode in this work also produces slightly higher output than that in the commercial Si-InGaAs detector. The InGaAlAs and InGaAs diodes detect blackbody temperatures as low as 275 and 125 ^{o}C, respectively, with signal to noise ratios (*SNR*s) above 10. As a ratio thermometer, the two-colour InGaAlAs-InGaAs photodetector achieves a temperature error of 12.8 °C at 275 °C, but this improves with temperature to 0.1 °C at 450 °C. If the maximum temperature error of 2 °C is defined, the InGaAlAs-InGaAs is capable of detecting an object temperature down to 325 °C. These results demonstrate the potential of InGaAlAs-InGaAs two-colour photodetector for development of high performance two-colour array detectors for radiation thermometry and thermal imaging of hot objects.

The InAs photodiode offers huge potential for infrared sensing applications at wavelengths above 1.7 μm. The performance of InAs photodiode was evaluated for use in radiation thermometry at wavelengths beyond InGaAs photodiode. For uncooled InAs, it successfully measured a blackbody temperature of 50 ^{o}C with an acceptable error of 0.17 ^{o}C. In order to evaluate its performance as a 3.43 μm narrow band thermometer, measurements were repeated with a narrow band filter. InAs was demonstrated to have lower temperature error than a commercial PbSe detector. The temperature error was 1.88 ^{o}C for InAs at 50 ^{o}C compared to 3.78 ^{o}C for PbSe. This suggests that InAs is ideally

suited for applications requiring 3.43 μm operating wavelength. Further improvement was achieved by cooling InAs to 200 K. It was found that a temperature as low as 37 ^{o}C, with an error of less than 0.5 ^{o}C, can be measured indicating its potential for human body temperature sensing.

An alternative to using a photodetector with longer wavelength response is to increase the sensitivity of the photodetector via internal gain mechanisms such as impact ionisation. By employing a very high internal gain in SPAD, the photon counting technique was evaluated for radiation thermometry. Photon induced avalanche pulses were successfully measured at temperature as low as 225 ^{o}C with an error less than 2 ^{o}C using Si SPAD. This is significantly lower than the lower temperature limit of 400 ^{o}C in conventional Si photodiode based radiation thermometer. The photon counting technique is therefore demonstrated to be a feasible technique to achieve lower temperature sensing.

Following the promising results obtained using Si SPAD in this work and Si APD in a recent literature, a Simple Monte Carlo model was developed to model the avalanche characteristics of Silicon. Good agreement with experimental results from Silicon p^{+}-i-n^{+} diodes with i-regions ranging from 0.082 to 0.26 μm, an n^{+}-i-p^{+} diode with an i-region of 0.82 μm and a $p^{+}n$ diode was obtained. The derived ionisation coefficients is also comparable to that derived from the local model. Therefore this model can be used to model the avalanche process in diodes with varying electric field profiles such as those in Si APDs and SPADs. Under a SPAD operation, this model can accurately predict the ballast resistor effect, indicating that this is an effective tool for APD and SPAD design.

List of publications

Journal Publications

1. **X. Zhou**, M. J .Hobbs, B. S. White, J. P. R. David, J. R. Willmott and C. H. Tan, "An InGaAlAs-InGaAs two colour photodetector for ratio thermometry," *IEEE Trans. Electron Devices*, vol. 61, no. 3, pp. 838-843, Mar. 2014.

2. **X. Zhou**, J. S. Ng and C. H. Tan, "A simple Monte Carlo model for prediction of avalanche multiplication process in Silicon," *Journal of Instrumentation*, vol. 7, no. 8, pp. P08006, Aug. 2012.

3. M. J. Hobbs, C. H. Tan, **X. Zhou**, J. P. R. David, J. R. Willmott, S. Krishna and E. Plis, "InAs/GaSb type-II superlattice for radiation thermometry," *accepted for publication in IEEE transaction of instrumentation and measurement* on 19th June 2014.

4. **X. Zhou**, X. Meng, B. S. White, J. S. Ng and C. H. Tan, "InAs photodiodes for 3.43 μm narrowband radiation thermometers," in preparation for submission.

Conference publications

1. **X. Zhou**, J. S. Ng and C. H. Tan, "Temperature dependence of radiation thermometry of InAs photodiodes," *UK compound semiconductors conference*, Sheffield, UK, July 2014.

2. I. Sandall, B. S. White, **X. Zhou** and C. H. Tan, "An InAs/QDIP multispectral detector," *UK compound semiconductors conference*, Sheffield, UK, July 2014.

3. **X. Zhou**, I. Sandall, B. S. White, A. B. Krysa, J. R. Willmott and C. H. Tan, "InAs photodiode for 3.43 μm radiation thermometer," *41th International Symposium on Compound Semiconductors (ISCS)*, Montpellier, France, May 2014.

4. I. Sandall, **X. Zhou**, X. Meng, A. B. Krysa, S. Zhang and C. H. Tan, "Development of high efficiency and uniform InAs APDs for imaging applications," *41th International Symposium on Compound Semiconductors (ISCS)*, Montpellier, France, May 2014.

5. **X. Zhou** and C. H. Tan, "InAsSb mid-IR detector for room temperature operation," *UK compound semiconductors conference*, Sheffield, UK, July 2013.

6. B. S. White, I. Sandall, **X. Zhou**, C. H. Tan, J. R. Willmott and A. B. Krysa, "Single pixel thermal imaging using an InAs photodiode," *UK compound semiconductors conference*, Sheffield, UK, July 2013.

7. C. H. Tan, I. Sandall, **X. Zhou**, B. S. White, M. Hobbs, S. Zhang, A. B. Krysa and J. P. David, "Mid-IR detectors at Sheffield," *UK compound semiconductors conference*, Sheffield, UK, July 2013.

8. **X. Zhou**, I. Sandall, M. J. Hobbs, B. S. White, C. H. Tan and J. R. Willmott, "Evaluation of InAs photodiodes for radiation thermometry," *27th Meeting of the Semiconductor and Integrated Optoelectronics (SIOE)*, Cardiff, UK, 2013.

9. **X. Zhou**, S. Xie and C. H. Tan, "APD designs for gain-bandwidth product above 200GHz", *UK compound semiconductors conference*, Sheffield, UK, July 2011.

10. S. Xie, A. S. Idris, **X. Zhou** and C. H. Tan, "$AlAs_{0.56}Sb_{0.44}$ avalanche photodiode with an extremely small temperature coefficient of breakdown voltage", *38th International Symposium on Compound Semiconductors (ISCS)*, Berlin, Germany, 2011.

11. S. Xie, J. Xie**, X. Zhou**, P. J. Ker and C. H. Tan, "$AlAs_{0.56}Sb_{0.44}$ avalanche photodiode with weak temperature dependence", *25th Meeting of the Semiconductor and Integrated Optoelectronics (SIOE)*, Cardiff, UK, 2011.

Glossary of terms

$\alpha\,(\beta)$	Electron (hole) ionisation coefficient
α_T	Tunnelling factor
γ	Ionisation rate softness factor
ξ	Electric field
λ	Wavelength
λ_p	Peak response wavelength
λ_m	Mean free path length between scatterings
λ_e	Effective operation wavelength in ratio thermometer
c	Speed of light
ε	Emissivity
ε_0	Permittivity of vacuum
ε_r	Relative permittivity of dielectric
σ	Stefan-Boltzmann constant
η	Quantum efficiency
τ_{eff}	Effective life time
ν	Frequency of light
φ	Radiation incident angle
θ	Optical field of view
θ_i	Incident angle
θ_d	Diffractive angle
$\hbar\omega$	Photon energy
Γ_t	Scattering rate
Θ	Non-parabolic parameter
c_2	Second radiation constant
f	Frequency
f_c	Focal length
d	*G*roove spacing in a grating
$h\,(\hbar)$	Planck constant
k	Ionisation coefficient ratio

k_B	Boltzmann constant
l	Diffraction order
m_o	Free electron mass
m^*	Effective mass
n_i	Material intrinsic carrier concentration
q	Electron charge
t_d	Drift time
w	Depletion region width
w_s	Entrance or exit slit width
Φ	Input photon flux
$\%/^oC$	Percentage-per-degree
A	Area
ABMC	Analytical band Monte Carlo
APD	Avalanche photodiode
B	Bandwidth
BP	System bandpass
BST	Barium strontium titanate
C	Capacitance
C_d	Diode capacitance
C_{ii}	Coefficient for impact ionisation rate
C_I	Instrument factor
C-V	Capacitance-voltage
CB	Collisional broadening
CW	Continuous wave
D^*	Detectivity
D_n (D_p)	Diffusion coefficients of electron (hole)
DCR	Dark count rate
DIW	Deionised water
DUT	Device under test
E	Carrier energy
EQE	External quantum efficiency
E_g	Energy gap
E_{th}	Impact ionisation threshold energy

F	Excess noise factor
FBMC	Full band Monte Carlo
F_c	Optical chopper factor
FFT	Fast Fourier Transform
FTIR	Fourier transform IR
FPA	Focal planar array
G_0	Generation rate of photocarriers
$<G^2>$	Mean value of squared multiplication factor
$<G>^2$	Squared mean multiplication factor
$<i_S^2>$	Spectral shot noise current density
$<i_T^2>$	Spectral thermal noise current density
I_F	Forward current
I_o	Saturation current
I_a	Peak avalanche current
I_b	Current from absorption of background radiation
I_d	Dark current
I_{diff}	Diffusion current
$I_{g\text{-}r}$	Generation recombination current
I_{ph}	Photocurrent
I_{pr}	Primary photocurrent
I_s	self-sustaining current
I_{tunn}	Tunnelling current
I-V	Current-voltage
IPA	Isopropyl alcohol
IR	IR
J_{diff}	Diffusion current density
J_{dr}	Drift current density
J_{tt}	Total current density
K	Wave vector
L_d	Minority carrier diffusion length
$L_{b,\lambda}(\lambda,T)$	Emissive power from the blackbody at wavelength of λ and temperature of T
L_B	radiated energy from a blackbody at temperature T per unit are

L_n (L_p)	Debye length for electron (hole)
LIA	Lock-in amplifier
LWIR	Long-wave IR
M	Mean avalanche gain
MCT	HgCdTe
M_e (M_h)	Avalanche gain due to electron (hole) injection
MBE	Molecular beam epitaxy
MOCVD	Molecular organic chemical vapour deposition
MWIR	Mid-wave IR
N	Doping concentration
N_D (N_A)	Donor (acceptor) impurity concentration
NEP	Noise equivalent power
N_F	Phonon occupation factor
NIM	Nuclear instrument modules
NIR	Near IR
NETD	Noise-equivalent temperature difference
P_b	Breakdown probability
P_{opt}	Power of incident light
$P(\lambda)$	Incident power of per unit wavelength radiation
pdf	Probability density function
PC	Photoconductive
PCR	Photon count rate
PDE	Photon detection efficiency
PMT	Photomultiplier tube
PQC	Passive quenching circuit
PSD	Phase sensitive detection
PV	Photovoltaic
QKD	Quantum key distribution
QWIPs	Quantum well IR photodetectors
R_{ab} (R_{em})	Effective phonon scattering rates for phonon absorption (emission)
R_s	Series resistance
R_b	Ballast resistance
R_d	Diode resistance

R_{eq}	Equivalent resistance of device
R_{ii}	Impact ionisation rate
$R(\lambda)$	Responsivity at wavelength of λ
$\mathcal{R}_p$	Peak responsivity
RMS	Root mean Square
RPM	Revolution per minute
S_λ	Output photocurrent from spectral radiation thermometer
S_n	Occurrence probability of n_{th} scattering mechanism
SNR	Signal to noise ratio
SA	Spectrum analyser
SLS	Superlattices
SMC	Simple Monte Carlo
SMU	Source measurement unit
SPAD	Single photo avalanche diode
SWIR	Short-wave IR
T	Temperature
T_f	Transmission factor of the system
T_{BB}	Temperature of the blackbody
T2SLs	Type-II superlattices
TCR	Total count rate
V	Voltage
V_{bd}	Breakdown voltage
V_{bi}	Build-in potential
V_d	Diode voltage
V_o	Output voltage
V_{pp}	Peak to peak voltage
UV	Ultraviolet
VLWIR	Very long-wave IR
VLSI	Very large scale integration

Contents

Chapter 1 Introduction

1.1 Infrared Radiation

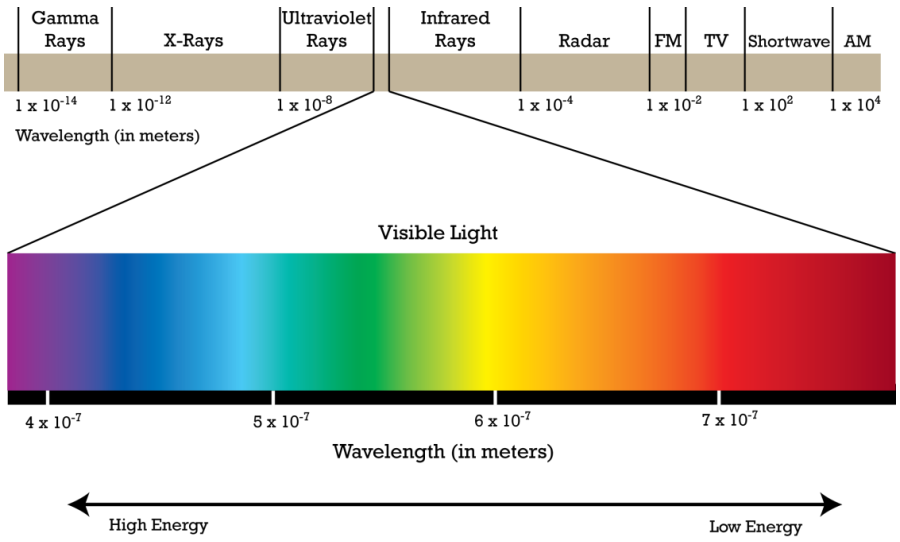

Figure 1.1 The electromagnetic spectrum [1]

The wave-particle duality describes light as a collection of photons propagating through a medium as electromagnetic wave. Light can be characterised by the frequency, f or wavelength, λ, which are related by

$$f = \frac{c}{\lambda} \tag{1.1}$$

where $c = 3\times10^8$ m/s is the speed of light. The electromagnetic spectrum covers high frequency component such as gamma ray to low frequency radio waves in communication system, as shown in Figure 1.1. In this work, the infrared (IR) spectrum is of particular interest.

IR refers to electromagnetic waves which beyond the visible light and below microwave, corresponding to λ = 700 nm - 1 mm. IR radiation is further divided into three wavelength bands: near-IR (NIR) (0.7 μm - 1.0 μm), short-wave IR (SWIR) (1 μm - 3 μm), mid-wave IR (MWIR) (3 μm - 5 μm), long-wave IR (LWIR) (8 μm - 14 μm) and far-IR (14 μm - 1 mm).

All the objects with a temperature above absolute zero absorb and emit IR light. An ideal absorber or emitter known as blackbody source, can absorb all the incident IR energy on its surface. The emitted energy per unit wavelength and per unit area from a blackbody follows the Planck's equation [2]

$$L_{b,\lambda}(\lambda, T_{BB}) = \frac{2\pi c^2 h}{\lambda^5 \left(e^{\left(\frac{hc}{\lambda k_B T_{BB}}\right)} - 1 \right)} \quad W/m^3 \tag{1.2}$$

where T_{BB} is the temperature of the blackbody in Kelvin, $h = 6.626\times10^{-34}$ J·s is the Planck constant, k_B is the Boltzmann constant. The power radiated by the blackbody increases with temperature shown in Figure 1.2. As temperature T increases, the peak of the spectrum shifts to shorter wavelength. The shift is given by Wien's displacement law

$$\lambda_p T = 2897.8 \quad \mu\text{m. K} \tag{1.3}$$

This provides a simple guide for the choice of photodetectors that can be used to measure the temperature of an object via IR radiation, also known as radiation thermometry.

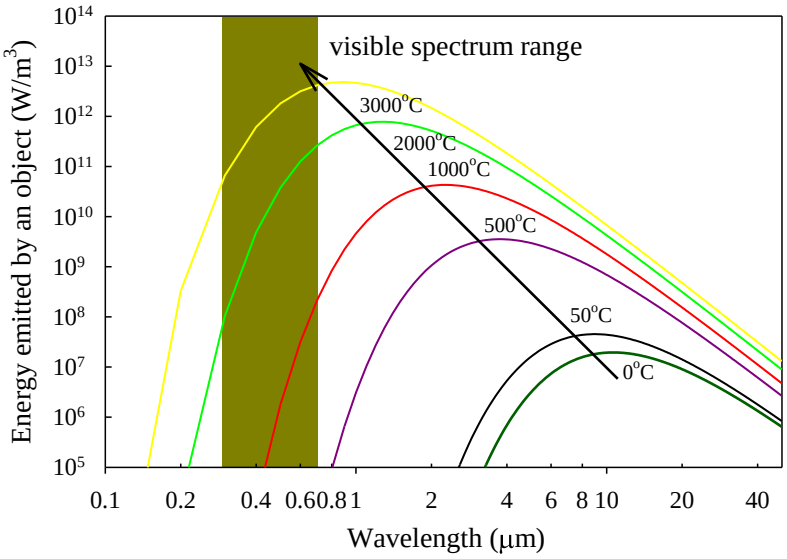

Figure 1.2 Emitted energy, calculated using Planck's Law, as a function of wavelength for different blackbody temperatures

Thermography or thermal imaging also measure the emitted IR radiation. Most thermal cameras operate in the IR spectrum in 0.9 – 14 μm range, which transmit well through the air, to provide temperature profile of the object. Therefore thermal imaging is extensively used for military purposes, which includes target acquisition, night vision and surveillance. IR radiation measurement also plays key role in industry applications

including environmental monitoring and facility inspections, and other uses such as spectroscopy and remote temperature sensing.

IR spectroscopy is a technique to study the matter and radiation intensity. It mainly used to identify chemicals. As each chemical bond or molecule will resonate at specific frequencies, it absorbs these frequencies to produce IR absorption spectrum that represents the chemical bond. The instruments implementing this technique are called IR spectrometers, which are used to characterise solids, gases and liquids. The most common laboratory instruments using this technique are Fourier transform IR (FTIR) spectrometers and monochromators.

Night vision systems convert IR light to electrical signal to provide better image in cases where there is insufficient visible light or no visible light. By detecting the thermal radiation from the objects, thermal imaging is an efficient tool for night vison without requiring illumination such as in active imaging. As there are a wide range of applications that rely on temperature sensing, the detectors for temperature sensing will be the focus of this work.

1.2 Temperature measurement

1.2.1 Concept of temperature

Today, temperature measurement is an essential component in material processing [3], manufacturing and remote sensing [4]. The first interpretation of temperature was by associating it with sensations of hot or cold. However, the more precise temperature scale was only used when Galileo invented the first air thermoscope (relying on the change of liquid level in a tube as temperature changes) in 1592. In 17th century, extensive studies on thermometers were carried out, with better accuracy introduced through Fahrenheit and Celsius temperature scales in 1724 and 1742, respectively. These were the preferred units until 19th century, when the absolute thermodynamic scale, Kelvin, was introduced by Lord Kelvin. Since then Kelvin is the preferred unit for temperature measurement in metrology.

Many techniques for temperature measurement have been developed. These can be classified as contact measurement and non-contact measurement. The contact thermometer measures the change of a physical property via a direct contact between the sensor and the object. These thermometers include glass thermometer, thermocouples and thermistors.

The most common non-contact thermometer measures the radiated photons and correlate it to a temperature via Planck's law. This technique is called radiation thermometry and is widely used in applications involving fast measurement, measurement on non-accessible target due to extremely high temperature or prevent contamination because of its high precision. The high precision is achieved through optimisation of optical systems to cater for the requirements in different applications. In the following section, radiation thermometry will be described in more detail.

1.2.2 History of radiation thermometry development

Every object with a temperature above absolute zero can emit electromagnetic waves. When the object temperature approaches 600 ^{o}C, it emits visible light. As the object temperature increases, the emitted light colour changes from red to purple. Therefore the human eye was used as the first radiation thermometer. In 1892, French chemist Le Chatelier introduced the first optical pyrometer which was initially used for applications relating to cement manufacturing [5]. Following this, modifications were introduced in the optical pyrometers by other researchers including Holborn and Kurlaum, and Morse. A patent for the optical pyrometer was granted to Morse in 1899 who introduced the human eye as a temperature sensor to compare the brightness of object with that emitted energy from a tungsten wire in front of the object in the thermometer. It is known as disappearing-filament optical pyrometers [6]. In this pyrometer, the thin wire in front of object will be heated by a current. The user then compare the wire brightness under different currents with the object. Once the wire achieves the same brightness as object, the object temperature can be determined from pre-determined calibration scale. It is very useful for high temperature measurement and had been used until 1940s [7]. However due to the limited sensitivity of human eye, the disappearing-filament pyrometer is restricted to objects with high temperature above 600 ^{o}C which can emit visible light and with high emissivity (see section 2.1). Furthermore, the accurate measurement using this

pyrometer relies heavily on the skilled user to achieve a good control. Therefore, other pyrometers have been developed as a more efficient temperature measurement instrument.

From 1950s, photomultipliers were used as physical sensors to calibrate optical pyrometers. This type of optical pyrometers are based on the photoelectric effect and secondary electron emission [8]. Photoelectric pyrometers were developed to replace those disappearing-filament optical pyrometers in standards laboratories. From 1980s, semiconductor detector based radiation thermometer was developed for non-invasive temperature measurement [9].

Nowadays, semiconductor photon and thermal detectors are widely used in radiation thermometers. Due to a wide range of available semiconductor detectors, radiation thermometers can be employed in temperature monitoring in steel, aluminium, food, glass and plastic industries. They have also been used in semiconductor processing and more advanced manufacturing in recent years.

1.3 Overview of Radiation thermometry

1.3.1 Design Considerations of radiation thermometers

A basic radiation thermometer consists of an optical system, detectors and signal processing unit as shown in Figure 1.3. The radiated energy from the hot object is measured to determine its temperature. The lens and aperture in the thermometer defines the field of view which determines the size of target that can be imaged by the detector, while the filter defines the measured spectral region of the thermal radiation. The output signal from the detector is then amplified and converted to the temperature value by the signal processor. Each components should be optimised to maximise the accuracy in a given application.

The selection of the detector is one of primary considerations in designing a radiation thermometer. Several aspects of the detector, including response time, spectrum range and detector noise need to be considered. Thermal detectors and photon detectors are the two main types of detector used in radiation thermometry.

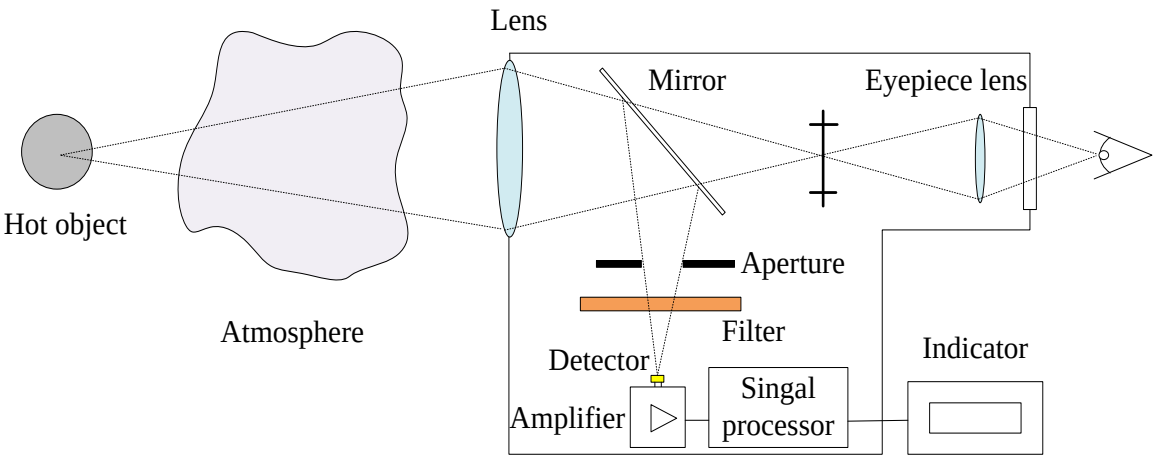

Figure 1.3 the basic schematic of a radiation thermometer

The thermal detectors, such as thermopiles, bolometers and pyroelectric, can respond to radiation over a broad spectrum, thus can detect to low temperature range down to -100 ^{o}C [10,11]. Thermopiles are composed of several thermocouples in series. They measure the voltage generated due to a temperature change of a junction built from two dissimilar metal contacts. A bolometer absorbs emitted energy from a target, which changes its resistance and the corresponding temperature value can be extracted. Both thermopiles and bolometers can be operated in the DC mode. Due to lower sensitivity shown in Figure 1.4, they can be employed in thermometers with lower accuracy and no optical modulation requirement. Pyroelectric translates the temperature to a change in charges. Therefore by measuring the capacitance the temperature can be obtained. However, the incident radiation must be chopped and the output needs to be read out using a high impedance circuit. These can be used when the optical chopper is acceptable to achieve high accuracy in the measurement.

Since all these thermal detectors employ a wide band absorbent materials, thermal detectors can response to radiation across a broadband, with the output only dependent on incident radiation power. Thus they can operate at room temperature without cooling to achieve satisfactory performance. A useful figure of merit to compare the performance of detector is the detectivity (see details in section 2.3.1), defined as the reciprocal of noise-equivalent power (*NEP*), multiplied by square root of the detector area and bandwidth.

Thermal detectors have low detectivity and need to achieve thermal equilibrium, when responding to temperature changes of targets, leading to long response time. Hence, they are not suitable for high speed measurements.

Instead of heating up a material in response to incident radiation, photon detectors experience an electronic state change when the incident wave is absorbed. Either working in a photovoltaic or photoconductive mode, the incident photons excite carriers in the detectors, changing the current or resistance, respectively. Unlike the thermal detectors, the photon detectors have a limited response range dependent on the band gap energy of the materials. Photon detectors present much faster response speed and higher detectivity than thermal detectors. Figure 1.4 shows the spectral response and detectivities for the commonly used IR detectors. Although photon detectors have a limited detection range, most thermometers still use photon detectors rather than the thermal detectors because the output loss due to restricted detection range is compensated by the higher detectivity.

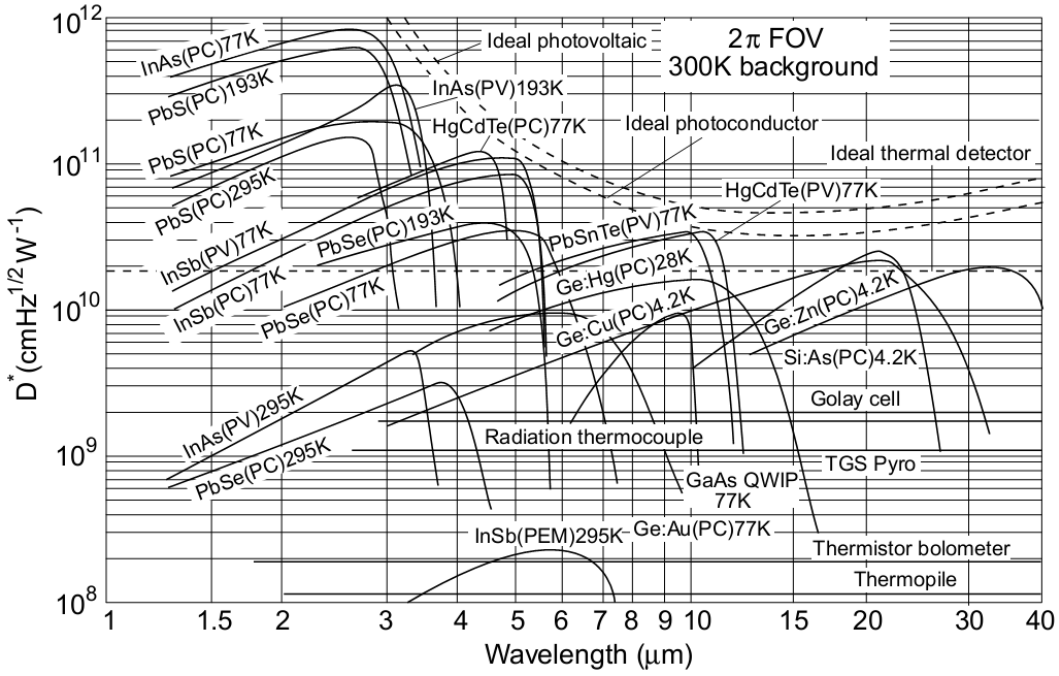

Figure 1.4 Comparison of detectivity for various commercially available thermal detectors and IR photon detectors [12]

In practice, there is no perfect blackbody. All objects emit less energy than the blackbody, thus a factor of emissivity is included to quantify the emitted energy. To achieve an accurate temperature measurement, the object should not be transparent or have high reflection. Otherwise, most of incident wave will be transmitted or reflected by the object

and thus the absorbed or emitted power of the object will be extremely low to perform accurate measurement. A major challenge in radiation thermometry is the uncertainty of target emissivity which depends on the material physical property and its surface conditions. The background radiation and attenuation along the sight path as illustrated in Figure 1.3, are also factors that can introduce errors. However, these can be solved using a well-designed radiation thermometer incorporating multi-wavelength measurement using different bandpass/narrow band filters or multi-junction photodetectors. For instance in dual-wavelength thermometers, the measurement only depends on the ratio of energies at the chosen wavelengths and it can reduce the emissivity problem significantly. Narrow band filters can also be used to define the measured spectral range where the object could have no reflection and is opaque. More details are provided in the following section.

1.3.2 Types of radiation thermometers

Broadband thermometers, also known as total radiation thermometers, measure a significant fraction of radiation emitted by the target. Depending on the lens and windows used, it detects photons with wavelengths from 0.3 μm to an upper cut-off wavelength ranging from 2.5 to 20 μm [10].

Unlike broadband thermometer, bandpass thermometer only detects a specific part of spectrum and is particular useful for measuring the temperature of different materials. In glass industry, 5-7 μm spectrum range was widely used to sense glass temperature as glass will transmit or reflect some energy at other wavelengths range [10]. The 8-14 μm bandpass was always chosen for low temperature sensing below room temperature [11].

Narrow band thermometers measure the temperature over a narrow spectrum. Such narrow spectral range either depends on the selected detector or the use of narrow band filters. These thermometers are used in the industry process for specific temperature range of interest. For high temperature sensing above 600 ^{o}C, Si detectors operating at 0.9 μm are used [3]. In plastic industry, most of plastics show a strong absorption band at 3.43 μm due to the hydrogen to carbon molecular bonds (C-H bonds) or at 7.92 μm where the plastics contain strong carbon to oxygen molecular bonds (C-O bonds) [11].

Consequently, narrow band filters with an operation wavelength at 3.43 μm or at 7.92 μm are employed in thin film plastics processing.

Ratio thermometers measure the emitted energy from target at two narrow bands and derive the target temperature by calculating the ratio of the absorbed radiation. As the temperature only depends on the ratio, this technique can reduce or eliminate the effect of changes in emissivity due to attenuation for obscured path or vapour absorption, provided the attenuation factors are the same at both wavelengths.

Fibre optic thermometers are thermometers employing a flexible optical fibre to guide the radiation from target to the detectors. The radiation spectral response depends on the fibre materials, but can achieve measurements down to 100 ^{o}C [10]. Fibre optic thermometers are useful in the situations where it is difficult or impossible to obtain a clear line of sight or to measure temperatures of small targets [10].

1.4 Existing detectors for radiation thermometry

For radiation thermometers, appropriate detectors are chosen for desired wavelength ranges. A comparison of some commonly used detectors in the thermometers is presented in Table 1.1. With a high detectivity and fast response, photon detectors are preferred as they can work at wavelength ranges to achieve high temperature resolution. This section will discuss some of the most popular photon detectors in radiation thermometers.

Table 1.1 Detectors used in the radiation thermometers

Detectors type	Material	Wavelength, μm
Photon detectors	Si	0.9
	Ge	1.7
	InGaAs	1.7/2.6
	PbS	2.5
	PbSe	4
	InSb	5
	HgCdTe	1-20
Thermal detectors	Pyroelectric	Up to 20
	Thermopiles/bolometers	Up to 20

1.4.1 Si and Ge photodiodes

Si photodiode, is a mature and cheap device that is widely used as a sensor in radiation thermometer. Due to a cut-off wavelength of 1.1 μm, its performance is restricted to measurement above 400 ^{o}C [11]. Ge detectors are employed in commercial thermometers detecting down to 250 ^{o}C due to its extended wavelength range up to 1.6 μm [13]. However, it suffers from high thermal noise which limits its lower temperature limit.

1.4.2 InGaAs photodiodes

A standard InGaAs photodiode, lattice matched to InP, is another candidate with a similar cut-off wavelength to Ge. It is more attractive in many applications such as radiometry and thermal imaging due to its lower noise and weaker temperature dependence performance [14]. With a high responsivity between 0.9 μm to 1.7 μm, InGaAs is an outstanding optical receiver in optical communication system [15]. Similarly, it is also used in a radiation thermometer to sense temperature down to 150 ^{o}C [16,17]. However, for lower temperature measurement, detectors with longer cut-off wavelengths should be used to collect more radiated power to achieve sufficient resolution. Sakuma *et al*. [18] developed an InGaAs thermometer for sensing temperature between 100 ^{o}C to 600 ^{o}C by using a cooled extended InGaAs (by increasing the In composition to reduce the band gap) detector, working at a wavelength of 2 μm. An extended InGaAs sensor operating at 2.3 μm has also been adopted in a commercialised thermometer to detect temperature down to 50 ^{o}C [19]. By changing the alloy composition during the growth and optimisation in fabrication process, InGaAs can be used to detect IR radiation up to 2.6 μm. Yoon *et al*. [20] demonstrated that an extended InGaAs with a 2.5 μm cut-off wavelength can be used to sense a 50 ^{o}C target with a noise-equivalent temperature difference (NETD) < 3 mK. The NETD relates to minimum resolvable temperature difference which is a measure of the sensitivity of a detector of thermal radiation. However, a longer response wavelength results in a lower shunt resistance which leads to higher thermal noise. In order to achieve the required performance, a thermo-electric cooler is needed to reduce detector noise in this application.

1.4.3 Lead salts detectors

Lead salts are the next group of photon detectors developed to sense mid-IR radiation in broad band applications. PbSe thin film photoconductors were first fabricated in Germany in 1944 and later were used in a system to detect hot aircraft engine emissions [21]. After that, intensive effort to develop lead salt detectors for applications in war, communications and search and rescue systems [22]. Currently, low cost PbS and PbSe photoconductors are still some of the best choices for applications working 1-3 μm and 3-5 μm spectral range [22]. These still occupy most of market in IR detectors. Hamamatsu and Judson Technology provide both room temperature and cooled PbS and PbSe photoconductors. PbS and PbSe detectors are widely used in a commercial radiation thermometer to sense temperature down to 80 ^{o}C and 30 ^{o}C [23], respectively. However, lead salt detectors have higher dielectric constant compared with other photodiodes, such as Si, Ge, InGaAs and InSb [24,25]. It suffers from low response time and high 1/f noise, making them unsuitable for high speed applications [26]. Furthermore, due to growth issues, commercial PbSe is limited to linear arrays and small FPA arrays (up to 80×80).

1.4.4 InSb detector

As the first developed III-V system material, InSb alloys have a small energy band gap of 0.17 eV and can be prepared in single crystal form to provide high performance in the wavelength region between 2 and 5 μm [27]. It can be operated in photovoltaic (PV) and photoconductive (PC) modes. Unfortunately, InSb detectors suffer from high dark current and needs to be cooled to liquid-nitrogen temperature. The peak detectivity of InSb at 5 μm is around 1×10^{11} cmHz$^{1/2}$/W at 77 K [28]. These high-performance InSb cooled detectors are also used in a radiation thermometer for medium and low temperature range [29,30]. It is most highly developed and used for focal plane array in MWIR cameras [31]. However, it has been found that InSb IR FPAs shows significant drift in the uniformity characteristics over time and cooling process, making them less attractive for measurement applications.

1.4.5 HgCdTe detector

The HgCdTe (MCT) detectors have been widely used for IR sensing applications. A unique benefit of this material system is the flexibility of spectral range covering from SWIR to VLWIR [32]. Due to high absorption coefficients, MCT devices can provide a

high quantum efficiency of 90 % when used with an anti-reflection coating layer. MCT devices can be operated as a photovoltaic devices sensing up to 20 μm or photoconductive devices with a detection range up to 25 μm. For IR imaging applications, MCT devices were optimised to work either at 3-5 μm or 8-14 μm due to atmospheric transmission.

However, MCT devices need cooling for high performance operation. For 3-5μm band operation, this can be optimised to work efficiently at temperatures as high as 195 K while it needs to be cooled down to liquid nitrogen temperature which is 77K in 8-14 μm bands [32]. The growth and fabrication challenges in MCT lead to low yield arrays and thus high cost.

1.4.6 Thermal detectors

Thermal detectors such as bolometers and pyroelectric detectors are widely used in radiation thermometers [33]. Both bolometer and pyroelectric detector arrays have been used for IR thermal imaging due to low cost and uncooled operation. Mostly, the bolometers operate at 8-14 μm wavelength range, but they can also work as 3-5 μm band detectors. Amorphous silicon is one of most advanced technologies for microbolometers due to fabrication in silicon foundry. Another popular material for fabrication of microbolometers is vanadium dioxide, VO_2 [34] which can also be fabricated by silicon foundries. A 640×480 FPA microbolometer arrays with NETD of below 50 mK have been reported by Altman at BAE systems [35]. The detectivity of bolometer is around 2×10^8 $cmHz^{1/2}/W$. Typically, the pyroelectric detector shows higher detectivity than the bolometers which is 1×10^9 $cmHz^{1/2}/W$. As it measures the temperature by a change in capacitance when responding to the absorbed radiation, the pyroelectric detector require optical modulation. This is a major limitation in many applications.

1.5 Other IR technologies

1.5.1 Multicolour detectors

Multicolour capability is highly desirable for advanced IR systems [36]. Based on the wavelength range of interest in MWIR, LWIR and VLWIR, three types of detector have

been developed: MCT, quantum well IR photodetectors (QWIPs) and type-II superlattices (T2SLs). Currently, both MCT and QWIPs are commercially available and have been demonstrated as detectors with multicolour capability.

Dual band detectors have been grown on the lattice matched CdZnTe substrates by molecular beam epitaxy (MBE). Raytheon Vision Systems has developed and produced a 1280×720 two-colour MWIR/LWIR FPAs with a 20 μm pixel size and cut-off up to 11 μm at 78 K [37]. These FPAs shows excellent performance with high sensitivity and pixel operability above 98% in both mid-wave and long-wave bands [37]. However drawbacks in CdZnTe, such as limited substrate size (<50 cm^2), high production cost and large difference in thermal expansion coefficient with silicon readout circuit, led to limited applications [36]. It is well known there are a lot of factors including low cost, availability of large area substrate and long-term thermal reliability when coupling Si readout circuit that make the use of Si substrate attractive in IR technology. Nowadays, MCT/Si detectors have been grown and can be obtained with comparable performance to that grown on CdZnTe substrates [38].

Quantum well IR photodetector is an alternative detector for MWIR and LWIR technology. Compared with MCT, GaAs/AlGaAs QWIPs presents many advantages. Mature manufacturing techniques based on GaAs technologies, high uniformity and large area FPAs are available, providing high yield, thus low cost reliable IR detectors. With respect to single pixel device, some fundamental limitations related to intersubband transition problem make it non-competitive with MCT, especially at temperatures above 70 K. For instance, QWIPs show a typically low quantum efficiency (<10%) and narrow spectral range with a full-width haft maximum of 15 %. This limitation in performance becomes less important at detector temperature below 50 K due to the rising problem from MCT such as trap-assisted tunnelling and interface instabilities. As they operate in the photoconductive mode, QWIPs suffers from low integration time application. However, QWIPs have better uniformity leading to large arrays. QWIPs can achieve comparable NETD but at 10-100 times longer integration time than that for MCT. QWIPs are used in large array formats with longer integration time and low frame rate. Gunapala *et al*. demonstrated 1024×1024 pixel MWIR and LWIR QWIP focal plane arrays [39].

The MWIR QWIP array has demonstrated a NETD of 17 mK at 95 K operation temperature while the LWIR array has shown a 13 mK at 70 K operation temperature.

As the QWIPs show narrow band spectrum, they are ideal detectors for multicolour detection with zero cross-talk achieved using different spectrum range with several μm apart. Detectors with two bands or multi-bands can be easily fabricated by vertical stacking of different quantum well structures. Gunapala *et al*. reported a four-band FPAs including four 640×128 pixel areas which are sensitive in 4-6, 8.5-10, 10-12 and 13-15 μm range for imaging applications [40]. Four bands were separated by etching process and unwanted junction was shorted by metal contact.

Table 1.2 The properties of HgCdTe, QWIPs and InAs/$Ga_xIn_{1-x}Sb$ SLS at 77 K [36]

Parameters	HgCdTe	QWIPs(n-type)	InAs/$Ga_xIn_{1-x}Sb$ SLS
IR absorption	Normal incidence	Diffraction grating needed for absorption	Normal incidence
Quantum efficiency	≥ 70 %	≤10 %	30 %-40 %
Spectral range	Wide-band	Narrow-band	Wide-band
Thermal generation lifetime	≈1 μs	≈10 ps	≈0.1 μs

Besides MCT and QWIP detectors, the InAs/$Ga_xIn_{1-x}Sb$ strained layer superlattice (SLS) material system has been considered as the most promising IR detectors. In the SLS structure the absorption is stronger than QWIP thus provide higher responsivity without any grating required in QWIPs. The band gap can be modified by adjusting InAs monolayer thickness. Unlike bulk materials such as MCT, the InAs/$Ga_xIn_{1-x}Sb$ SLS shows larger effective mass, suggesting lower tunnelling current. The properties of these three technologies at 77 K are summarised and compared in Table 1.2. Narrow band gap materials challenges to have low intentional doping level to reduce tunnelling current, normally below 1×10^{15} cm^{-3} and carrier lifetime needs to be increased to enhance diffusion length and improve device performance. However, the lifetime of SLS is limited by Shockley-Read-Hall recombination process. The Shockley-Read-Hall recombination is the carrier recombination process occurred in the localized energy state introduced by an impurity in the lattice. The background residual carrier density for both p- and n-type is still around 5×10^{15} cm^{-3} at present [41].In general, InAs/$Ga_xIn_{1-x}Sb$ SL

photodiodes employ normal *p-i-n* structure. Most of the MWIR and LWIR detectors are based on InAs/GaSb superlattices. The most challenging fabricating aspect is achieving a small surface leakage current. To eliminate leakage current, passivation techniques and shallow mesa etch with band-graded junction [42] have been explored.

The 256×256 MWIR SLs detectors with 40 μm pixel size and a cut-off wavelength at 5.3 μm have been tested and presented a low NETD of 12 mK [43]. The first LWIR InAs-GaSb SLs FPAs with a cut-off at 10 μm was demonstrated by Delaunay *et al*.[44], presenting a NETD and integration time of 33 mK at 81 K operating temperature and 0.23 ms which is comparable to MCT. They also reported a *n-i-p-p-i-n* two-colour type-II InAs/GaSb photodiode with a quantum efficiency of 40 % and 39% at 5.3 μm and 8.5 μm at 77K [45]. The MWIR T2SL dual colour FPA was first reported with selective detection in the 3-4.1 μm and 4.1-5 μm wavelength range and 40 μm pitch size [46]. It achieves a good thermal resolution with NETD < 30 mK and 17 mK for longer and lower wavelength range and integration time of 2.8 ms for both selected wavelength range.

All these three technologies focus on the LWIR and MWIR detectors which need to be cooled for high temperature resolution. Currently, uncooled two colour detectors mostly operate at NIR and SWIR. Tandem Si-Si [47] and Si-InGaAs [48] two colour detectors are commercially available. These detectors use two single photodiodes, with the short wavelength detector mechanically stacked on top of the longer wavelength detector. Such a method is however impractical for imaging array applications.

1.5.2 Photon-counting detector

In order to achieve lower temperature sensing, either longer wavelength detectors or higher sensitivity detectors have been employed in radiation thermometers. When compared to conventional photo detectors, detectors with extremely high sensitivity such as avalanche photodiodes (APDs) or single photon detectors can provide higher signal to noise ratio.

A photomultiplier tube (PMT) is one of most sensitive detectors with extremely high gain of over a million and is capable of detecting down to individual photons [49]. It has also

been demonstrated in radiation thermometry and developed as a photon counting pyrometer [50,51]. Based on a PMT photon-counting pyrometer, Coates and Andrew developed a precise determination of copper freezing point [52] and reviewed the thermodynamic temperature above zinc point [53].

Similarly, a single photon avalanche photodiode (SPAD) works at Geiger mode which provides high gain (> million) and presents a high potential for photon-counting thermometer. A full description of SPAD operation is given in section 2.3.3. Currently, Si SPADs, are most widely used for visible and near-IR wavelengths due to their mature fabrication technology [54]. Si SPAD arrays have also been developed for 3D imaging and low-light-level 2D imaging applications. Tisa *et al*. [55] presented a monolithic 32 Si SPAD pixels for imaging applications with high frame rates and high sensitivity. However, the band gap energy of 1.1 eV makes it unsuitable for longer wavelength detection beyond 1.0 μm. For applications ranging from 0.95 μm to 1.65 μm, especially for optical telecommunications working at 1.3 μm and 1.55 μm, InGaAs material system have been widely used. Avalanche photodiodes with a separate $In_{0.53}Ga_{0.47}As$ absorption layer and InP multiplication region are widely used due to the superior speed, responsivity and low noise characteristics. Recently, the adoption of InGaAs/InP SPADs have also become more attractive in research groups for single-photon detecting applications. Earlier studies developed an InGaAs/InP SPAD with a photon detection efficiency of 20 % and dark count rate of ~ 1 kHz at 215 K [56]. Nowadays, 128×32 InGaAsP/InP SPAD arrays with pitch size of 50 μm for 3D imaging at 1064 nm have been designed and made commercially available from Princeton Lightwave Inc. [57]. They also developed the first generation 32×32 InGaAs/InP SPAD arrays for imaging at 1.55 μm [58]. More recently InGaAs/InAlAs SPAD operating at room temperature has been reported with a single photon detection efficiency of 10% [59].

1.5.3 Uncooled IR detectors

In 1970s, uncooled IR detectors were developed by US researchers for thermal imaging in military applications. Barium strontium titanate (BST) IR detector and micromachining bolometer technology have been demonstrated in 1979 [60]. However, the mechanical chopper and thermoelectric cooling makes the BST not attractive for

further development compared with Vanadium oxide (VO_x) technology. In the mid 1990's, amorphous silicon technology was developed due to the advantage of fabrication technique in silicon foundry. At present, VO_x microbolometer arrays are used technology for uncooled detectors in thermal imaging systems [60]. For thermal detectors, the key trade-off is the sensitivity and response time. They are competing effects due to the inverse relationship with thermal conductance. The advanced technology will improve the sensitivity but sacrifice the response time.

As stated earlier, photon detectors provide a higher sensitivity and faster response time than conventional thermal detectors. Most uncooled photodetectors are restricted for short wavelength operation which is dominated by III-V compounds, such as InGaAs. For middle and long wavelength range applications, InSb and MCT are still dominant technologies. However, due to limitations of the material issue and low temperature operation, alternative materials have been investigated.

Unlike InSb and HgCdTe, InAs photodiodes with a larger band gap energy of 0.35 eV, corresponding to a cut-off at 3.6 μm, have the potential to work as an uncooled MWIR detector. In early 1960s, Lucovsky [61] reported a cadmium diffused InAs p-n junction with a dark current of 10 mA at reverse bias of 10 V. Lin *et al*. [62] studied InAs *p-i-n* photodiodes with i-layer thickness ranging from 0 to 0.72 μm. The dark current was reported to be suppressed by increasing i-layer thickness and can be reduced by ~6 orders of magnitude when cooling to 40 K. However, due to high surface leakage, the photodiodes were normally operate below 0.5 V. Both Hamamatsu and Teledyne Judson Technologies can provide uncooled commercial InAs photodiodes for photovoltaic operation. In the late 2000s, InAs APDs with low excess noise and high gain was reported by Marshall *et al.* [63]. In their later optimisation, high speed InAs APDs with a gain-bandwidth product of 430 GHz at room temperature was reported [35].

The InAsSb ternary alloy, with flexible detection wavelength range up to 12 μm, is an alternative technology to MCT. Compared with MCT, it is more stable and shows better physical properties such as low dielectric constant and diffusion coefficient at room temperature [35]. The InAsSb detector technology has been developed as useful photodiodes for thermal imaging system and optical fibre communication. Considerable

progress in near room-temperature operation has been achieved in InAsSb alloy based detectors. From the study of Rogalski *et al*., the theoretical performance of InAsSb photodiodes at high temperature is competitive with MCT. The first uncooled long IR InAsSb heterojunction photodiode was reported with a peak detectivity of 1.5×10^{8} $cmHz^{1/2}/W$ at 10.6 μm by Kim *et al*. [64]. Recently, Gao *et al*. [65] reported an $InAs_{0.052}Sb_{0.948}$ photoconductor with a peak detectivity of 5.4×10^{9} $cmHz^{1/2}/W$.

1.6 Gaps/Motivation

For high temperature sensing applications such as the steel industry, shorter wavelength thermometers show a higher temperature resolution than single thermometers with longer operation wavelength. To correct the emissivity problem due to attenuation along the line of sight, ratio thermometers is more attractive in such applications. Despite the lack of short wavelength ratio thermometers, ratio thermometers with shorter operation wavelength are desirable for high temperature sensing. The $In_{1-x-y}Ga_xAl_yAs$ quaternary alloy, which is a direct band gap material and lattice match to InP, can be easily combined with InGaAs to form two-colour imaging arrays grown on high quality InP substrates. The InGaAlAs-InGaAs material system has a huge potential as a ratio thermometer/imager and its evaluation as a ratio thermometer will be presented in this thesis.

From previous work, the InAs photodiode provide high performance at room temperature up to 3.6 μm. InAs has been reported for many mid-IR applications. It has vast potential for low temperature thermometers or narrow band thermometers working at 3.43 μm for detecting materials with C-H bonds. In this thesis, the performance of InAs photodiode is evaluated.

As target temperature decreases, the total emitted energy reduces and peak energy wavelength shift to longer wavelength. In order to detect lower temperatures, thermometers with longer operation wavelength are chosen. Single photon detectors which can detect very low light level also present benefits in such low temperature applications. From previous study, Photomultiplier tubes with extremely high gain and low noise have been studied for thermometry measurement using photon counting mode.

However, single photon avalanche photodiodes have not been systematic studied for this operation mode in radiation thermometry. A commercial Si SPAD was evaluated as photon counting thermometer in this work.

To achieve high performance SPADs, a suitable model is needed to design and predict the avalanche process. In most APDs or SPADs, the structures have non-uniform electric field profiles. By modelling the carrier transport process, a simple Monte Carlo model with capability of dealing with non-uniform electric field will be introduced for design of Si APDs/SPADs.

More detailed motivations will be provided as introduction in each chapter. The work described in this thesis can be divided into three main sections: a study of the InGaAlAs/InGaAs two-colour detector in a ratio thermometer for high temperature sensing applications, an evaluation of uncooled InAs photodiode as a 3.43 μm thermometer, investigation of Si SPAD for radiation thermometry and modelling of ionisation process in Si APDs and SPADs. Consequently the thesis is organised as follows:

Chapter 2 provides the background theory of radiation thermometry in terms of theoretical calculation of output signal from a practical single-band thermometer or ratio thermometer. The principles of photodiodes or avalanche photodiodes are outlined in this chapter, followed by a simple Monte Carlo model description.

Chapter 3 describes the experimental techniques for characterisation of photodiodes/APDs in this work. In each technique, the electrically or optically characterisation setup is illustrated and the working principles and optimised operation steps are described.

Chapter 4 demonstrates an InGaAlAs/ InGaAs two-colour detector for use as a ratio thermometer. The electrical and optical performance of the two-colour detector was first characterised, followed by the thermometry test as a ratio thermometer.

Chapter 5 describes the uncooled InAs MWIR photodiode as a viable option for low temperature radiation thermometers working at 3.43 μm for plastic industry. The device noise due to dark current and signal from high response are all analysed for applications involved with low temperature sensing. Mid-IR filter is also used to evaluate the InAs performance in 3.43 μm thermometers.

Chapter 6 investigates a Si SPAD as the detector in a radiation thermometer. A commercial Si SPAD with low dark count rate was evaluated for radiation thermometry measurement.

Chapter 7 details the development of a Simple Monte Carlo model to predict the avalanche process in Si APDs and SPADs. The ionisation coefficient and drift velocity of Si were simulated using this model. The avalanche gain and excess noise in APD can be accurately predicted. The qualitative behaviour of Si SPADs was also modelled.

Chapter 8 draws the conclusion of all the work performed in this thesis. Future work are discussed and potential areas of interest are also proposed.

References

[1] "Electromagnetic Spectrum," PION, [Online]. Available: http://www.pion.cz/en/article/electromagnetic- spectrum. [Accessed 04 Sep 2014].

[2] S. D. Gunapala and S. V. Bandara, "Quantum well infrared photodetector (QWIP) focal plane arrays," in *Intersubband Transitions in Quantum Wells: Physics and Device Applications I*, Academic Press, 2000, pp. 197-291.

[3] T. J. Quinn, "Radiation thermometry," in *Temperature*, London, UK, Academic Press, 1990, pp. 332-431.

[4] L. Michalski, K. Eckersdorf, J. Kucharski and J. McGhee, Temperature Measurement, New York: John Wiley & Sons, Inc., 2001.

[5] H. L. Chatelier, in *On the measurement of high temperatures*, Comptes Rendus Academie des Sciences, 1892, pp. 214-216.

[6] W. Forsythe, "The disappearing filament type of optical pyrometer," *Transactions of the Faraday Society*, vol. 15, pp. 21-50, 1920.

[7] W. P. Wood and J. M. Cork, Pyrometry, New York: McGraw-Hill, 1941.

[8] D. P. DeWitt and G. D. Nutter, "Spectral-band radiation thermometry," in *Theory and Practice of Radiation Thermometry*, New York, John Wiley & Sons, Inc., 1988, pp. 341-458.

[9] A. C. Parr, R. U. Datla and a. J. L. Gardner, "Optical Radiometry," in *Experimental Methods in the Physical Sciences*, San Diego,CA, Elsevier, 2005.

[10] E. C. Magison, "Radiation thermometers-theory and construction," in *Temperature measurement in industry*, North California, Instrument Society of America, 1990, pp. 97-122.

[11] Z. M. Zhang, B. K. Tsai and G. Machin, "Industrial applications of radiation thermometry," in *Radiometric temperature measurements. II. Applications*, USA, Elsevier Inc., 2010, pp. 2-54.

[12] A. Rogalski, Infrared detectors, Boca Raton, FL: CRC Press, 2011.

[13] J. Hollandt, J. Hartmann, B. Gutschwager and O. StruX, "Radiation Thermometry- Non-Contact Temperature Measurements," *Automatisierungstechnische Praxis (atp)*, vol. 48, p. 70281, 2006.

[14] G. P. Eppeldauer, "Electronic characteristics of Ge and InGaAs radiometers," in *Proc. of SPIE 3061*, Orlando, FL, USA, Aug. 1997.

[15] J. B. D. Soole and H. Schumacher, "InGaAs metal-semiconductor-metal photodetectors for long wavelength optical communications," *IEEE Journal of Quantum Electronics*, vol. 27, no. 3, pp. 737-752, Mar. 1991.

[16] F. Sakuma and T. K. L. Ma, "Development of a New InGaAs Radiation Thermometer at NMIJ," *Int J Thermophys*, vol. 29, no. 1, pp. 312-321, 2008.

[17] H. W. Yoon, C. E. Gibson, V. Khromchenko and G. P. Eppeldauer, "SSE- and Noise-Optimized InGaAs Radiation Thermometer," *Int J Thermophys*, vol. 28, no. 6, pp. 2076-2086, 2007.

[18] F. Sakuma and L. Ma, "Development of InGaAs Radiation Thermometers," in *SICE Annual Conference*, Tokyo, 20-22 Aug. 2008.

[19] "Product overview for non-contact temperature measurement," Optris GmbH, [Online]. Available: http://www.optris.co.uk/temperature-sensors-and-thermal-imagers?file=tl_files/pdf/Downloads/Zubehoer/Optris%20Product%20brochure.pdf.&file=tl_files/pdf/Downloads/Zubehoer/Optris%20Product%20brochure.pdf.. [Accessed Sep. 2014].

[20] H. W. Yoon and G. P. Eppeldauer, "Measurement of thermal radiation using regular glass optics and short-wave infrared detectors," *Optical Express*, vol. 16, no. 2, pp. 937-940, Jan. 2008.

[21] R. J. Cashman, "Film-type infrared photoconductors," *Proc. IRE*, vol. 47, no. 9, pp. 1471-1475, 1959.

[22] A. Rogalski, K. Adamiec and J. Rutkowski, "Lead salt photodiodes," in *Narrow-Gap semiconductor photodiodes*, Washington, USA, SPIE, 2000, pp. 361-397.

[23] "Standard radiation thermometer," Chino Corporation, [Online]. Available: http://www.chino.co.jp/english/download/pdf/IR-RST_PSE-600.pdf. [Accessed 04 Sep 2014].

[24] E. Burstein, S. Perkowitz and M. H. Brodsky, "The dielectric properties of the cubic IV-VI compound semiconductors," *J. Phys. Colloques*, vol. 29, no. C4, pp. 78-83, Nov. 1968.

[25] R. Dalven, "Electron-Optical-Polaron Coupling Constant in PbS, PbSe and PbTe," *Phy. Rev. B*, vol. 3, no. 6, pp. 1953-1954, Mar. 1971.

[26] A. Rogalski, "History of infrared detectors," *Opto-Electron. Rev.*, vol. 20, no. 3, pp. 279-308, 2012.

[27] A. Rogalski, "Infrared detectors: an overview," *Infrared Physics & Technology*, vol. 43, pp. 187-210, 2002.

[28] A. Rogalski, K. Adamiec and J. Rutkowski, Narrow-Gap Semiconductor Photodiodes, 1st ed., Bellingham, WA: SPIE Press, 2000.

[29] H. C. McEvoy, D. H. Lowe and M. Owen, "The NPL InSb-based radiation thermometer for the medium temperature range (<962 °C)," *Int. J. Thermophys*, vol. 28, no. 6, pp. 2067-2075, Oct. 2007.

[30] J. Ishii and A. Ono, "Low-Temperature infrared radiation thermometry at NMIJ," *AIP Conference Proceedings*, vol. 684, no. 1, pp. 657-662, Sep. 2003.

[31] W. J. Parrish, J. D. Blackwell, G. T. Kincaid and R. C. Paulson, "Low-cost high performance InSb 256 ×256 infrared camera," *Proc. of SPIE*, vol. 1540, pp. 274-284, Dec. 1991.

[32] A. Rogalski, "HgCdTe infrared detector material: history, status and outlook," *Rep. Prog. Phys.*, vol. 68, no. 10, pp. 2267-2336, 2005.

[33] J. Fraden, "Infrared Electronic Thermometer and Method for Measuring Temperature". U.S. Patent 4797840, 1989.

[34] H. Jerominek, F. Picard and D. Vincent, "Vanadium oxide films for optical switching and detection," *Optical Engineering*, vol. 32, no. 9, pp. 2092-2099, Sep. 1993.

[35] A. Rogalski, "Infrared detectors: status and trends," *Progress in Quantum Electronics*, vol. 27, no. 2-3, pp. 59-210, 2003.

[36] A. Rogalski, "Infrared detectors for the future," *ACTA Physica Polonica A*, vol. 116, no. 3, pp. 389-405, 2009.

[37] D. F. King, W. A. Radford, E. A. Patten, R. W. Graham, T. F. McEwan, J. G. Vodicka, R. E. Bornfreund, P. M. Goetz, G. M. Venzor, S. M. Johnson, J. E. Jensen, B. Z. Nosho and J. A. Roth, "3rd-Gnereration 1280×720 FPA development status at Raytheon Vision Systems," Proc. of SPIE, vol. 6206, pp. 62060W, 2006.

[38] R. Bornfreund, J. Rosbeck, Y. Thai, E. Smith, D. Lofgreen, M. Vilela, A. Buell, M. Newton, K. Kosai, S. Johnson, T. DeLyon, J. Jensen and M. Tidrow, "High-Performance LWIR MBE-Grown HgCdTe/Si Focal Plane Arrays," *J. Electron. Mater.*, vol. 36, no. 8, pp. 1085-1091, 2007.

[39] S. D. Gunapala, S. V. Bandara, J. K. Liu, C. J. Hill, S. B. Rafol, J. M. Mumolo, J. T. Trinh, M. Z. Tidrow and P. D. LeVan, "1024 x 1024 Pixel mid-wavelength and long-wavelength infrared QWIP focal plane arrays for imaging applications," *Semicond. Sci. Technol.*, vol. 20, no. 5, pp. 473-480, Mar. 2005.

[40] S. D. Gunapala, S. V. Bandara, J. K. Liu, S. B. Rafol and J. M. Mumolo, "640x512 Pixel Long-wavelength Infrared Narrowband, Multiband, and Broadband QWIP Focal Plane Arrays," *IEEE Trans. Electron Devices*, vol. 50, no. 12, pp. 2353-2360, Dec. 2003.

[41] L. Bürkle and F. Fuchs, "InAs/(GaIn)Sb superlattices: a promising material system for infrared detection," in *Handbook of Infrared Detection and Technologies*, Oxford, Elsevier, 2002, pp. 159-189.

[42] E. Aifer, J. Tischler, J.H.Warner, I. Vurgaftman, W. Bewley, J. Meyer, C. Canedy and E. Jackson, "W-structured type-II superlattice long-wave infrared photodiodes with high quantum efficiency," *Appl. Phys. Lett.* , vol. 89, no. 5, p. 053510, 2006.

[43] W. Cabanski, K. Eberhardt, W. Rode, J. Wendler, J. Ziegler, J. Fleißner, F. Fuchs, R. Rehm, J. Schmitz, H. Schneider and M. Walther, "Third-generation focal plane array IR detection modules and applications," *Proc. of SPIE*, vol. 5406, pp. 184-192, 2005.

[44] P. Y. Delaunay, B. M. Nguyen, D. Hoffman and M. Razeghi, "High-Performance Focal Plane Array Based on InAs–GaSb Superlattices With a 10-Cutoff Wavelength," *IEEE J. Quant. Electron.*, vol. 44, no. 5, pp. 462-467, May 2008.

[45] P. Y. Delaunay, B. M. Nguyen, D. Hoffman, A. Hood, E. K.-W. Huang, M. Razeghi and M. Z. Tidrow, "High quantum efficiency two color type-II InAs/GaSb n-i-p-p-i-n photodiodes," *Applied Physics Letters, vol. 92, 111112, 2008*, vol. 92, no. 11, p. 111112, 2008.

[46] M. Munzberg, R. Breiter, W. Cabanski, H. Lutz, J. Wendler, J. Ziegler, R. Rehm and M. Walther, "Multipectral IR detection modules and applications," *Proc. of SPIE,* vol. 6206, p. 620627, 2006.

[47] "Dual sandwich detector series," OSI Optoelectronics, [Online]. Available: http://www.osioptoelectronics.com/Libraries/Product-Data-Sheets/Two-Color-Sandwich-Detectors.sflb.ashx. [Accessed Sep 2014].

[48] "Two-color photodetector K1713-05/-08/-09," Hamamatsu Photonics K. K., Aug. 2014. [Online]. Available: http://www.hamamatsu.com/resources/pdf/ssd/k1713-05_etc_kird1040e04.pdf.

[49] S. Kinishita and T. Kushida, "High-performance, time-correlated single-photon counting apparatus using a side-on type photomultiplier," *Rev. Sci. Instrum.*, vol. 53, no. 4, pp. 469-475, Apr. 1982.

[50] B. W. Mangum, G. T. Furukawa, K. G. Kreider, C. W. Meyer, D. C. Ripple, G. F. Strouse, W. L. Tew, M. R. Moldover, B. C. Johnson, H. W. Yoon, C. E. Gibson and R. D. Saunders, "The Kelvin and temperature measurements," *J. Res. Natl. Inst. Stand. Technol.*, vol. 106, no. 1, p. 105–149, Feb. 2001.

[51] P. B. Coates, J. W. Andrews and M. V. Chattle, "Measurement of the difference between IPTS-68 and thermodynamic temperature in the range 457 °C to 630 °C," *Metrologia*, vol. 21, no. 1, pp. 31-35, 1985.

[52] P. B. Coates and J. W. Andrews, "A precise determination of the freezing point of copper," *J. Phys. F: Metal Phys.*, vol. 8, no. 2, pp. 277-285, 1978.

[53] P. B. Coates and J. W. Andrews, "Measurement of thermodynamic temperature with the NPL photon-counting pyrometer," in *Temperature: Its measurement and control in science and industry, vol. 5, part 1*, 1982, pp. 109-114.

[54] S. Cova, M. Ghioni, M. A. Itzler, J. C. Bienfang and A. Restelli, "Semiconductor-Based detectors," in *Single-photon generation and detection: Physics and Applications, edited by A. Migdall, S. Polyakov, J. Fan and J. Bienfang*, USA, Elsevier Inc., 2013, pp. 83-146.

[55] S. Tisa, F. Guerrieri and F. Zappa, "Monolithic array of 32 SPAD pixels for single-photon imaging at high frame rates," *NDIP08*, vol. 610, no. 1, pp. 24-27, Oct. 2009.

[56] M. A. Itlzer, X. Jiang, M. Entwistle, K. Slomkowshi, A. Tosi, F. Acerbi, F. Zappa and S. Cova, "Advances in InGaAsP-based avalanche diode single photon detectors," *J. Mod. Opt.*, vol. 58, no. 3-4, pp. 173-200, Feb. 2011.

[57] "128×32 Geiger-mode avalanche photodiode (GmAPD) camera," Princeton Lightwave, 2013. [Online]. Available: http://www.princetonlightwave.com/images/pli_content/PLI%20128x32%20GmAPD%20Camera%20-%20ProdSum%20Rev%201.2.pdf.

[58] "32×32 Geiger-mode avalanche photodiode (GmAPD) camera," Princeton Lightwave, 2012. [Online]. Available: http://www.princetonlightwave.com/images/pli_content/PLI%2032x32%20GmAPD%20Camera%20-%20ProdSum%20Rev%202.0.1.pdf.

[59] X. Meng, C. H. Tan, S. Dimler, J. P. R. David and J. S. Ng, "1550 nm InGaAs/InAlAs single photon avalanche diode at room temperature," *Opt. Express* , vol.22, no. 19, pp.22608-22615, 2014.

[60] "Uncooled detectors for thermal imaging cameras," FLIR, [Online]. Available: http://www.flir.com/uploadedFiles/Eurasia/Cores_and_Components/Technical_Notes/uncooled%20detectors%20BST.pdf. [Accessed Sep 2014].

[61] G. Lucovsky, "Electrical characteristics of diffused InAs p-n junctions," *British J. Appl. Phys.*, vol. 12, no. 6, p. 311, 1961.

[62] R. M. Lin, S. F. Tang, S. C. Lee and C. H. Kuan, "Improvement of current leakage in the InAs photodetector by molecular beam epitaxy," *J. Crystal Growth*, Vols. 227-228, pp. 167-171, Jul. 2001.

[63] A. R. J. Marshall, C. H. Tan, M. J. Steer and J. P. R. David, "Extremely Low Excess Noise in InAs Electron Avalanche Photodiodes," *IEEE Photon. Technol. Lett.*, vol. 21, no. 13, pp. 866-868, 2009.

[64] J. D. Kim, S. Kim, D. Wu, J. Wojkowski, J. Xu, J. Piotrowski, E. Bigan and M. Razeghi, "8–13 μm InAsSb heterojunction photodiode operating at near room temperature," *Applied Physics Letters*, vol. 67, no. 18, pp. 2645-2647, 1995.

[65] Y. Gao, X. Gong, G. Wu, Y. Feng, T. Makino, H. Kan, T. Koyama and Y. Hayakawa, "InAsSb thick epilayers applied to long wavelength photoconductors," *International Journal of Minerals, Metallurgy and Materials*, vol. 20, no. 4, pp. 393-396, Apr. 2013.

Chapter 2 Background theory

2.1 Introduction

This chapter describes the background theory of radiation thermometry. It also introduces the operation principles of photodetectors, APDs and SPADs and provides details of the Monte Carlo technique used for modelling the avalanche process in APDs and SPADs.

2.2 Basics of radiation thermometry

2.2.1 Blackbody and non-blackbody radiation

When an electromagnetic wave incident on an object, a portion of the wave can be absorbed, reflected and the remaining portion transmitted. The sum of three components should always equal to the magnitude of the incident wave arrived on its surface. Thus, the relationship of object absorption, reflection and transmission factor can be described as

Absorption + reflection + transmission = 1

If most of wave is transmitted, the object can be considered as transparent. If the material reflectivity is too high, then it is a mirror-like object. Therefore objects with low reflection and transmission can absorb most of the incident wave and can be regarded as opaque. The roughness of surface may reduce the reflection and thus increase its absorptivity.

Under thermal equilibrium, Kirchhoff law [1,2] states that the radiated energy from an object must equal its absorbed energy. A blackbody is an ideal object which can absorb all the incident light on its surface, independent of incident direction and wavelength. No surface can absorb light more efficiently than a blackbody source. At a given temperature, the emitted energy from a blackbody follows Planck's equation, reproduced below,

$$L_{b,\lambda}(\lambda, T_{BB}) = \frac{2\pi c^2 h}{\lambda^5 \left(e^{\left(\frac{hc}{\lambda k_B T_{BB}}\right)} - 1 \right)} \quad W/m^3 \tag{2.1}$$

For real materials, the emitted radiation is less than that of a blackbody. The emissivity, ε is the ratio of the emissive power of the object to the emissive power of a blackbody at the same temperature, where $\varepsilon = 1$ for a blackbody and $\varepsilon < 1$ for real materials. A Greybody is a material whose emissivity is constant independent of wavelength. In a practical temperature measurement, the greybody concept is employed to characterise the radiated power

$$L_\lambda(\lambda, T) = \varepsilon L_{b,\lambda}(\lambda, T_{BB}) \tag{2.2}$$

It is clear that the power reduction is equal across the whole spectrum range for perfect greybody. However, a non-greybody object also needs to be considered in many applications. In such cases, the radiation is strongly dependent on wavelength. Figure 2.1 compares the spectral radiance from the blackbody, perfect greybody with $\varepsilon = 0.7$ and non-greybody ($\varepsilon = 0.4$, $\varepsilon = 0.3$) at temperature of 500 ºC.

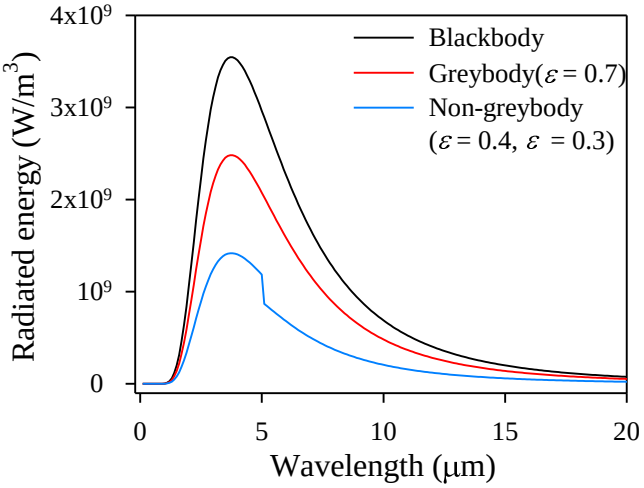

Figure 2.1 Spectral radiance from the blackbody, greybody and non-greybody at a temperature of 500 ºC

2.2.2 Broadband radiation thermometry

The fundamental theory of radiation thermometry has been well established. For broadband radiation thermometry, the total radiated energy from a blackbody at temperature T per unit area is stated by Stefan-Boltzmann law. It can be expressed as

$$L_B = \sigma T^4 \quad \text{W/m}^2 \tag{2.3}$$

where σ = 5.6704×10^{-8} Js^{-1}m^{-2}K^{-4} is Stefan-Boltzmann constant. For a real surface, the emissivity is lower than 1 and need to be accounted for in the equation (2.2). Thus the total emitted energy from an object at temperature T can be modified to

$$L_o = \varepsilon\sigma T^4 \quad \text{W/m}^2 \tag{2.4}$$

Assuming the temperature T_o is total radiance temperature when blackbody emit same amount of power as object. It can be easily described as

$$T_o = \varepsilon^{1/4} T \tag{2.5}$$

which is always equal to, or lower than, the true object surface temperature. By correcting the emissivity in deriving object true temperature, a variation in emissivity will corresponding to a temperature error by

$$\frac{dT}{T} = -\frac{1}{4}\frac{d\varepsilon}{\varepsilon} \tag{2.6}$$

A small uncertainty in emissivity for broadband thermometers results in large errors in temperature measurement [3]. For instance, when measuring an object temperature of 500 K, a 4% emissivity will result in a temperature error of 5 K. Broadband detectors such as thermopiles or pyroelectric detectors are mostly employed in this type of thermometers for ambient temperature measurement due to lower impact of emissivity uncertainty.

2.2.3 Spectral radiation thermometry

By using a photodetector with a narrow spectrum or a selected bandpass filter in radiation thermometry measurement, the radiation thermometer will produce an output electrical signal in response to incident radiance, which is given by

$$S_\lambda = C_I \int_{\lambda-\Delta\lambda/2}^{\lambda+\Delta\lambda/2} \mathcal{R}(\lambda) L_\lambda(\lambda, T) d\lambda \tag{2.7}$$

where $R(\lambda)$ is the responsivity at wavelength of λ, C_I is instrument factor, it is given by[4]

$$C_I = sin^2\left(\frac{\theta}{2}\right) A T_f(\lambda)(1-r) F_c cos(\varphi) \tag{2.8}$$

where A is detector area, T_f is the transmission factor of the system, r is the reflectivity of detector, F_c is the optical chopper factor (F_c = 1 without chopper), φ is the incident angle, θ = 2 tan^{-1} (ρ/D) is the optical field of view under assumption of no focusing lens.

D is the distance between detector and blackbody source and ρ is the radius of blackbody source aperture as shown in Figure 2.2.

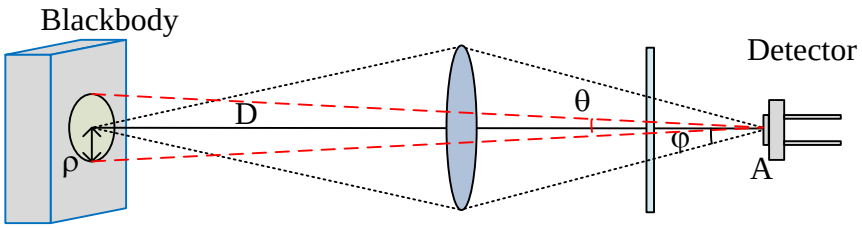

Figure 2.2 Schematic diagram of thermometry measurement setup

When a narrow bandpass filter ($\Delta\lambda \rightarrow 0$) is employed in the system, the output signal can be simplified to

$$S_\lambda = C_I \mathcal{R}(\lambda) L_\lambda(\lambda, T) \tag{2.9}$$

By substituting equation (2.1) into (2.7) and differentiating it with respect to *T*,

$$\frac{\mathrm{d}L_\lambda}{L_\lambda} = \frac{c_2}{\lambda T}\left[\frac{e^{c_2/\lambda T}}{e^{c_2/\lambda T} - 1}\right]\frac{dT}{T} \tag{2.10}$$

where c_2 = 1.4388 cm·K is second radiation constant. This gives the temperature uncertainty as a function of radiance change, which is illustrated in Figure 2.3.

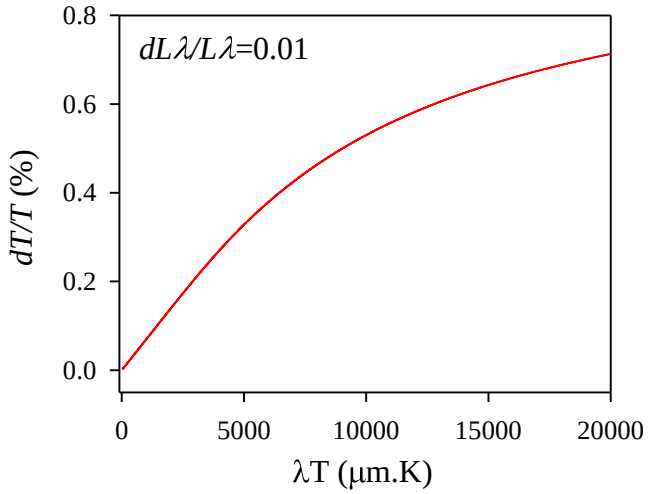

Figure 2.3 Uncertainty in spectral radiance due to change in temperature of 1%

According to Wien's approximation that $c_2/\lambda T >> 1$, this can be simplified to

$$\frac{\mathrm{d}L_\lambda}{L_\lambda} = \frac{c_2}{\lambda T}\frac{dT}{T} \tag{2.11}$$

The temperature uncertainty of single wavelength thermometer can be determined from this equation. The radiance temperature T_r is the temperature at which blackbody give the same radiance at the temperature T, thus the relationship between these two temperatures can be deriven from equation (2.1) based on Wien's approximation which is given by

$$\frac{1}{T} = \frac{1}{T_r} + \frac{\lambda}{c_2} \ln \varepsilon \tag{2.12}$$

Then the temperature error given by emissivity uncertainty can be calculated by differentiating above equation, giving by

$$\frac{\Delta T}{T} = -\frac{\lambda T}{c_2} \frac{\Delta \varepsilon}{\varepsilon} \tag{2.13}$$

It is clear that for a given uncertainty in emissivity, the temperature error increases with operational wavelength. Thus, for more accurate measurement, shorter wavelength thermometers need to be chosen.

For two-band thermometers, the ratio of the output of both detectors is described as

$$Q = \frac{L_{\lambda_2}}{L_{\lambda_1}} = \frac{\varepsilon_2 {\lambda_2}^{-5}}{\varepsilon_1 {\lambda_1}^{-5}} \exp[\frac{c_2}{T}\left(\frac{1}{\lambda_1} - \frac{1}{\lambda_2}\right)] \tag{2.14}$$

In order to look for the ratio thermometer performance, we differentiate the equation (2.14) with respect to T,

$$\frac{dQ}{dT} = -\frac{c_2}{T^2}\left(\frac{1}{\lambda_1} - \frac{1}{\lambda_2}\right) \frac{\varepsilon_2 {\lambda_2}^{-5}}{\varepsilon_1 {\lambda_1}^{-5}} \exp\left[\frac{c_2}{T}\left(\frac{1}{\lambda_1} - \frac{1}{\lambda_2}\right)\right] = -\frac{c_2}{T^2}\left(\frac{1}{\lambda_1} - \frac{1}{\lambda_2}\right) Q \tag{2.15}$$

This can be rewritten as [5]

$$\Delta T = -[\frac{c_2}{T^2}\left(\frac{1}{\lambda_1} - \frac{1}{\lambda_2}\right)]^{-1} \frac{\Delta Q}{\mathrm{Q}} \tag{2.16}$$

Therefore, the temperature error can be calculated based on the output signal and the effective operation wavelength. The effective operation wavelength in ratio thermometer is given by

$$\lambda_e = \frac{\lambda_1 \lambda_2}{\lambda_1 - \lambda_2} \tag{2.17}$$

This method is useful if the surface emissivity is constant at both wavelengths. The ratio thermometer has always been implemented and provides more benefits in specific situations, especially for target smaller than the thermometer field of view and attenuated sighting view. However, for a non-greybody measurement, the wavelength dependent

emissivity needs to be used. The ratio thermometer need to account for the non-greyness factor which is the ratio of two wavelength emissivities. Considering the same percentage in emissivity uncertainty and non-greyness, ratio thermometer operates at longer effective wavelength than single wavelength thermometer, resulting in higher temperature uncertainty [2]. Therefore, the ratio thermometer needs a higher requirement in non-greyness control and shorter wavelengths operation are preferred for more accurate temperature measurement.

2.3 Detectors in radiation thermometers

As described in the first chapter, photodetectors and thermal detectors can be used as radiation thermometers. As photodetectors can provide higher sensitivity and perform more accurate measurement at specific temperature range, this work explores new photodetectors for radiation thermometry. The basic concepts of photodiodes, APDs and SPAD are discussed below.

2.3.1 Photodiodes

A photodiode is usually designed to operate at small reverse bias with a depletion region that converts optical signal to electrical current [6]. The quantum efficiency, which is defined as the number of photogenerated carriers per incident photon, need to be maximised to improve sensitivity of the photodiode. It can be described as

$$\eta = \frac{I_{ph}}{q}\left(\frac{h\nu}{P_{opt}}\right) \tag{2.18}$$

where I_{ph} is the photocurrent, q is the electron charge, ν is the frequency of light and P_{opt} is the incident light power. Carriers generated in the depletion width and region within the diffusion length can all contribute to the photocurrent under electric field. The total photocurrent density is given by

$$J_{tt} = J_{dr} + J_{diff} \tag{2.19}$$

where J_{dr} is the drift current due to photogenerated carriers in the depletion width and J_{diff} is the diffusion current due to generated carriers outside of depletion width which diffused into electric field region. To increase the quantum efficiency of the diode, large depletion region is needed for more light absorption while thin depletion layer is required for high speed operation. Thus, there is a trade-off between these two parameters. In this

section, we briefly consider the general characteristics of a photodiode for temperature measurement. For a good photodiode, it should achieve a high quantum efficiency and high speed with minimum detector noise.

The responsivity, $\mathcal{R}$ is a key parameter for a photodetector, which is a ratio of the generated photocurrent to incident optical power, expressed in A/W. It can be written as

$$\mathcal{R} = \frac{I_{ph}}{P_{opt}} = \frac{\eta\lambda}{1.24} \tag{2.20}$$

The photogenerated current from a photodetector between the wavelengths from λ_1 to λ_2 can be calculated from

$$I_{ph} = \int_{\lambda_1}^{\lambda_2} \mathcal{R}(\lambda)P(\lambda)d\lambda = \mathcal{R}_p \int_{\lambda_1}^{\lambda_2} \hat{\mathcal{R}}(\lambda)P(\lambda)d\lambda \tag{2.21}$$

where P is incident light power, $\hat{\mathcal{R}}(\lambda)$ is the normalised responsivity at wavelength of λ, $\mathcal{R}_p$ is peak responsivity value which is written as

$$\mathcal{R}_p = \frac{I_{ph}}{\int_{\lambda_1}^{\lambda_2} \hat{\mathcal{R}}(\lambda)P(\lambda)d\lambda} \tag{2.22}$$

The responsivity need to be maximised to improve the output signals. Some photodetectors including avalanche photodiodes and photoconductors have internal gain which can improve the responsivity by a factor up to 10^6, with a penalty of added noise.

To investigate the performance of a photodiode, the device noise also needs to be studied. The device noise consists of shot noise and thermal noise. Besides incident optical signal, background radiation is also absorbed to induce some photocurrent, I_b. These photocurrents and device dark current, I_d, (see details in section 3.1) due to thermally generated dark carriers all contributes to the shot noise which is given by

$$< {i_s}^2 > = 2q\left(I_d + I_{ph} + I_b\right)B \tag{2.23}$$

where B is the bandwidth. The thermal noise is given by

$$< {i_T}^2 > = \frac{4k_BT}{R_{eq}} \tag{2.24}$$

where R_{eq} is equivalent resistance of device. The signal to noise ratio (SNR) can be written as

$$SNR = \frac{{I_{ph}}^2}{{i_s}^2 + {i_T}^2} \tag{2.25}$$

The noise equivalent power is defined as (SNR = 1 and B = 1 Hz)

$$NEP = \frac{hc}{\eta}\sqrt{\frac{2(I_d + I_b + \frac{2k_BT}{qR_{eq}})}{q}} = \frac{1}{\mathcal{R}}\sqrt{2q(I_d + I_b) + \frac{4k_BT}{R_{eq}}} \quad (2.26)$$

This value is limited by device dark current and background noise which should be minimised to improve the device sensitivity.

The detectivity of device, D^* is crucial parameter for consideration in a practical application, taking into account both responsivity and detector noise. This is expressed as

$$D^*(\lambda) = \frac{\sqrt{AB}}{NEP} = \frac{\mathcal{R}(\lambda)\sqrt{AB}}{\sqrt{2q(I_d + I_b) + 4k_BT/R_{eq}}} \quad (2.27)$$

Where A is the detector area and B is the bandwidth. This is a common parameter for comparing detector performance including both signal and noise. The value needs to be maximised to improve detector performance.

2.3.2 Avalanche photodiode

Avalanche photodiodes are widely used in many applications due to its internal gain generated by impact ionisation. They also have high bandwidth. They are operated at high reverse bias voltages where avalanche processes occur. Excess avalanche noise is introduced due to the randomness of the avalanche process. Since a high gain is accompanied by multiplied shot noise, it is important to consider the excess noise to achieve high performance APDs.

The mechanism producing the multiplication in APDs is called impact ionisation, as shown in Figure 2.4. In this process, the injected carriers accelerated in the electric field and gain energy from the field. When the energy exceeds the impact ionisation threshold energy new electron-hole pairs are generated via collision with the lattice atoms. The initial carriers and newly generated carriers repeat the ionisation process until an avalanche of carriers is produced. The ionisation coefficients refer to the probabilities of electrons and holes to impact ionise within per unit length, which can be defined as α and β for electrons and holes, respectively. The ionisation coefficients depend on device structure, temperature of device and electric field. For a given device temperature,

ionisation coefficients for carriers are mainly determined by the electric field which is widely used assumptions in the local model.

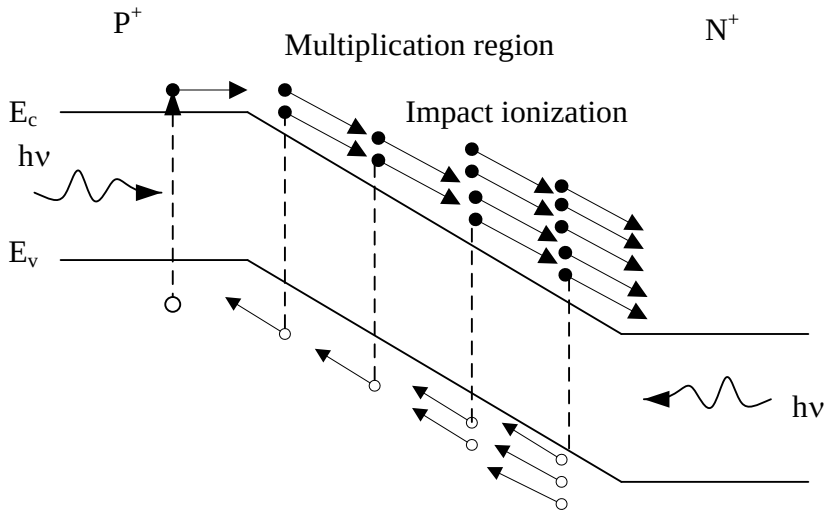

Figure 2.4 Impact ionisation process in a *p–i-n* APD

In the local model where the ionisation coefficients are solely dependent on local electric field, the avalanche gain due to carrier injection at any position can be calculated for a given arbitrary electric field profile. For ideal devices, the electric field is assumed uniform in the multiplication region, the multiplication factor [7] by a carrier injected at position *x* is given by

$$M_x = \frac{(\beta - \alpha)\exp[(\beta - \alpha)x]}{\beta - \alpha\exp[(\beta - \alpha)w]} \tag{2.28}$$

where *w* is avalanche region thickness. Therefore, the avalanche gain due to pure electron and pure hole injection, M_e and M_h, can be calculated

$$M_e = \frac{\beta - \alpha}{\beta - \alpha\exp[(\beta - \alpha)w]} \tag{2.29}$$

$$M_h = \frac{\alpha - \beta}{\alpha - \beta\exp[(\alpha - \beta)w]} \tag{2.30}$$

Two special cases will be discussed here. For electron-only ionisation process where β was set to zero, the electron avalanche gain becomes

$$M_e = \exp(\alpha w) \tag{2.31}$$

The other special case where $\alpha = \beta$, the gain is

$$M_e = M_h = 1/(1 - \alpha w) \tag{2.32}$$

The breakdown voltage is defined as the voltage which avalanche gain approaches infinity and can be calculated by equating the denominator of equation (2.29) to zero, i.e.

$$\exp[(\beta - \alpha)w] = \beta/\alpha \tag{2.33}$$

It is worth noting that the breakdown voltage is independent of the primary carrier injected location while the multiplication does.

Since the impact ionisation process is random, the multiplication factor due to the process is also variable in avalanche region. The fluctuations of this avalanche process results in excess avalanche noise which reduces the signal to noise ratio of system. The randomness of the positions of ionisation events by initiating carriers, leads to a distribution of avalanche gain around mean multiplication factor. The gain in above section is all considered mean avalanche gain, *M*. The excess noise factor can be described as

$$F = \frac{< G^2 >}{< G >^2} \tag{2.34}$$

where $<G^2>$ is the mean value of squared multiplication factor, $<G>^2$ is the squared mean multiplication factor.

In McIntyre's local model [8], the excess noise factor *F* for electron injection can be described in terms of multiplication factor *M* with constant ionisation coefficient ratio *k* in the whole avalanche region

$$F = kM + \left(2 - \frac{1}{M}\right)(1 - k) \tag{2.35}$$

where $k = \alpha/\beta$ for hole injection and $k = \beta/\alpha$ for electron injection. The small value of *k* is desirable for minimizing excess noise effect. In addition to multiply the signal, the internal gain also introduces more noise to the detector. The shot noise is multiplied by the avalanche gain, giving by

$$< {i_s}^2 > = 2q\left(I_d + I_{ph} + I_b\right)M^2FB \tag{2.36}$$

The thermal noise from an avalanche photodiode is the same as photodiode which is shown in equation (2.24). Thus, the *SNR* from avalanche photodiode is improved, providing better performance than conventional photodiode.

2.3.3 Single photon avalanche photodiode

Besides the linear mode, the APD can also operate above its breakdown voltage, known as the Geiger mode. In this mode, it is called single photon avalanche photodiode. Figure 2.5 shows a SPAD operation diagram. In Geiger mode operation, the detector is reverse

biased at voltage V_a above breakdown voltage V_{bd}. The electric filed is very high but no free carrier is present. When a single carrier generated by a photon or one of the dark current mechanism in section 3.1 is injected into high electric field region, it is accelerated and impact ionized quickly, building up a self-sustaining avalanche process. In this state, the avalanche current increases rapidly. This current pulse can be detected using a threshold detection circuit. Upon detection, the avalanche event must be quenched by lowering the bias voltage below the breakdown voltage.

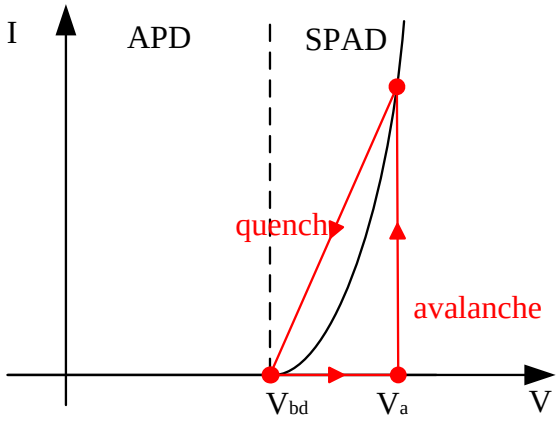

Figure 2.5 SPAD operation diagram

2.3.3.1 Single photon detection efficiency and dark count rate

Several parameters including photon detection efficiency (*PDE*), dark count rate (*DCR*) and recovery time are used to characterise the single photon detectors. Single photon detection efficiency is defined as the probability of detecting the avalanche event due to an absorbed photon, and is given by

$$PDE = \eta \times P_b \tag{2.37}$$

where P_b is avalanche breakdown probability and η is the external quantum efficiency. Avalanche breakdown probability is defined as the probability of a carrier triggering an avalanche event, which strongly depends on the electric field and temperature. It increases with applied reverse bias. The external quantum efficiency accounts for the probability that an injected photon is absorbed by the detector and photogenerated carrier diffuses to depletion layer without being recombined. This depends on the semiconductor absorption coefficient and diffusion length, respectively.

The dark count rate is number of avalanche events trigger by dark carriers within 1 second. As the counter circuit cannot distinguish the avalanche events triggered by dark carrier and photon generated carriers, the dark count rate is considered as noise in photon counting measurement. A bulk dark current arising from thermal generation-recombination processes and band-to-band tunnelling can contribute to dark count. Surface leakage current can only increase dark current but not dark counts, unless it exceeds the threshold value in the detection circuit. The dark count rate increases with increased reverse bias due to increased breakdown probability and more thermally generated dark carriers. The dark count rate also increases with SPAD operation temperature. Thus, the SPAD can be operated at low temperature to reduce the internal noise from the dark count rate.

2.3.3.2 After-pulsing

After-pulsing is the generated false counts due to the avalanche events triggered by carriers released by traps in the SPAD. During an avalanche event, these secondary generated carriers may be trapped in the deep levels (defects in semiconductor), and when released at a later time, they can contribute to false avalanche counts, producing higher noise in the measurement. The after-pulsing effect can be minimised by increasing the avalanche off time using low frequency operation. This can be achieved using a proper quenching circuit which is illustrated in the following part.

2.3.3.3 Quenching techniques

As stated above, when an avalanche event happens, the bias voltage on the detector needs to be reduced to quench the avalanche event. There are several quenching circuits including passive quenching, active quenching and gated quenching technique used to lower the SPAD bias voltage.

In a passive quenching circuit (PQC), a large series ballast resistor is used to quench the avalanche event and recharge the voltage after quenching. A simple passive quenching circuit is shown in Figure 2.6. When an avalanche event is produced by SPAD, the avalanche current causes a voltage drop on the ballast resistor which reduces the bias voltage across the SPAD and quenches the avalanche process. However, there are some

limitations of the simple passive quenching technique. The ballast resistor and detector capacitance form a low pass filter in the circuit. If the resistor is large, the time constant is high resulting in long charge and discharge cycle. On the other hand, if a small ballast resistor is chosen to reduce the time constant, the avalanche current and self-sustaining level is higher. High avalanche current causes more severe after-pulsing problem.

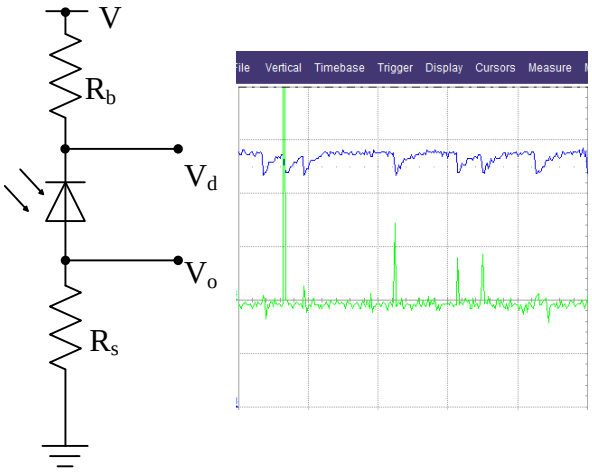

Figure 2.6 A passive quenching circuit (left) and measured diode voltage, V_d and output voltage, V_o (right)

During the recharge time, the photons injected to the detector cannot be detected. To avoid long recharge time, an active quenching circuit shown in Figure 2.7 can be employed. In an active quenching circuit, a comparator is used to control a driver circuit to switch off the bias below breakdown voltage after sensing an avalanche pulse. After a certain avalanche off time, the bias can be restored very quickly. Precise timing control can be achieved through the circuit design. However, this increases the complexity of the circuit and inflexibility for general characterisation of different SPADs.

The simplest mode of SPAD is the so-called free running mode, in which only a DC bias above breakdown is applied on the detector. This operation is useful for very low light level detection through maximizing the sensing time scale. However, the free running mode also brings significant after-pulsing effect. Gated mode operation can reduce after-pulsing effect as well as quench the avalanche effectively when a very short pulse is superimposed on a DC bias such that the SPAD is in switched on for a short duration. The DC bias was chosen to be slightly below the breakdown voltage and AC pulse will define the operating voltage to detect the incident photons. After a gate pulse finished,

the bias on the detector falls below breakdown and the avalanche pulse is quickly quenched away.

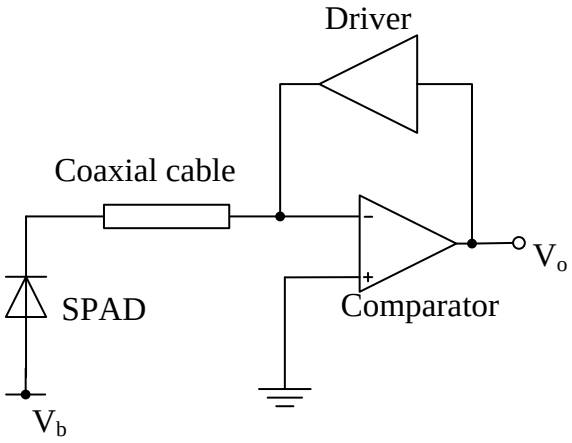

Figure 2.7 An active quenching circuit [9]

2.4 Monte Carlo technique for APD/SPAD design

A Monte Carlo technique has been widely used to simulate the carrier transport in semiconductors. Both band structures and scattering mechanisms are key factors for determining the carrier transport. There are different types of Monte Carlo models which can be distinguished by the implemented band structures in the model. Full band Monte Carlo (FBMC) technique is the most accurate method for carrier transport simulation. It employs the most realistic band structures such as those calculated from a pseudopotential method by Cohen and Bergstresser [10]. However, this approach is computational complex and time consuming. In most applications, the analytical approximation using non-parabolic band structure can also provide sufficiently precise calculation. In an analytical model, three conduction and valance bands have been used to represent the band structure. The energy-wave vector relationship can be described as

$$E(1+\Theta E)=\frac{\hbar^2 K^2}{2m^*} \tag{2.38}$$

$$E=\frac{\hbar^2 K^2}{2m^*} \tag{2.39}$$

for a non-parabolic and parabolic band, respectively, where E is the carrier energy, Θ is the non-parabolic parameter, $\hbar$ is Planck's constant, K is wave vector and m^* is effective mass.

Scattering mechanisms also play a key role in the carrier transport in semiconductors. The main transitions are intravalley and intervalley for electrons due to the electron scattering in the same valley or between valleys. These can be classified as intraband and interband transitions for holes transport. The most important particle for the carrier transitions is phonons. The interactions with ionized impurities become more important, and needs to be considered at low temperatures. Depending on the operation conditions, appropriate scattering mechanism should be accounted for carrier transport prediction.
The first step of simulation is to define the material of interest, then the band structure and initial conditions can be determined. Essential scattering rates have also been calculated for evaluating the probability of each scattering mechanism.

To start the simulation, a carrier with an initial wave vector will experience a free flight. This initial wave vector is determined by its initial energy. To simplify the drift time calculation, Ree *et al.* [11] introduced an artificial self-scattering to the process when there is no scattering mechanism happens after a free flight. Thus the total scattering rates, Γ_t is a constant and energy dependent. After a free drift time, the probability of a carrier suffering a scattering process is given by [12]

$$P(t_d) = \Gamma_t \exp(-\Gamma_t t_d) \tag{2.40}$$

Therefore, the survival probability without undergoing any scattering mechanism after a drift time t_d can be obtained as $1 - \int_0^{t_d} P(t)dt$. The free flight time, t_d, can be solved by generating a uniformly distributed random number, r between 0 and 1 for the survival probability, i.e.

$$t_d = -ln(r)/\Gamma_t \tag{2.41}$$

During the free flight, the carrier is forced to move under the electric field. The wave vector, carrier position and energy are also updated for later process.

At the end of free flight, a scattering mechanism needs to be chosen by another evenly distributed random number between 0 and 1 according to the scattering probability. The occurrence probability of n_{th} scattering mechanism is described by

$$S_n(E) = \frac{\sum_{m=1}^{n} \Gamma_m(E)}{\Gamma_t} \tag{2.42}$$

where $\Gamma_m(E)$ is the scattering rate of m_{th} mechanism. If $r \leq S_n(E)$ and $r > S_{n-1}(E)$, the carrier will undergo the n_{th} scattering mechanism. If all the scattering mechanisms have

not been selected, it will experience a self-scattering. The scattering selection guide is shown in Figure 2.8. After undergoing a scattering mechanism, the carrier energy and state are updated and a third random number is generated to decide the initial wave vector for next free flight. However, if the self-scattering is chosen, the energy and wave vector of the carrier will not change after the free flight. The free flight drift and scattering process will repeat many times until the required conditions has been met to end the simulation. As there is a statistical uncertainty in the process, a number of trials need to be carried out to achieve the convergence in the simulation.

The model can be used to account for non-local effect including changing electric field and dead space effect which is minimum travel distance for carrier to gain sufficient energy to impact ionise. It can be easily implemented to simulate the impact ionisation process such as multiplication and excess noise. The method is also applicable for tracking steady-state drift velocity and impact ionisation energy.

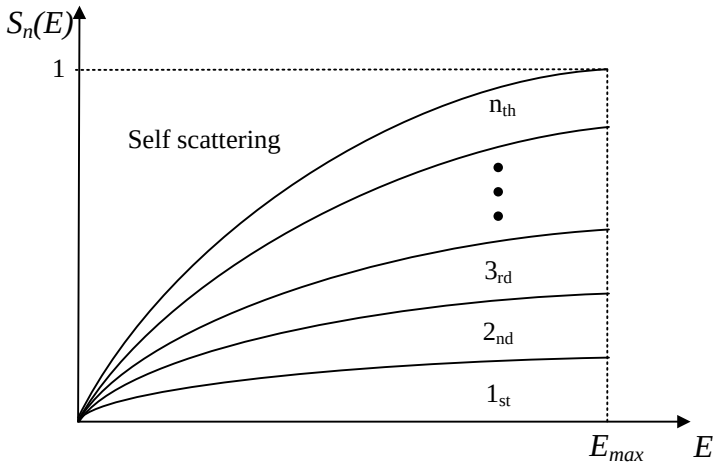

Figure 2.8 The occurrence probability of n_{th} scattering mechanism

References

[1] D. P. Dewitt and G. D. Nutter, Theory and practice of radiation thermometry, New York: John Wiley & Sons, Inc., 1988.

[2] J. Taylor, "Infrared Training Notes - Level 1," Land Instruments International Ltd , 14 Jan 2008. [Online]. Available: http://www.aumico.it/prodotti/files/117.pdf.

[3] Z. M. Zhang, B. K. Tsai and G. Machin, "Industrial applications of radiation thermometery," in *Radiometric temperature measurements. II. Applications*, USA, Elsevier Inc., 2010, pp. 2-54.

[4] S. D. Gunapala and S. Bandara, "Quantum well infrared photodetector (QWIP) focal plane arrays," in *Intersubband Transitions in Quantum Wells: Physics and Device Applications I*, Academic Press, 2000, pp. 197-291.

[5] T. J. Quinn, "Radiation thermometry," in *Temperature*, London, UK, Academic Press, 1990, pp. 332-431.

[6] S. M. Sze and K. K. Ng, Physics of Semiconductor Devices, 3rd Ed., Hoboken, New Jersey: John Willey & Sons, 2007.

[7] W. T. Tsang, Semicondctors and Semimetals- Lightwave Communications Technology, Holmdel, New Jersey: Acadamic Press, Inc., 1985.

[8] R. J. McIntyre, "Multiplication noise in uniform avalanche diodes," *IEEE Trans. Electron. Devices*, Vols. ED-13, no. 1, pp. 164-168, Jan. 1966.

[9] S. Cova, M. Ghioni, A. Lotito, I. Rech and F. Zappa, "Evolution and prospects for single-photon avalanche diodes and quenching circuits," *Journal of modern optics*, vol. 15, no. 9-10, pp. 1267-1288, July 2004.

[10] M. L. Cohen and T. K. Bergstresser, "Band structures and pseudopotential form factors for fourteen semiconductors of the diamond and zinc-blende structures," *Physical Review*, vol. 141, no. 2, pp. 789-796, Jan. 1966.

[11] H. D. Rees, "Calculation of steady state distribution functions by exploiting stability," *Phys. Lett.*, vol. 26, no. 9, pp. 416-417, Mar. 1968.

[12]W. Fawcett, A. Boardman and S. Swain, "Monte Carlo determination of electron transport properties in Gallium Arsenide," *J. Phys. Chem. Solids*, vol. 31, no. 9, pp. 1963-1990, Sep. 1970.

Chapter 3 Experimental methods

This chapter describes many characterisation techniques which can provide useful information related to key properties of a photodetector. The principle experimental methods and theoretical models employed in this work are described. Procedures to extract the information from experimental results are also presented.

3.1 Current-voltage measurements

Current-voltage (*I*-*V*) measurement taken under forward and reverse biases are one of the most basic characterisation methods for a diode or an APD. This was performed using a HP4140B picoammeter or a Keithley 236/237 source measure unit (SMU). The device forward *I*-*V* shows the quality of junction. In an ideal diode the forward dark current is given by [1]

$$I_F = I_o[exp\left(\frac{qV}{nk_BT}\right) - 1] \tag{3.1}$$

where q is the electron charge, V is the voltage drop on the device, T is the temperature in Kelvin, and n is the ideality factor ranging from 1 to 2, depending on diffusion and recombination currents. I_o is saturation current for a p-n diode which is given by

$$I_o = qA(\frac{D_p {n_i}^2}{L_p N_D} + \frac{D_n {n_i}^2}{L_n N_A}) \tag{3.2}$$

where A is device cross-sectional area, D_p and D_n are the diffusion coefficients of holes and electrons, N_D and N_A are the donor and acceptor impurities in n- and p- side, n_i is the material intrinsic carrier concentration, L_p and L_n are the minority carrier diffusion lengths for holes and electrons, respectively.

In real diodes, the series resistance, R_s, can influence the dark current. When the forward voltage increases, R_s and heating effect would become more significant, thus the forward dark current is now described by

$$I_F = I_o[exp\left(\frac{q(V - IR_s)}{nk_BT}\right) - 1] \tag{3.3}$$

By fitting this equation to measured dark current, the series resistance and dominant current component can be determined. The series resistance arise from both semiconductor material and metal-semiconductor contact. To reduce both resistances, highly doped semiconductor cladding layer and good ohmic contact need to be achieved.

The reverse *I-V* measurement is crucial for photodiodes and APDs as they operate under reverse biased to produce the avalanche gain. The reverse *I-V* characteristics provide the device breakdown voltage, V_{bd}, and dark current. The dark current can consist of surface leakage current, tunnelling current, diffusion current and generation-recombination current. All except the surface leakage, depend on the device cross-sectional area. Therefore by dividing the current by area and perimeter, it is possible to analyse the dominance of these dark current components. If the dark current scales with the perimeter, the surface leakage current is obviously dominant, which is undesirable. Improved fabrication via optimised etching and surface passivation will be required to reduce surface leakage. The bulk current scales with area and can divided into diffusion current I_{diff}, generation-recombination $I_{g\text{-}r}$ current and band-to-band tunnelling current $I_{tunn.}$ They are described by [1][2]

$$I_{diff} = I_o \left[exp\left(\frac{qV}{nk_BT}\right) - 1 \right] \tag{3.4}$$

$$I_{g-r} = \frac{qn_iAw}{\tau_{eff}} \tag{3.5}$$

$$I_{tunn} = \frac{(2m_*)^{1/2} q^3 \xi V A}{h^2 {E_g}^{0.5}} exp\left[-\frac{2\pi\alpha_T (m^*)^{1/2} {E_g}^{3/2}}{qh\xi} \right] \tag{3.6}$$

where n_i is the intrinsic carrier concentration, A is the device cross-sectional area, w is the depletion region width, τ_{eff} is the effective carrier lifetime, m^* is the electron effective mass, ξ is the electric field, h is the Plank's constant, E_g is the band gap and α_T is a parameter dependent on the detailed shape of the barrier. The dark current is dominated by I_{diff} and $I_{g\text{-}r}$ at low fields, while at high fields it is dominated either by avalanche breakdown or $I_{tunn.}$ The tunneling current would be large in narrow band gap materials. If I_{tunn} is dominant, a gradual breakdown rather than a sharp breakdown caused by avalanche process is observed. In order to reduce I_{tunn}, materials with large band gaps or thicker intrinsic region to lower the electric field should be implemented in APD design.

3.2 Capacitance-voltage measurements

Capacitance-voltage (*C*-*V*) measurements were carried out using a HP4275LCR meter operating at 1 MHz with a 40 mV amplitude AC bias superimposed over a DC bias. The device capacitance with an area of *A* is given by Gauss's law as,

$$C = \frac{\varepsilon_0 \varepsilon_r A}{w} \tag{3.7}$$

where ε_0 and ε_r is the vacuum permittivity and relative dielectric permittivity. Assuming a single sided abrupt junction, the doping concentration of avalanche region is also given by

$$N = \frac{2}{q\varepsilon_0 \varepsilon_r A^2}\left[\frac{dV_t}{d\left(\frac{1}{C^2}\right)}\right] \tag{3.8}$$

V_t is total reverse bias including built-in potential, V_{bi}. By plotting $1/C^2$ against voltage, V_{bi} is obtained by the interception at $1/C^2 = 0$. Figure 3.1 shows an example of how the built-in potential is derived from the plot of $1/C^2$ versus *V* of a Si *p*-*i*-*n* diode. It shows a built-in potential of 1 V for Si diode.

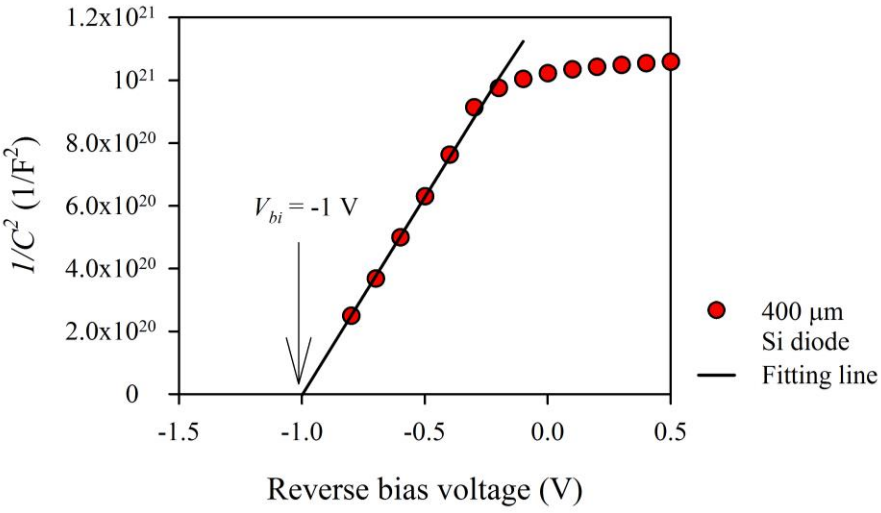

Figure 3.1 $1/C^2$ versus *V* of a Si diode with a diameter of 400 µm.

For *p*-*i*-*n* diodes, the V_{bi} cannot be extracted once the device under test is fully depleted to both cladding layers. The *C*-*V* is also used to estimate the doping profile and electric field profiles of diode. The gradient of the electric field, is given by Poisson equation,

$$\frac{d\xi}{dx} = \frac{qN}{\varepsilon_0 \varepsilon_r} \tag{3.9}$$

where N is the activated dopant density. Using this equation with adjustable parameters in layer doping concentration and layer thickness, the depletion width and electric field profile can be calculated at each bias.

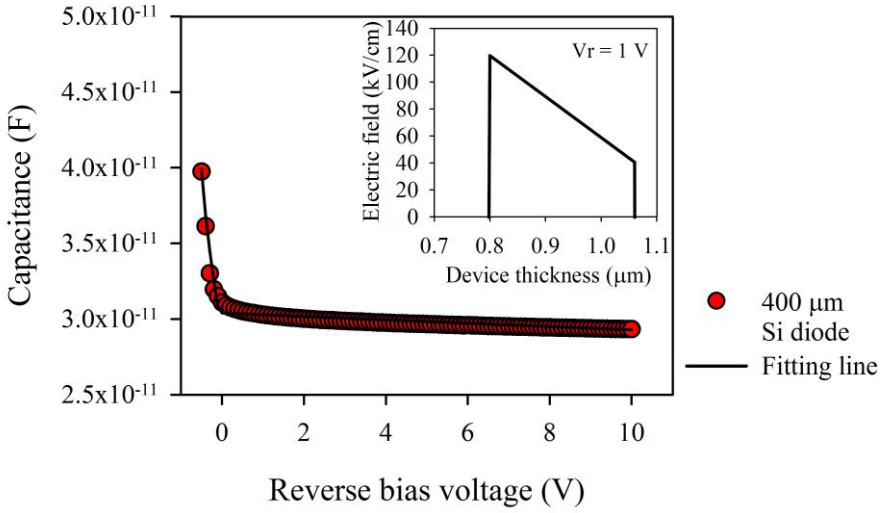

Figure 3.2 *C-V* characteristic of a Si *p-i-n* diode with a diameter of 400 μm. Inset figure shows calculated electric field at reverse bias of 1 V.

Figure 3.2 shows measured *C-V* data of Si *p-i-n* diodes, fitted by three region approximation. It is obvious that there are two gradients in the *C-V* plot. The capacitance in the forward bias drops dramatically with bias, due to an extremely low carrier concentration in the intrinsic region. With increasing reverse bias, the capacitance value reduces slowly since the depletion region has extended into both cladding layer, resulting in a shallow gradient, determined by doping concentrations in the p- and n- cladding regions. By using the above Poisson equation, the absolute capacitance values can be well fitted. Based on the estimated doping concentrations in the three layers and intrinsic region thickness, electric field profile at a given bias is predicted. The inset diagram illustrates the electric filed profile at V_r = 1 V. Depending on *C-V* characteristics, the diode can also be divided into several regions to obtain a better *C-V* fitting when the doping level is not uniform.

3.3 Responsivity and detectivity measurement

Besides *I-V* and *C-V* characterisations, the responsivity measurement of a photodetector also needs to be performed. The photocurrent needs to be measured and discriminated

from the device dark leakage current. It can be measured under DC conditions if device leakage current is sufficiently low. Usually the photocurrent should be at least 2 orders of magnitude higher the leakage current for DC method to be deem acceptable. Otherwise, phase sensitive detection (PSD) method needs to be employed to measure the photocurrent when the device suffers from high leakage current, such as narrow band gap photodetectors.

3.3.1 PSD technique

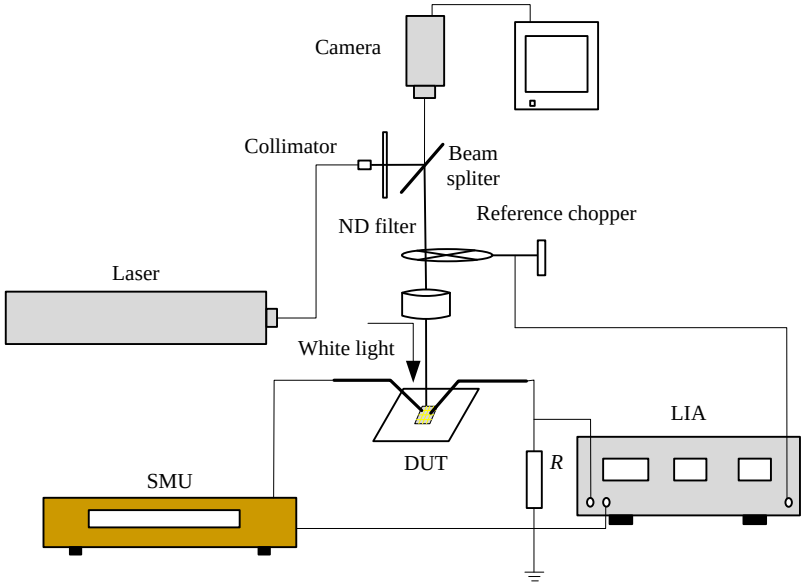

Figure 3.3 The schematic diagram of PSD measurement setup

A PSD measurement setup used in this work is shown in Figure 3.3. In this measurement, visible or IR lasers were used to illuminate the device under test (DUT). This optical signal was then chopped at a frequency of 180 Hz to induce an AC photocurrent. The SMU used to apply a reverse bias voltage on the device and a resistor. Thus the generated AC photocurrent from device went through the resistance and induced a voltage drop on the resistance and finally fed into the lock-in amplifier. The SR830 lock-in amplifier (LIA) was utilised in this measurement which can successfully measure the photocurrent, even in the presence of a dark leakage current up to three orders of magnitude higher than the photocurrent.

In the PSD technique, the LIA generates a sine wave signal at the reference frequency and multiplies this by input signal at the same frequency. After a low pass filter, the

components at other frequencies are all removed except the component at reference frequency. The LIA measures the first sine component of the signal at frequency of interest. It is well known that any input signal can be represented as the sum of many sine waves of differing amplitudes, frequency and phases, called Fourier's series [3]. For example, if the input signal is an ideal square wave with a peak-peak voltage of V_{pp} at a frequency of f_{ref}, it can be expressed as

$$V(t) = \frac{2V_{pp}}{\pi} \sum_{N=1,3,5\ldots} \frac{1}{n} \sin(2\pi f_{ref} nt) \tag{3.10}$$

The LIA displays the input signal in Volts Root Mean Square (RMS) value of the first sine wave at f_{ref} and the output from LIA is

$$V_{LIA} = \frac{2V_{pp}}{\sqrt{2}\pi} \tag{3.11}$$

Therefore, the photocurrent I_{ph} from device across the resistor is given by

$$I_{ph} = \frac{V_{LIA} \times \sqrt{2}\pi}{2R} = \frac{V_{pp}}{0.45R} \tag{3.12}$$

Once photocurrent is obtained, the responsivity at a certain wavelength is calculated by equation (2.20). The incident optical power at a single wavelength can be measured using a Thorlabs PM100D optical power meter with sensors detecting 0.19-25 μm.

3.3.2 Detectivity

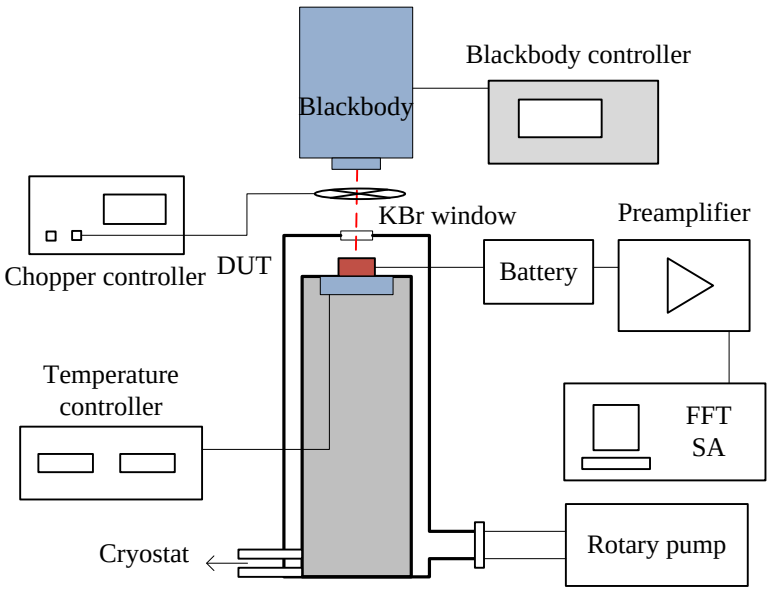

Figure 3.4 The schematic diagram of photocurrent setup

Figure 3.4 shows a schematic of setup for measuring IR photocurrent. Thermal radiation

was emitted by an IR-563/301 blackbody source at a temperature of 800 °C and chopped at a frequency of 810 Hz. The device was placed in a Helium cryostat if cooling is required and biased using batteries. The photocurrent generated from device was amplified using a preamplifier and measured by a Fast Fourier Transform (FFT) Spectrum analyser (SA). The Spectrum analyser can derive weak photocurrent from the dark current. During the measurement, the total photocurrent from the detector can be measured by Spectrum analyser. The incident power of per unit wavelength radiation, $P(\lambda)$, which can be calculated from the product of Planck's equation and instrument factor in equation (2.8), given by [4]

$$P(\lambda) = L_{b,\lambda}(\lambda, T) sin^2\left(\frac{\theta}{2}\right) AT_f(\lambda)(1-r)Ccos(\varphi) \quad (3.13)$$

where $T_f(\lambda) = 0.87$ is the transmission factor of KBr window as a function of wavelength (measured using an optical power meter) for the wavelength range, and the chopper factor F_c = 0.37 in this work. Therefore, the peak responsivity could be determined from equation (2.22). The detectivity can be calculated from the responsivity and noise current using equation (2.27).

3.4 Spectral response

The spectral response illustrates the relative responsivity of the photodetector as a function of wavelength of the signal. For a conventional photodiode, the spectral response cut-off is determined by band gap of the material. For example the cut-off wavelength of silicon (Si) is 1.1 μm. In this thesis, two systems were used to perform the spectral response measurement.

3.4.1 Monochromator setup

The iHR monochromator is adopted for the spectral response measurement. The monochromator is designed in Czerny-Turner configuration [5], shown in Figure 3.5. The input light source is focused onto the entrance slit and directed to a collimating mirror. As the diffraction angle will be different for light with different wavelengths. The reflected light from collimating mirror is then diffracted and split by a diffraction grating into individual wavelengths at different positions. These lights with individual wavelengths are finally focused by a concave mirror and directed out at the exit slit. The

wavelength of the light output is selected by rotating the diffraction grating. The optimisation of system optical path to eliminate the re-diffracted light travelling through the exit port was done in this system and can be precisely controlled by computer.

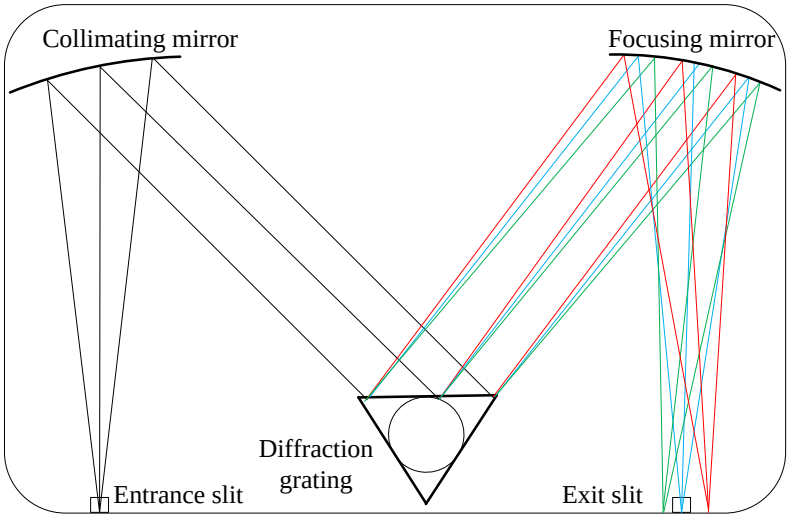

Figure 3.5 Czerny-Turner monochromator

As a dispersive element, the diffraction grating is normally used by a monochromators and spectrometers. It consists of a set of grooves with different shape structure in periodic space. The fundamental grating equation is given by [6]:

$$l\lambda = d(sin\ \theta_i\ + sin\ \theta_d) \tag{3.14}$$

where d is the groove spacing in a grating, θ_i and θ_d are incident and diffractive angles, l is the diffraction order. The detailed diffraction distribution also depends on the grating structure and number of grooves in grating. Blaze grating is designed for achievement of maximum efficiency at a chosen wavelength. Blazed grating profiles are calculated on the basis of Littrow condition where the incident angle equals to the diffraction angle. A grating blazed at a certain wavelength in first order is equally blaze in the subsequent higher orders of one of integer's wavelength points, such as a 1000 nm blazed grating in first order is also blazed at 500 nm in second order and so on [6]. Therefore, in a real measurement, a high pass optical filter need to be used to remove the high order components. Generally, for blazed gratings the strength of a signal is reduced by 50% at two-thirds the blaze wavelength, and 1.8 times the blaze wavelength [6].

The ability of splitting adjacent wavelengths of a monochromator is characterised by bandpass and resolution. The bandpass of the instrument is the isolated spectral interval

in wavelength. In a monochromator, it is defined as a full width at half maximum of the spectrum which can go through the exit slit. This depends on several factors, such as entrance and exit slit widths, linear dispersion of the grating and system aberrations.

The dispersion angle of a grating is defined as the change of the diffractive angle in response to a wavelength fluctuation. It can be written as [6]

$$\frac{d\theta_d}{d\lambda} = \frac{l}{d \cdot \cos\theta_d} \tag{3.15}$$

High dispersion is desirable to improve the resolution which can be achieved by small groove spacing and higher orders or using higher diffractive angle. The product of angle dispersion and exit focal length is line dispersion, which is associated with the resolving fine spectral ability of the monochromator. This is known as

$$\frac{d\lambda}{dx} = \frac{d \cdot \cos\theta_d}{lf_c} \tag{3.16}$$

where *dx* is the unit interval in mm. Finally, the system bandpass, *BP* is determined by the product of line dispersion and entrance or exit slit width, w_s,

$$BP = \frac{w_s d \cdot \cos\theta_d}{lf_c} \tag{3.17}$$

By narrowing the entrance and exit slit widths to approach bandpass minimum, the monochromator resolution can be optimised.

Figure 3.6 shows the spectral response setup using a monochromator. A tungsten lamp or globar source is used to provide continuous lights, focusing into monochromator. The monochromator has a focal length of 340 mm and there are two customised exit slit ports for characterisation of devices on wafer or packaged photodiodes. It contains gratings with 1800, 600, and 300 grooves /mm which blazed at 400 nm, 1 μm and 2 μm, respectively. This can be chosen for scanning spectral range of interest. An entrance or exit slit widths of 2 mm or 4 mm is flexible used for different power intensities, corresponding to a bandpass of 9.8 nm or 19.6 nm at a blaze wavelength of 1 μm. A focusing lens is placed after the exit port to focus signals onto device. Cut-off filters are used in this setup to remove high order signals. In the cases with high leakage current, optical chopper is implemented in the PSD measurement. Devices on wafer or packaged are placed or mounted on a XYZ stage. During this measurement, a commercial photodiode with known spectrum is always used to calibrate the power distribution with

wavelength from this system. The spectral response of the DUT can be corrected and normalised using the calibrated photodiode. Finally, the responsivity of a certain wavelength is measured and cross checked using lasers in the setup shown in Figure 3.3.

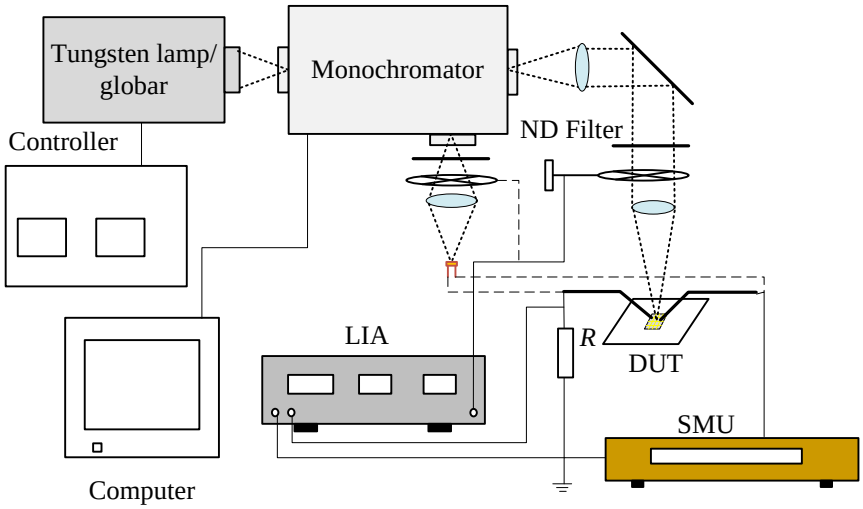

Figure 3.6 Monochromator setup for spectral response measurement

3.4.2 Fourier Transform IR (FTIR) setup

In addition to a monochromator, FTIR which adopts a Michelson interferometer as shown in Figure 3.7 is also widely used for spectral response measurement, particularly for wavelengths above 3 μm. Rather than shining monochromatic light onto the device, this system shines IR radiation from a hot ceramic. In the FTIR, the IR beam is split onto a static and a movable mirror by a beam splitter. Then the reflected light from both mirrors is combined and directed onto the device. As the mirror moves, the reflected light from static mirror and movable mirror stacked or offset with respect to the position of movable mirror. The output beam from the interferometer therefore changes with time. During the measurement, the process is repeated several times and presents different spectrum from the device. The interferogram is converted absorption information at each wavelength.

The schematic diagram of spectral response setup is shown in Figure 3.8. A Varian FTIR adopted a ceramic light source which can transmit radiation from 1.7 μm to 25 μm [7]. The output beam from FTIR was collected and focused by a parabolic mirror onto the device. The device under test was sealed into a chamber and vacuumed by a rotary pump.

A KBr window with a diameter of 10 mm was used as chamber's optical window, giving a uniform IR radiation transmission up to 20 μm. The device was biased by a ±5 V using a Standford Research SR 570 low noise preamplifier source and additional battery stage if higher voltage is required, and then the output signal was amplified before being fed back to FTIR and finally sorted out by the computer. In this setup, cooling the chamber can be performed by Helium closed cycle cryostat down to 10 K for the spectrum temperature dependence measurement. A heater and temperature sensors were placed under the mounting plate to control the device temperature.

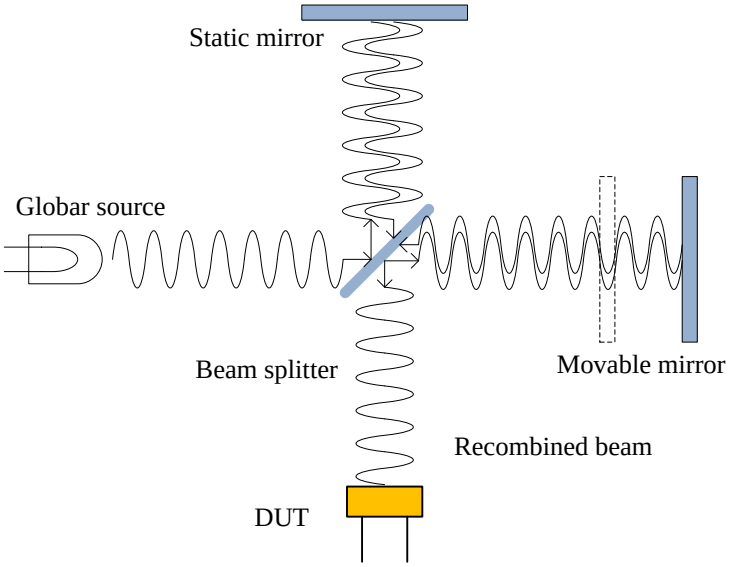

Figure 3.7 Schematic diagram of FTIR operation

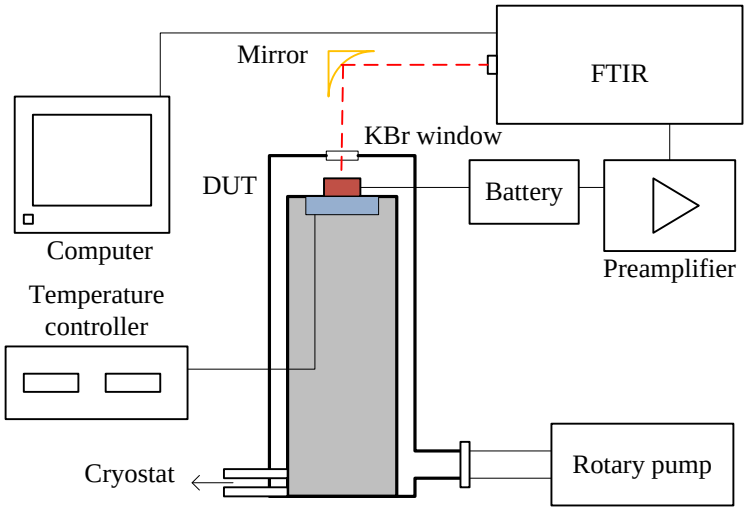

Figure 3.8 Schematic diagram of FTIR spectral response measurement setup

3.5 Photomultiplication measurement

For APDs, avalanche gain is main factor which need to be measured. This measurement can be performed using the setup shown in Figure 3.3. Once the photocurrent is obtained, the avalanche gain can be calculated by

$$M(V) = \frac{I_{ph}(V)}{I_{pr}(V)} \tag{3.18}$$

where *M(V)* is the avalanche gain at a certain reverse bias, I_{pr} are the primary photocurrent generated by primarily generated under unity gain conditions.

In the practical photomultiplication measurement, several factors need to be considered to ensure the accuracy of final results. First of all, pure carrier injection is important for avalanche gain analysis, so that the relative magnitude of electron and hole ionisation coefficients can be determined. To ensure this, it is desirable to focus a laser spot (that is smaller than the device) on to the top p-type or n-type layer in the *p-i-n* or *n-i-p* diodes to avoid light injection in mesa sidewall for pure electron or hole injection. To ensure the light is fully absorbed in the top cladding layer, it is crucial to choose appropriate laser wavelength and device cladding layer thickness. Measurements performed on different sizes of device are useful to check the purity of carrier injections.

In the ideal case, the avalanche gain of devices is independent of optical power density. However, at high reverse bias and high power density, the avalanche gain might vary due to heat dissipation issues. As impact ionisation process depends on the temperature, the avalanche gain either increase or decrease with heating. For instance high power dissipation in small area may increase device temperature. Thus the real multiplication measurement could suffer from heating effect. Performing the measurement under different optical powers allows analysis of this heating effect. Monitoring the stability of the photocurrent with time is another method to check the heating effects.

The series resistance effect in the circuit is another factor which may lead to inaccuracy in the multiplication measurement. When the applied reverse bias on an APD approaches the breakdown voltage, the photocurrent increased significantly. This can cause a voltage drop on the series resistance, reducing the actual bias voltage in the device. This issue mainly comes from the contact series resistance due to poor ohmic contact between

metals and semiconductors. The resistor in the Figure 3.3 also contributes to this issue which need to be carefully selected to avoid the underestimation of avalanche gain.

The photocurrent increases with applied bias due to impact ionisation and improved collection efficiency. To calculate the avalanche gain, the primary photocurrent under pure injection conditions, due to primary carriers generated in the cladding which diffuse to high electric field region, needs to be determined accurately. The collection efficiency increases due to longer depletion width at higher reverse bias and must be taken into account in the calculation. The primary photocurrent can be expressed as [8]

$$I_{pr} = \frac{qG_0}{\cosh(\frac{L}{L_d})} \tag{3.19}$$

where G_0 is the generation rate of photocarriers in the illuminated surface, L is the distance between the illuminated surface and depletion region edge, and L_d is the minority carrier diffusion length. When the $L_d >> L$, this equation can be simplified to a linear equation, $I_{pr} = aV+b$. The primary current increases linearly with reverse bias voltage and can be derived by linear extrapolating the photocurrent from low bias voltage. Finally, the avalanche gain can be calculated using equation (3.18).

3.6 Radiation thermometry measurement

3.6.1 Photocurrent mode

Figure 3.9 shows the schematic diagram of radiation thermometry setup. A calibrated IR-563/301 blackbody source with an emissivity > 0.99 (or Land Instruments Landcal P80P) was used for blackbody temperature range of 50-1050 ºC. The aperture of the blackbody source was set to 10.16mm or 7.5mm in diameter and the photodetector was place at 300 mm away from the blackbody source. A mechanical chopper was used to modulate the signal from the blackbody at 420 Hz and the modulated signal was focused by a ZnSe lens (Ø1" Plano-convex lens, f_c = 50 mm) onto the device. The photocurrent from the photodetector was amplified by a transimpedance amplifier circuit with an overall gain of 10^6 V/A. The output signal from the amplifier was recovered using the PSD method by a SR830 lock-in amplifier. This measurement was performed at room temperature and air-exposed.

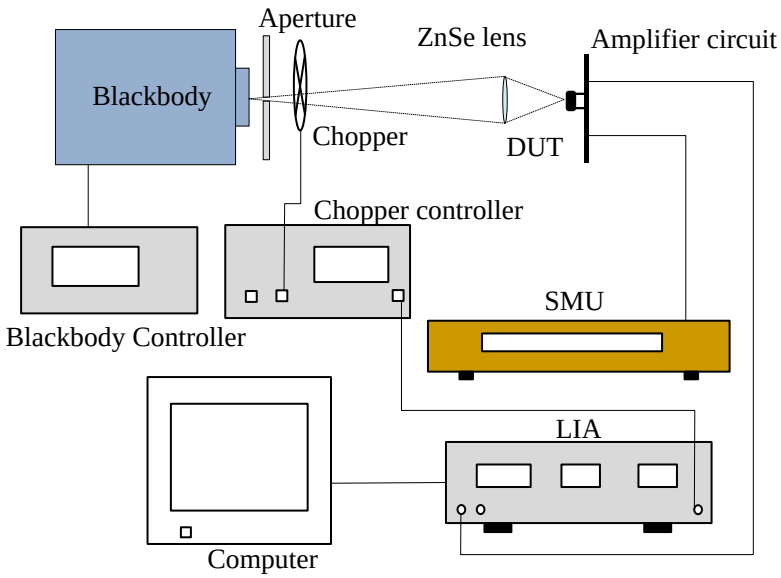

Figure 3.9 The schematic of radiation thermometry measurement setup

The electronic noise of the detector-amplifier combination in the system and influence of laboratory ambience (e.g. temperature and humidity) can be assessed as a temperature error. This value was calculated from the ratio of percentage error of the output voltage to the percentage change in output for a 1 °C rise in the target temperature, known as Percent-per-Degree [9], [10]. To assess the error in the output voltage we measured the largest peak to peak voltage, (V_{pp}) and the mean output voltage <V> as shown in Figure 3.10. The percentage error of the output voltage is then defined as (V_{pp}/2)/<V> multiplied by 100 while the Percent-per-Degree is defined from equation (2.11) which is given by

$$\%/℃ = 100 \times \frac{c_2}{\lambda T^2} \tag{3.20}$$

where λ is the effective operational wavelength of a single-channel thermometer. This effective wavelength is derived from the gradient of the natural logarithm of output voltage plotted as a function of 1/T [11], [12]. It is a method based on Wien's law, by approximating broad band wavelengths into a single monochromatic wavelength [13]. The ratio thermometer can be considered to behave in the same way as a single-channel thermometer whose effective wavelength is given by equation (2.17).

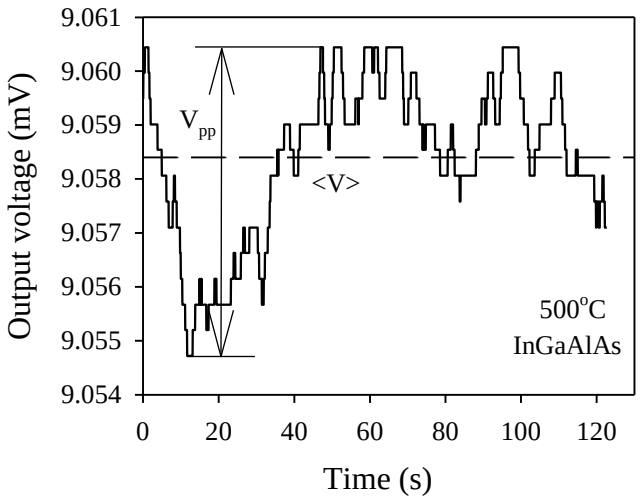

Figure 3.10 Fluctuations of output voltage during thermometry measurement

3.6.2 Photon counting mode

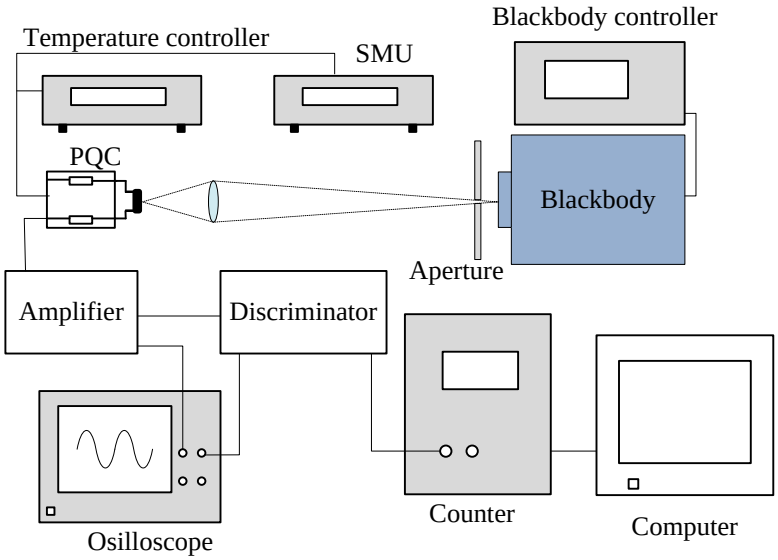

Figure 3.11 Radiation thermometry measurement using photon counting mode

Besides the photocurrent measurement at different blackbody temperature to calibrate the temperature of target, photon counting mode measurement was performed to achieve a lower temperature limit of a radiation thermometer.

Figure 3.11 shows a radiation thermometry setup using photon counting mode. A calibrated IR-563/301 blackbody source was used to provide light signal onto the device. The measured device was mounted into a metal box and connected to a passive quenching

circuit. A Keithley 2400 General-purpose SMU was used to provide DC bias in the circuit. A C30902SH-DTC Si SPAD was operated in a Geiger mode to generate avalanched current pulse where the reverse bias voltage is above its breakdown voltage. The avalanche current pulse generated from the Si SPAD went through a 50 Ω load resister and formed a voltage signal. The voltage was amplified using a low noise preamplifier with a gain of 10 and can be monitored by an Agilent oscilloscope. By setting a threshold voltage, a discriminator was used to distinguish the amplified signal above the threshold and generates a nuclear instrument module (NIM) standard logic signal. Finally, The NIM logic signals generated from the discriminator were calculated by a counter and the number of avalanche pulse was recorded by the computer.

References

[1] S. M. Sze and K. K. Ng, Physics of Semiconductor Devices, 3rd Ed., Hoboken, New Jersey: John Willey & Sons, 2007.

[2] S. R. Forrest, R. F. Leheny, R. E. Nahory and M. A. Pollack, "$In_{0.53}Ga_{0.47}As$ photodiodes with dark current limited by generation-recombination and tunneling," *Appl. Phys. Lett.*, vol. 37, no. 3, p. 322–325, 1980.

[3] "DSP Lock-In Amplifier model SR830," Stanford Research Systems Inc., [Online]. Available: http://www.ece.cmu.edu/~mems/resources/HH1212/SR830m.pdf. [Accessed 12 January 2013].

[4] S. D. Gunapala and S. V. Bandara, "Quantum well infrared photodetector (QWIP) focal plane arrays," in *Intersubband Transitions in Quantum Wells: Physics and Device Applications I*, Academic Press, 2000, pp. 197-291.

[5] "Imaging Spectrometer," Horiba Jobin Yvon Ltd., [Online]. Available: http://www.horiba.com/fileadmin/uploads/Scientific/Documents/Mono/iHR.pdf. [Accessed 12 Januray 2013].

[6]"Diffraction Grating," Horiba Jobin Yvon Ltd., [Online]. Available: http://www.horiba.com/scientific/products/optics-tutorial/diffraction-gratings/. [Accessed 12 January. 2013].

[7] "Varian 7000/7000e FT-IR spectrometers operational / hardware manual," Varian Australia Pty Ltd., March 2005. [Online].

[8] M. M. Wood, W. C. Hojnson and M. A. Lampert, "Use of a schottky barrier to measure impact ionisation coefficients in semiconductors," *Solid State Electron*, vol. 16, no. 3, pp. 381-394, Mar. 1973.

[9] J. Taylor, "Infrared Training Notes – Foundation level," Land Infrared Int. Ltd., UK., Aug. 2010. [Online]. Available: http://www.aumico.it/prodotti/files/117.pdf.

[10] T. J. Quinn, "Radiation thermometry," in *Temperature*, London, UK, Academic Press, 1990, pp. 332-431.

[11] P. Saunders, "General interpolation equations for the calibration of radiation thermometers," *Metroligia*, vol. 34, no. 3, pp. 201-210, Jun. 1997.

[12] J. W. Hahn and C. Rhee, "Interpolation Equation for the Calibration of Infrared Pyrometers," *Metrologia*, vol. 31, no. 1, pp. 27-32, 1994.

[13] P. Saunders, "Uncertainty Arising from the Use of the Mean Effective Wavelength in Realizing ITS-90," *Proc. AIP*, vol. 684, pp. 639-644, 2002.

Chapter 4 An InGaAlAs-InGaAs two-colour photodetector for high temperature sensing

4.1 Introduction

As described in the chapter 1, the ratio thermometer can provide more accurate measurement than the single wavelength thermometer, particularly in cases where the emissivity is not easily obtained, or when there is additional attenuation caused by the presence of an unwanted medium, such as smoke or steam. The ratio thermometer works if the emissivity (and the attenuation factor) is constant across the two chosen wavelength bands [1]. In this case the error due to the reduced emissivity or attenuation is removed and the ratio of electrical outputs from the two photodetectors is a function of source surface temperature alone [2]. The tandem Si-InGaAs photodetector shows good linearity and can be used for single spot measurement at temperatures above 400 ^{o}C [3]. Hence the Si-InGaAs photodetector (such as K1713 from Hamamatsu) has been used in a typical single spot ratio thermometer.

The concept of two-colour detection has also been demonstrated to be highly suitable for imaging applications where objects in the imaged scene have different emissivities or are located in an attenuating medium. In some cases the emissivity changes due to composition variation on the surface, such as in the growth of zinc alloy during galvanneal process and induction skull melting of titanium aluminide [4],[5]. In these situations it is impossible to translate the measured photocurrent into target temperature if the measurement is performed using a single waveband detector. Consequently a radiation thermometry system using a two-colour photodetector, which minimises the influence of emissivity, becomes highly attractive for concomitant temperature sensing and thermal imaging. Yamada *et al*. [6] and Mollmann *et al*. [7] successfully demonstrated a two-colour thermal imaging system using an InSb photodetector and narrow band optical filters. Improved accuracy over conventional thermal camera imaging was obtained using the two-colour measurement. Inclusion of filters, such as using of a filter wheel, prevents simultaneous measurement at the wavelengths of interest.

Removing the filters can bring further improvements to the two-colour imaging, in terms of simpler optical system, reduced cost and reduced dynamic filters drift and reflections between filters and detector. It is also worth noting that the ratio of signal at the two wavelengths is larger at the shorter wavelength. Consequently for objects with low emissivities, measurement with minimal error is best achieved at short wavelengths [8] and two-colour measurements are normally performed at selected short wavelengths. For applications with high operating temperature above 400 °C, such as furnace wall-tube monitoring [9] or supervision of low emissivity objects in aluminium industry [10], two-colour thermal imagers operating at short wavelengths are desirable.

For a two-colour imaging system at the short wave IR (SWIR) wavelengths the Si-InGaAs tandem photodetector is not a suitable technology for fabrication of imaging arrays, because the large lattice mismatch of 8% between InGaAs and Si [11] makes epitaxially grown InGaAs on Si impractical and stacking Si diode on InGaAs diode (the approach adopted for Hamamatsu K1713) becomes more complicated for large arrays. On the other hand the $In_{1-x-y}Ga_xAl_yAs$ quaternary alloy, which is a direct band gap material, can be easily combined with InGaAs to form two-colour imaging arrays grown on high quality InP substrates. $In_{1-x-y}Ga_xAl_yAs$ also offers several advantages over Si, such as cut-off wavelength tunability from 827 to 1700 nm [12], a higher absorption coefficient, leading to a thinner absorption layer and potential as wavelength tuneable multi-colour spot thermometer, line scanner and eventually extremely accurate thermometer camera.

In this chapter, the first evaluation of an InGaAlAs-InGaAs two-colour photodetector for use in a ratio thermometer is reported. The two-colour detector has a 3-level structure and imposes a stringent fabrication process. Electrical characterisation including current- and capacitance-voltage measurements was performed to evaluate the device performance. The two-colour photodetector thermometry measurement also has been done using the setup in Figure 3.9 and compared to those from a commercial two-colour photodetector. The detector performance as a single thermometer and ratio thermometer was also analysed.

4.2 Device structure and fabrication details

The two-colour photodetector comprises an $In_{0.53}Ga_{0.25}Al_{0.22}As$ (hereafter referred to as InGaAlAs) p^+-i-n^+ diode, with an alloy composition chosen to achieve a cut-off wavelength of 1100 nm, grown on top of an $In_{0.53}Ga_{0.47}As$ (hereafter referred to as InGaAs) p^+-i-n^+ diode, which is capable of detecting wavelengths up to 1700 nm. The InGaAlAs-InGaAs structure, illustrated in Figure 4.1, was grown by MBE on a 2" InP n^+ conducting substrate at the EPSRC National Centre for III-V Technologies at Sheffield.

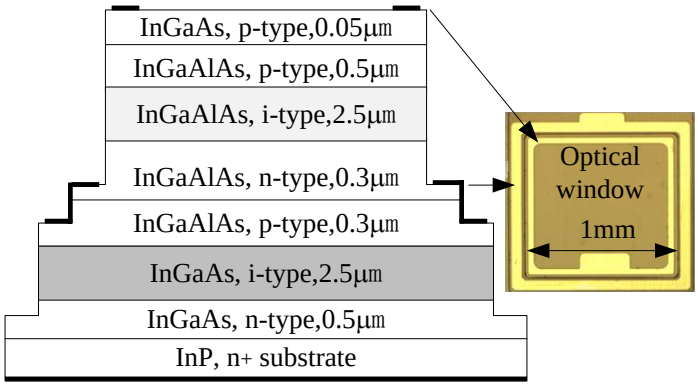

Figure 4.1 The cross-section and top-view of the InGaAlAs-InGaAs two-colour photodetector

Mesa devices, shown in Figure 4.1, were fabricated using standard photolithography. Mesas were fabricated by wet chemical etching using a sulphuric acid: hydrogen peroxide: deionised water (DIW) (1:8:80) solution. Ti-Pt-Au (10 nm/20 nm/200 nm) metal contacts were deposited on the highly doped InGaAs and InGaAlAs contact layers and the substrate, as shown in Figure 4.1. The metal contacts were annealed at 420 °C for 30 s. Surface passivation and anti-reflection coating on the optical windows were not performed. Three device sizes were fabricated to allow analysis of current density. The top mesa sizes are 1 mm × 1 mm (large), 0.5 mm × 1 mm (medium) and 0.21 mm × 0.235 mm (small) while the bottom mesa device sizes are 1220 μm × 1285 μm (large), 720 μm × 1285 μm (medium) and 445 μm × 490 μm (small) as shown in Figure 4.1. The large area devices were subsequently used for optical measurements. Their optically active areas, calculated by excluding the area shielded by the metal contacts, are 0.84 and 1 mm^2 for the InGaAlAs and InGaAs junctions respectively. A full details of fabrication process can be obtained in Appendix A.

4.3 *I-V* and *C-V* characterisation

The room temperature *I-V* measurements were performed on the detectors using a HP4140B picoammeter. Figure 4.2 shows the dark current density of InGaAlAs and InGaAs diodes in this work. For forward *I-V*s, the InGaAlAs show good ohmic contact while the InGaAs junction shows a larger series resistance. At low reverse biases below 0.1 V, bulk current appears to dominate in both set of diodes. At higher reverse biases, bulk current density of 10^{-6} A/cm^2 was obtained in the InGaAlAs, while the inconsistency of the current density in the InGaAs diodes indicates presence of some surface leakage.

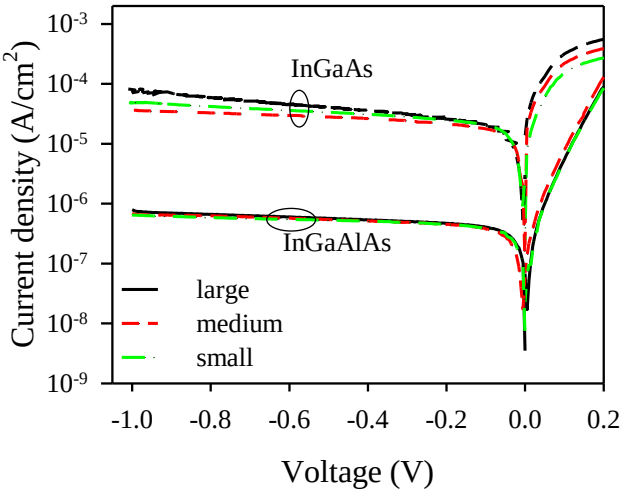

Figure 4.2 Dark current density of InGaAlAs and InGaAs diodes

The device capacitances were also measured at room temperature. Figure 4.3(a) shows the *C-V* results and depletion width as a function of reverse bias derived from *C-V* measurements. The doping densities of both junctions can also be calculated from equation (3.8), as shown in Figure 4.3(b). The InGaAlAs diode achieves full depletion at 0.1 V while the InGaAs diode is fully depleted at 6 V indicating a higher unintentional background doping level of 1×10^{15} cm^{-3} in the InGaAs intrinsic region.

The basic electrical characteristics of two-colour detector at 0 V are summarised in Table 4.1. Parameters from Hamamatsu K1713-09 [13] are also shown for comparison. The higher dark currents of both InGaAs and InGaAlAs diodes and the high background doping level in the InGaAs diode suggest that further growth and fabrication improvements are required.

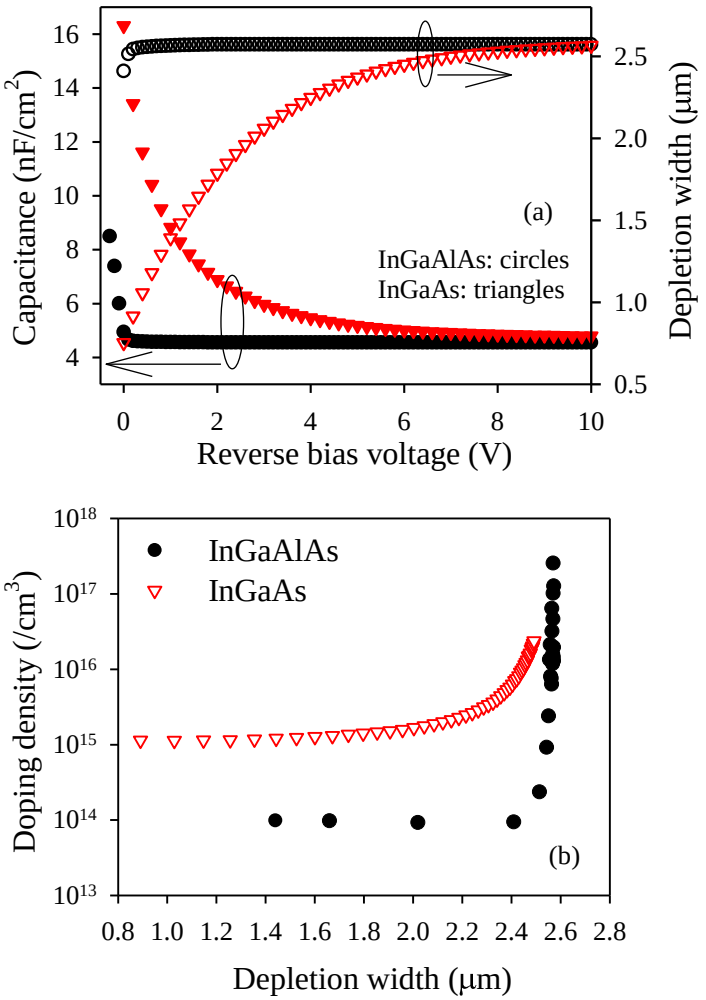

Figure 4.3 (a) Capacitance and depletion width of InGaAlAs and InGaAs photodetector and (b) Doping density of InGaAlAs and InGaAs junctions from large device

Table 4.1 Basic parameters of two-colour photodetector

Detector	Photodiode material	Active area (mm^2)	Dark current I_d at nominal zero bias (pA)	Depletion width at nominal zero bias (μm)
This work	InGaAlAs	0.84	15	2.41
	InGaAs	1	200	0.75
K1713-09	Si	5.76	<10	10.16
	InGaAs	0.785	<10	0.53

4.4 Spectral response

The spectral response of the two-colour photodetector was measured using an iHR320 monochromator with a tungsten lamp light source. Diffraction gratings with blaze wavelengths of 1 and 2 μm were used for spectral measurements of the InGaAlAs and InGaAs diodes, respectively. The photocurrents from chopped 1064 and 1550 nm lasers were also measured using a phase sensitive detection technique [14]. The incident powers onto the device were then measured using an optical power meter, so that the responsivities of both diodes could be calculated.

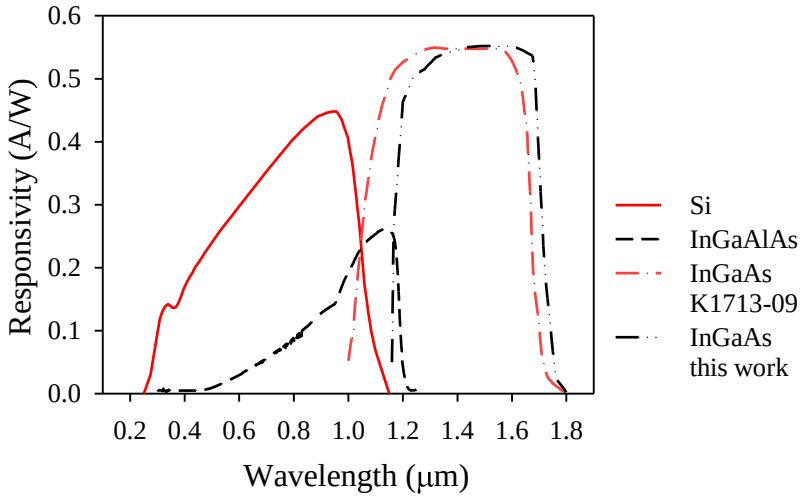

Figure 4.4 Responsivity of photodetectors in this work and commercial K1713-09 photodetector at 0 V

Figure 4.4 shows the typical reponsivities of the InGaAlAs-InGaAs photodetector and the K1713-09 photodetector at 0 V. The measured responsivities at 0 V from the two-colour detector are 0.25 A/W at 1064 nm for the InGaAlAs diode and 0.55 A/W at 1550 nm for the InGaAs diode. At 1064 nm the responsivity is lower than 0.44 A/W, measured in the K1713-09 (Si) diode while at 1550 nm it is similar to that in the K1713-09 (InGaAs) diode. The InGaAlAs diode shows a cut-off wavelength, defined as 50% of the peak intensity, of 1180 nm (slightly longer than the nominal value targeted) while the InGaAs photodetector shows a cut-off wavelength of 1700 nm. These are longer than the cut-off wavelengths of the diodes in K1713-09, most likely due to slight deviation of the alloy composition. The InGaAs diode in this work also shows a narrower spectrum due to higher absorption of the InGaAlAs in the wavelengths of 1100 – 1200 nm.

A longer depletion region width, as shown in Table 4.1, and more efficient carrier collection from the undepleted regions in Si diode gives rise to a higher peak responsivity value than the InGaAlAs diode. The lower peak responsivity is attributed to a poor carrier collection efficiency. Carriers generated in the top InGaAs layer are blocked by the p-InGaAlAs layer. The InGaAs layer in the optical window should be removed to improve the quantum efficiency in InGaAlAs diode. Similarly the thickness of the p-InGaAlAs layer can be reduced to improve carrier collection efficiency.

4.5 Radiation thermometry measurement

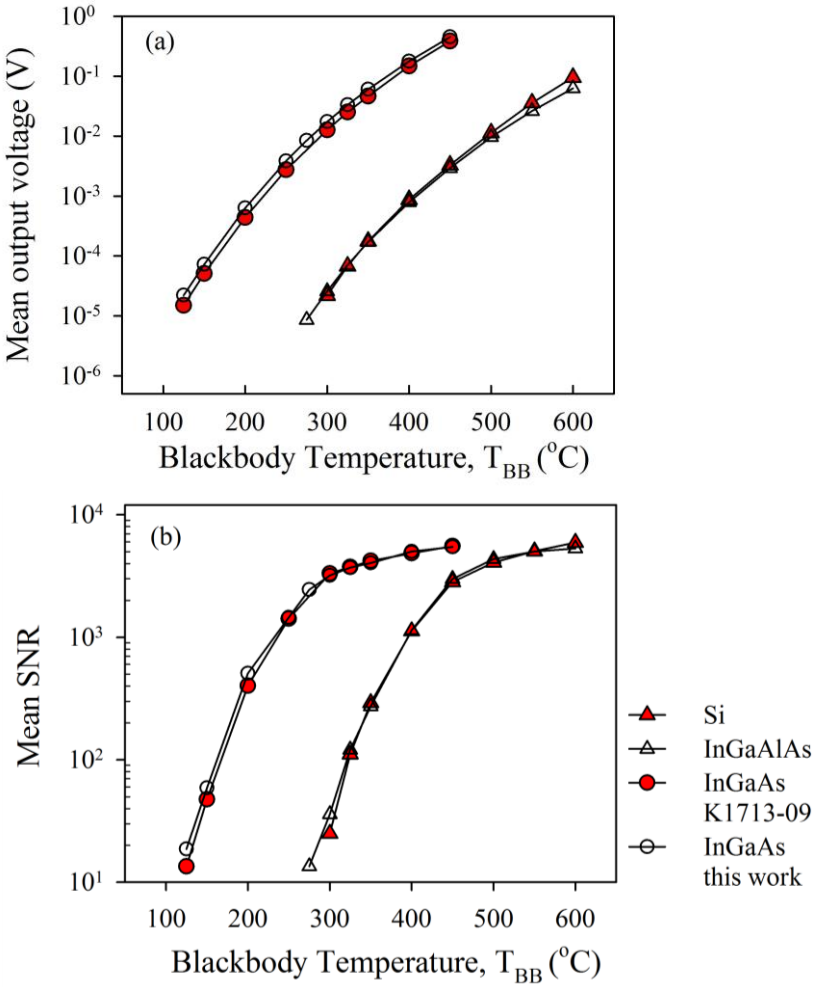

Figure 4.5 (a) The mean output voltage and (b) mean *SNR* of the InGaAlAs-InGaAs photodiode and K1713-09 as a function of the T_{BB}

In order to evaluate the performance of the InGaAlAs-InGaAs two-colour detector as a ratio thermometer, radiation thermometry measurements were also performed using the

setup in Figure 3.9. When exposed to the blackbody source, the mean output voltage of the transimpedance amplifier and the *SNR*, (taken as the ratio of the mean output voltage to the standard deviation of the output voltage) are shown in Figure 4.5. The mean output voltage and the mean *SNR* were calculated from at least 6 sets of data, each with more than 2400 experimental data points, taken over 2 minutes at any given temperature. This allows the diode stability to be confirmed and an accurate mean value to be obtained. *SNR* above 10 was achieved at the lowest measured temperatures of 125 °C and 275 °C for InGaAs and InGaAlAs detectors, respectively. The mean output voltage and the *SNR* appear to be comparable to those obtained from commercial detectors in Figure 4.5. However, closer inspection reveals that the InGaAlAs diode obtained a slightly higher signal at temperatures below 500 °C but lower signal at temperatures above 500 °C, compared to those measured from K1713-09(Si) diode. The signal from the InGaAs diode is also slightly higher than that from the K1713-09 (InGaAs) diode across the entire temperature range. The results suggest the InGaAlAs-InGaAs detector may offer some improvement over Si-InGaAs combination when measuring temperature below 500 °C.

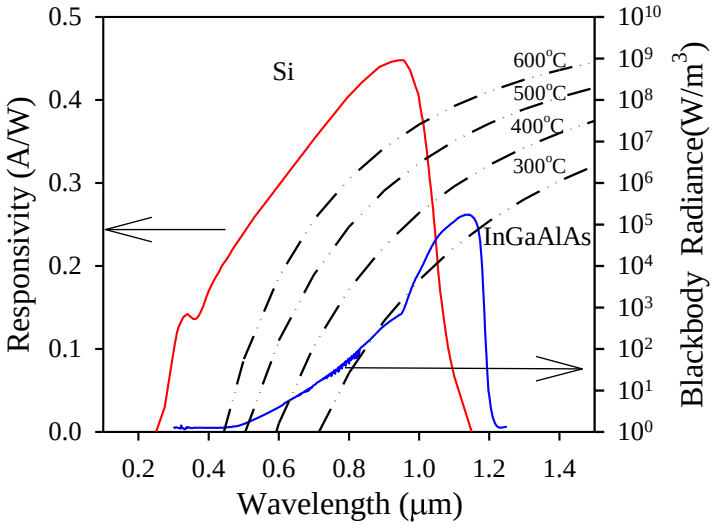

Figure 4.6 Si and InGaAlAs spectral responses and spectral radiance of a blackbody at temperatures from 300 to 600 °C

The photocurrent from a photodetector can be calculated by integrating the product of the incident optical power with the spectral response of the photodetector. Figure 4.6 shows the emitted energy from a blackbody source versus wavelength calculated from Planck's law [15], as well as the Si and the InGaAlAs spectral responses. Although the responsivity of InGaAlAs is lower than Si at shorter wavelengths, its higher response at

wavelengths above 1100 nm leads to a larger overlap between the diode spectral response and the blackbody radiated spectrum. This larger overlap compensates for the lower response in the shorter wavelength region. Consequently, the InGaAlAs diode produces a slightly higher signal when the radiated power is mostly in the longer IR wavelengths, when the T_{BB} is below 500 °C. On the other hand as the temperature increases, the peak radiated wavelength from the blackbody shifts to a shorter wavelength. Hence the Si diode, with higher responsivities at shorter wavelengths, higher quantum efficiency and longer depletion width produces stronger signal at T_{BB} > 500 °C, as shown in Figure 4.5(a).

The depletion width in the InGaAlAs is 2.41 μm, compared to 10.16 μm in K1713-09(Si). This significantly thinner InGaAlAs is clearly more suitable for development into high density array than the thick Si. Furthermore the responsivity of the InGaAlAs can be increased by optimising the absorption layer (for instance using thinner p InGaAlAs layer to increase carrier collection efficiency) and inclusion of a broadband anti-reflection coating. The InGaAs diode in this work also produces higher photocurrent due to a slightly larger area and a longer detection wavelength than the K1713-09(InGaAs) diode.

From Figure 4.5(b), it can be seen that the *SNR* values are similar for both sets of diode despite diodes having much higher dark current than their commercial counterparts. This is attributed to the dominance of the amplifier noise over the shot noise from the diode when the photocurrent is low. Using a spectrum analyser the amplifier noise of was found to be 125 $nV/Hz^{1/2}$, relatively high compared to state-of-the-art amplifiers. It is also higher than the noise induced by a dark current of 200 pA (equivalent to 8$nV/ Hz^{1/2}$ at the amplifier output) in the InGaAs diode in this work. The *SNR* increases quickly as the T_{BB} increases for both tandem diodes. However, the *SNR*s increase much more gradually at T_{BB} above 250 °C and 450 °C for long and short wavelength diodes respectively. These results are consistent with that from Hobbs *et al*. [16]. At low T_{BB} the amplifier noise is the dominant noise component in the system; *SNR* increases as output signal increases rapidly with increased temperature. As the T_{BB} increases to a sufficiently high value, the shot noise induced by the high photocurrent from diode becomes the overwhelming noise source, leading to the observed trend.

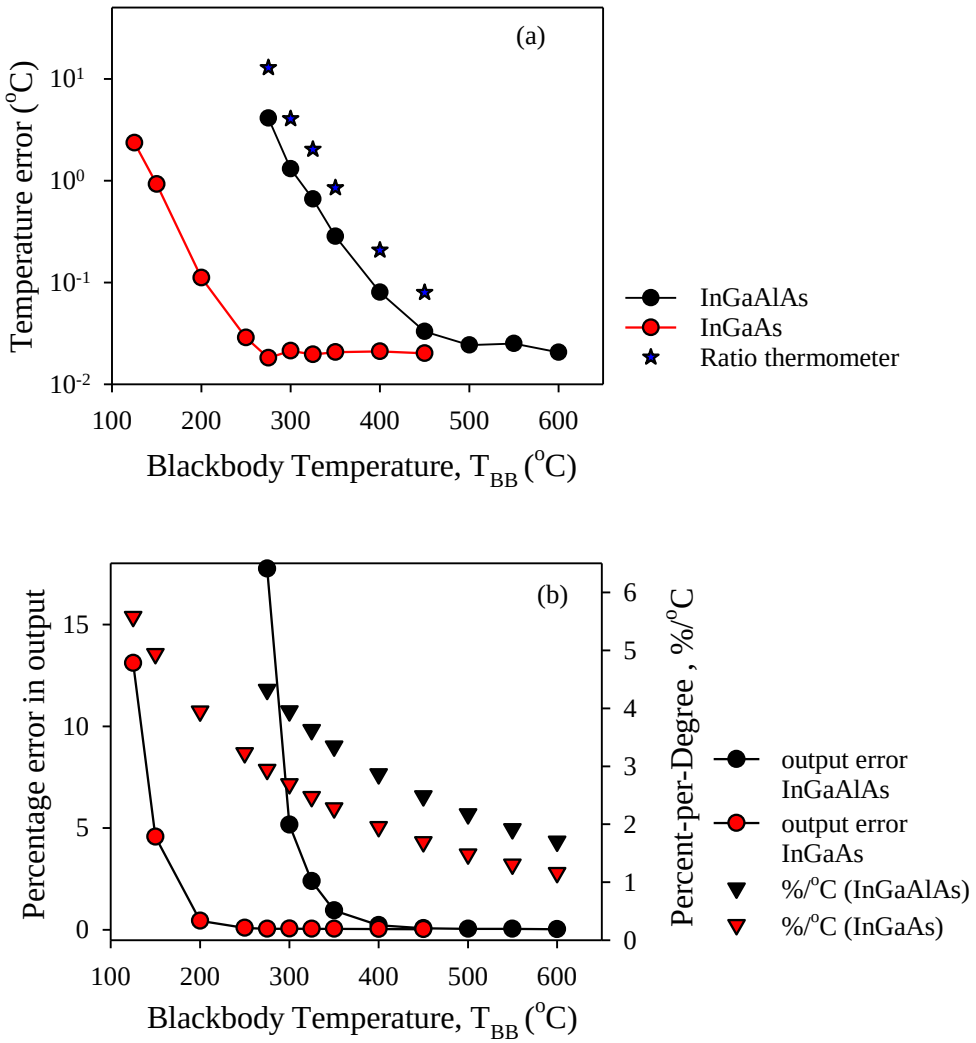

Figure 4.7 (a) Temperature error, including electronic noise and laboratory ambience, of the individual diode and when combined as a ratio thermometer and (b) percentage error in output and %/°C at different T_{BB}

Corresponding to the detector-amplifier noise, the temperature error was calculated using the method outlined in section 3.6.1. Figure 4.7(a) shows the temperature error for the InGaAs and InGaAlAs diodes and as a ratio thermometer. The temperature error ranges from 2.3 to 0.02 °C for InGaAs diode and 4 to 0.02 °C for the InGaAlAs diode. Assuming the acceptable temperature error is 2 °C [17], the InGaAlAs can be used to measure a T_{BB} = 294 °C while the InGaAs diode can measure T_{BB} = 131 °C. As a ratio thermometer, this temperature error becomes higher due to longer effective wavelength than single waveband thermometer. This InGaAlAs-InGaAs two-colour thermometer shows an error of 12.8 °C at T_{BB} = 275 °C. The error drops with increase of temperature to a value of

0.1 °C at T_{BB} = 450 °C. From the results InGaAlAs-InGaAs can be used as a ratio thermometer to detect down to 325 °C with an error of 2 °C. It is well known that the error of a ratio thermometer is larger than a single wavelength thermometer [18], as illustrated in section 2.2.3. Despite this, the importance of a ratio thermometer in overcoming the measurement errors, due to uncertainties in emissivity and attenuation in the signal path, is well recognized since there is a vast array of manufacturing applications where only measurements of greater than 600 ^{o}C are required. When an application dictates that lower temperature measurements are needed, it is possible to achieve this by moving both measurements to longer wavelengths. From Figure 4.7(a) it is clear that the temperature error reduces as T_{BB} increases. However, it tends to a saturation value of 0.02 °C at temperatures above 250 °C and 450 °C for InGaAs and InGaAlAs respectively. This is due to the progressively smaller change of percentage error in output signals as temperature increases, which is illustrated in Figure 4.7(b).

It is also worth noting that the test system might contribute some measurement error for the device performance evaluation. To investigate this, the photocurrent scanning was performed on a commercial InGaAs with diameter of 250 μm by using a motor scan system with a scanning step of 10 μm. The output voltage distribution and 2D contour are shown in Figure 4.8. It is clear that the incident power onto the detector has a near-Gaussian distribution with a diameter of 2.4 mm spot size. Therefore, the commercial Si can almost absorb all the incident power whilst the InGaAlAs loses a fraction of power. A small aperture in a real thermometer is always employed in front of the detector. By employing an aperture and good shielding in the set-up further improvement can be achieved in future work. With further improvement to increase the responsivity of the InGaAlAs to amplify signal, and lower amplifier noise to reduce total system noise, potentially more sensitive ratio thermometer can be obtained from this material system.

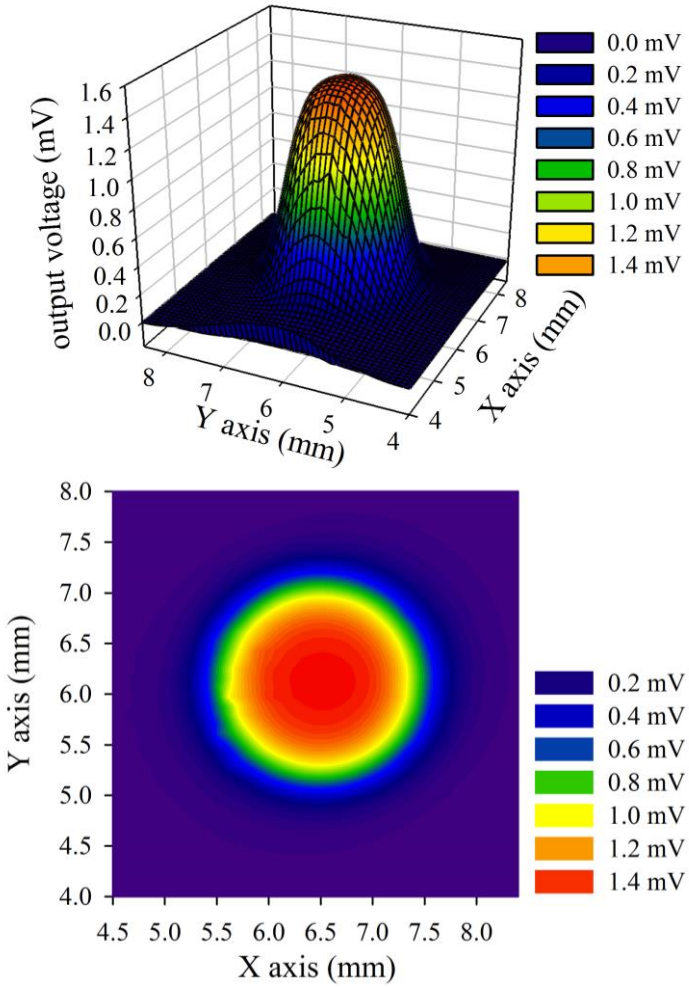

Figure 4.8 Output voltage distribution base on a commercial InGaAs (top) and 2D contour of output voltage (bottom)

4.6 Conclusion

In conclusion, the first evaluation of an InGaAlAs-InGaAs two-colour photodetector for use in radiation thermometry was performed. Although the dark currents are higher in this two-colour detector, the *SNR*s measured are comparable to the commercial diodes, since the noise is largely dominated by the amplifier when the photocurrent is low. *SNR* above 10 was achieved at the lowest measured temperatures of T_{BB} = 125 °C and T_{BB} = 275 °C for long and short band detector, respectively. When evaluated as a ratio thermometer, the InGaAlAs-InGaAs two-colour photodetector shows a temperature error of 12.8 °C at T_{BB} = 275 °C, but improves with temperature to 0.1 °C at T_{BB} = 450 °C. The lowest temperature that this two colour detector can measure accurately is 325 °C

with an error of 2 °C. This is significantly lower than 400 °C typically achieved using a commercial Si-InGaAs detector.

References

[1] J. Dixon, "Radiation thermometry," *J. Phys. E: Sci. Instrum.*, vol. 21, no. 5, pp. 425-436, May 1988.

[2] J. Mishin, M. Vardelle, J. Lesinski and P. Fauchais, "Two-color pyrometer for the statistical measurement of the surface temperature of particles under thermal plasma conditions," *J. Phys. E: Sci. Instrum.*, vol. 20, no. 6, pp. 620-625, Jun. 1987.

[3] J. Novak and P. Elias, "A silicon-InGaAs tandem photophotodetector for radiation thermometry," *Meas. Sci. Technol.*, vol. 6, no. 10, pp. 1547-1549, Jun. 1995.

[4] G. R. Peacock, "Ratio radiation thermometry thermometers in hot rolling and galvannealing of steel strip," *in Proc. AIP*, vol. 684, no. 1, pp. 789-794, Sep. 2003.

[5] R. A. Harding and M. Wickins, "Temperature measurements during induction skull melting of titanium aluminide," *Materials Sci. and Technol.*, vol. 19, no. 9, pp. 1235-1246, Sep. 2003.

[6] J. Yamada, T. Murase and Y. Kurosaki, "Thermal imaging system applying two-color thermometry," *Heat Transfer—Asian Research*, vol. 32, no. 6, pp. 473-488, Sep. 2003.

[7] K. P. Möllmann, F. Pinno, M. Vollmer and B. U. o. A. Sciences, "Two-color or ratio thermal imaging-potentials and limits," FLIR Systems, Inc, 18 May 2011. [Online].

[8] M. Vollmer and K. P. Möllmann, "Advanced methods in IR Imaging," in *Infrared Thermal Imaging: Fundamentals, Research and Applications*, Weinheim, Germany, WILEY-VCH Verlag GmbH & Co.KGaA, 2011, pp. 164-166.

[9] D. D. Burleigh, K. E. Cramer and G. R. Peacock, "Furnace wall-tube monitoring with a dual-band portable imaging radiometer," *Proc. SPIE* , vol. 5405, pp. 221-226, Apr. 2004.

[10] B. K. Tsai, D. P. DeWitt and G. J. Dail, "Application of dual-wavelength radiation thermometry to the aluminum industry," *Elsevier*, vol. 11, no. 3, pp. 211-221, Jun. 1993.

[11] N. A. Papanicolaou, G. W. Anderson, A. A. Lliadis and A. Christou, "Lattice mismatched InGaAs on silicon photodetectors grown by molecular beam epitaxy," *J. Electro. Mater.* , vol. 22, no. 2, pp. 201-206, Feb. 1993.

[12] P. Bhattacharya, "Structural properties of InGaAs," in *Properties of lattice-matched and strained Indium Gallium Arsenide*, London, UK, INSPEC, 1993, pp. 20-21.

[13] "Two-Color Photodetector K1713-05/-08/-09," Hamamatsu Photonics K. K., Hamamatsu, Japan., May 2006. [Online]. Available: http://www.hamamatsu.com/resources/pdf/ssd/k1713-05_etc_kird1040e03.pdf. [Accessed 22 Sep. 2014].

[14] D. P. Blair and P. H. Sydenham, "Phase sensitive detection as a means to recover signals buried in noise," *J. Phys. E: Sci. Instrum.*, vol. 8, no. 8, pp. 621-627, Aug. 1975.

[15] S. D. Gunapala and S. V. Bandara, "Quantum well infrared photodetector (QWIP) focal plane arrays," in *Intersubband Transitions in Quantum Wells: Physics and Device Applications I*, Academic Press, 2000, pp. 197-291.

[16] M. J. Hobbs, C. H. Tan and J. R. Willmott, "Evaluation of phase sensitive detection method and Si avalanche photodiode for radiation thermometry," *JINST*, vol. 8, no. 3, p. P03016, Mar. 2013.

[17] G. Machin and B. Chu, "High-quality blackbody sources for infrared thermometry and thermography between -40 ºC and 1000 ºC," *Imaging Sci.*, vol. 48, pp. 15-22, 2000.

[18] T. J. Quinn, "Radiation thermometry," in *Temperature*, London, UK, Academic Press, 1990, pp. 332-431.

Chapter 5 InAs photodiodes for 3.43 μm radiation thermometers and low temperature measurement

5.1 Introduction

Radiation thermometers are used to monitor the temperature of an object without physical contact. The object's temperature is calculated by measuring the emitted energy from the object over a specific wavelength range to determine its blackbody temperature [1]. These non-contact instruments are widely used in temperature measurement of plastics [2], glass [3] and metals [4]. Depending on their detection method, detectors for radiation thermometers can be classed into one of two categories, thermal detectors and photon detectors. Thermal detectors include thermopiles, pyroelectric detectors and bolometers, which can respond to radiation over a broad spectrum and hence can detect down to low temperatures [5]. These thermal detectors produce physical parameter changes that are proportional to the temperature changes of a target. Appropriate selection of an absorbent coating enables these detectors to work as either a broad band or a narrow band thermometer. However, when used as uncooled detectors, they suffer from long response time and low sensitivity. In comparison, photon detectors offer much higher sensitivity and shorter response times. They detect over a narrower wavelength range and can only measure a limited temperature range [4]. Therefore semiconductors with different band gaps are normally employed to cover different temperature ranges.

In practical measurements, the emissivity factor compares the spectral radiance from an object to that of a blackbody at the same temperature. Therefore uncertainty in the emissivity can lead to significant error in radiation thermometry. Fortunately at shorter wavelengths the rate of change in the spectral radiance as a function of temperature increases more rapidly, leading to a smaller temperature error [6]. In addition to the smaller error, from semiconductor physics it is well known that the short wavelength detectors have lower leakage current and hence lower shot noise. Si and $In_{0.47}Ga_{0.53}As$ (hereafter referred to as standard InGaAs) photodiodes have been widely used as high

temperature sensors in radiation thermometry [5,7]. Due to the non-linear spectral power of Planck's law, these detectors' cut-off wavelengths of 1.0 and 1.6 μm respectively limit the minimum temperature that can be measured to 400 and 150 ^{o}C respectively. As the target temperature decreases, the peak in spectral radiance shifts to longer wavelengths, necessitating the use of narrow band gap semiconductors that are sensitive to longer wavelengths. For example by increasing the Indium (In) composition, extended InGaAs photodiodes detecting up to 2.6 μm are available commercially. The extended InGaAs photodiode enables commercial thermometers to detect temperatures down to 50 ^{o}C [8]. Eppeldauer and Yoon [9] recently used an extended InGaAs photodiode, with a cut-off wavelength of 2.5 μm and cooled to - 85 ^{o}C, to measure a temperature of 36 ^{o}C with a temperature error of ~ 0.01 ^{o}C. Lead salt alloys, such as PbS and PbSe photoconductors with central operation wavelength at 2.0 and 4.0 μm, respectively, have been widely used as commercial room temperature thermometers to detect objects close to ambient temperature [10]. These uncooled photon detectors used are summarised in Table 5.1.

Table 5.1 Uncooled photon detectors used in radiation thermometers

Detectors	operation wavelength	Temperature range
Si	1.0 μm	400 - 2000 ^{o}C [5]
Standard InGaAs	1.6 μm	150 - 1000 ^{o}C [8]
Extended InGaAs	2.3 μm	50 - 400 ^{o}C [9]
PbS	2.0 μm	80 - 800 ^{o}C [11]
PbSe	4.0 μm	30 - 200 ^{o}C [11]

For measuring temperature of gases, glasses and certain plastics, a narrow band spectral filter is employed in the system in a relevant absorption band [11]. For instance, narrow band thermometers operating at 3.4 μm are widely used in the processing of thin film plastics [12,13], which have C-H bonds that resonate at this wavelength. Amongst the photon detectors reviewed above, those that are sensitive to light at this wavelength unfortunately do not provide fast measurements. InAs photodiodes have recently been

demonstrated as a promising material for IR sensing [14]. With a band gap of 0.36 eV, InAs photodiodes exhibit a cut-off wavelength of 3.55 μm at room temperature, providing a high detectivity around 3.4 μm. Therefore, InAs photodiodes have potential for use in an uncooled thermometer or thermal imager working at 3.0-3.65 μm. Recently Hobbs *et al.* [15] demonstrated that an avalanche photodiode can provide significant signal to noise ratio improvement in radiation thermometry. InAs has also been demonstrated as an excellent avalanche photodiode that operates with single carrier multiplication to produce negligible excess noise, presenting a huge potential further improvement for IR imaging [16 ,17]. Moreover, Sandall *et al.* have reported linear arrays of 1×128 InAs avalanche photodiodes [18]. Therefore future IR radiation thermometers could potentially be enhanced using discrete and arrays of InAs photodiodes or avalanche photodiodes. In this chapter, detailed characterisation of InAs photodiode and evaluated its potential for radiation thermometry are presented.

5.2 Device structure and fabrication details

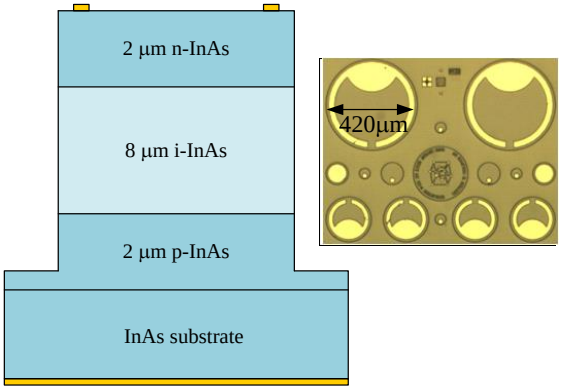

Figure 5.1 The schematic structure and top view image of fabricated device of various sizes

The InAs wafer studied in this work was grown by Molecular Organic Chemical Vapour Deposition (MOCVD). The structure was grown on 2" p-type InAs substrates. The structure comprised of a 2 μm p+ layer (1×10^{18} cm^{-3}) followed by an intrinsic region thicknesses of 8 μm and then a 2 μm n+ layer (1×10^{18} cm^{-3}), as shown in Figure 5.1. Ti/Au metal with thickness of 20/200 nm was deposited to form top and bottom ohmic contacts. The sample was fabricated using wet chemical etchants [19] of 1:1:1

(phosphoric acid: hydrogen peroxide: deionized water) etch, followed by a finishing etch of 1:8:80 (sulphuric acid: hydrogen peroxide: de-ionized water), to define the mesa diodes with diameters of 420, 220, 120 and 70 μm in Figure 5.1. No anti-reflection coating was performed on these devices.

5.3 *I-V* and *C-V* measurement

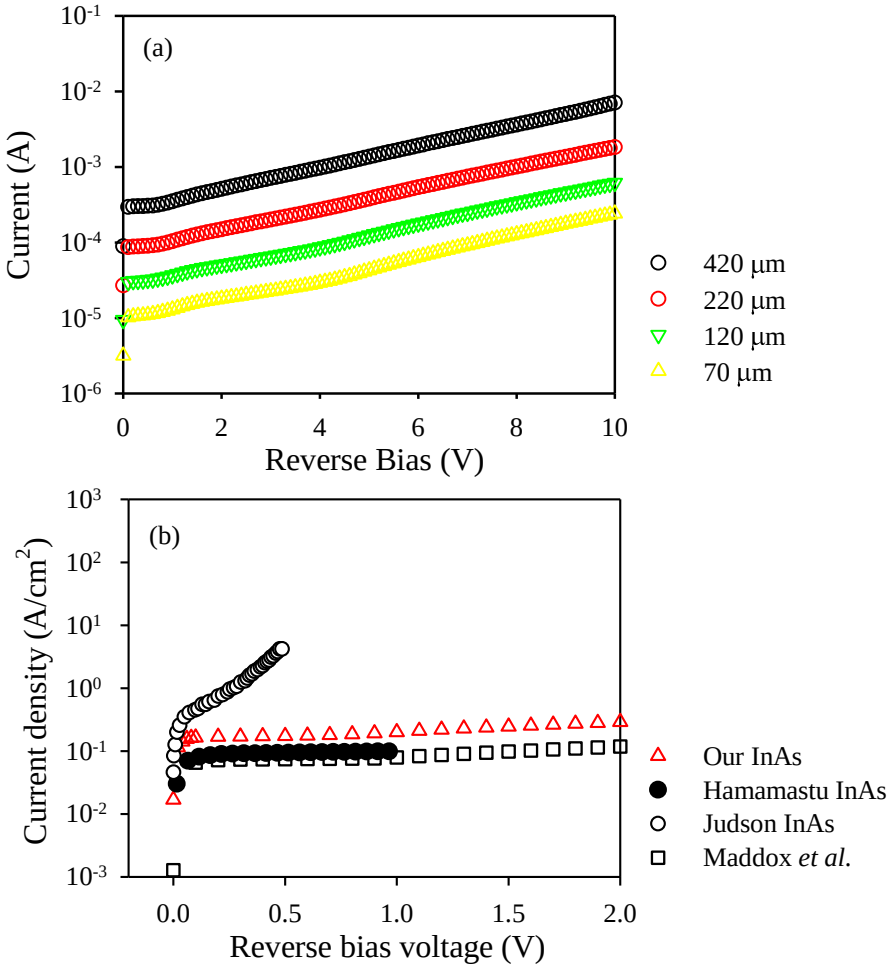

Figure 5.2 (a) Room temperature dark current of InAs photodiodes with different diameters and (b) dark current density comparison with commercial InAs and reported data

I-V measurements were performed using a Keithley 236 source-measurement unit. Devices with different diameters show bulk dominated dark currents at room temperature. For clarity, only current density from a device with 420 μm is shown in Figure 5.2(b). Commercial InAs diodes and that reported by Maddox *et al*. [20] were also

compared with InAs diode in this work. The diode in this work shows slightly higher dark current density than that from a commercial Hamamatsu InAs [21] but lower than that from Judson InAs [22]. It is worth noting that despite the large amount of exposed sidewall in the InAs mesa diode in this work, its dark current density remains competitive. Improved growth should produce InAs with lower dark current as demonstrated by Maddox *et al*. [20] who adopted similar etching recipe as ours.

C-V measurements were also performed on these devices to study the material background doping. Figure 5.3 shows the capacitances and depletion width of InAs with different sizes as a function of reverse bias. *C-V* results suggest this wafer is not fully depleted at zero bias and has a high unintentional doping level.

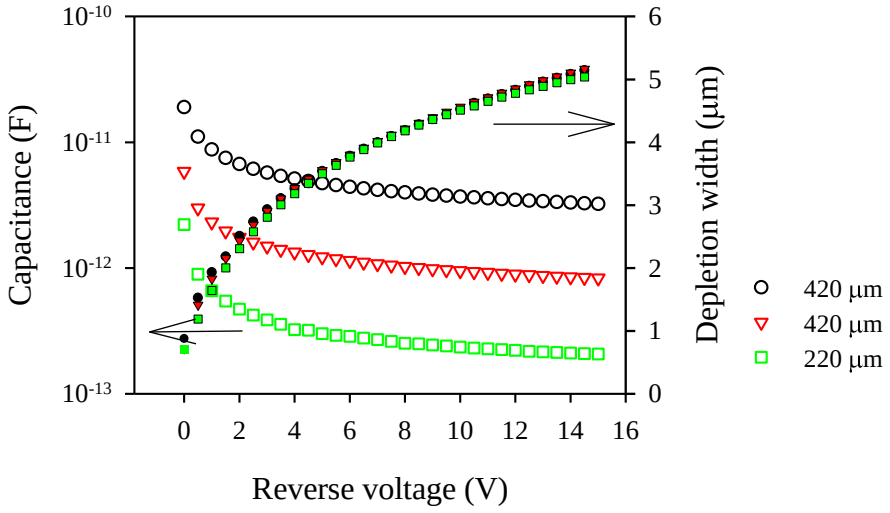

Figure 5.3 Capacitance and depletion width of InAs photodiodes with different diameters at 77 K

5.4 Responsivity and detectivity

Responsivity on InAs was performed in this work. Figure 5.4(a) shows the room temperature responsivity comparison of InAs photodiodes in this work and commercial InAs detectors. The responsivity was deduced using normalised spectral response obtained from the FTIR and the peak responsivity measured using a T_{BB} = 800 ºC. Responsivity values at wavelengths of 633, 1520 and 2004 nm were cross-checked using CW lasers at the respective wavelengths. With zero bias, the InAs diode shows a peak responsivity of 1.28 A/W at 3.35 μm and a cut-off wavelength (at 50% of peak response)

of 3.55 μm, giving ~ 48% external quantum efficiency (EQE) across the whole spectrum down to 633 nm. However, this external quantum efficiency can be improved up to 54% with a bias of 0.1 V as shown in Figure 5.4(b), which is higher than that of Hamamatsu InAs diode and only slightly lower than Judson diode at longer wavelengths. Deposition of an anti-reflection coating should increase the responsivity on InAs devices.

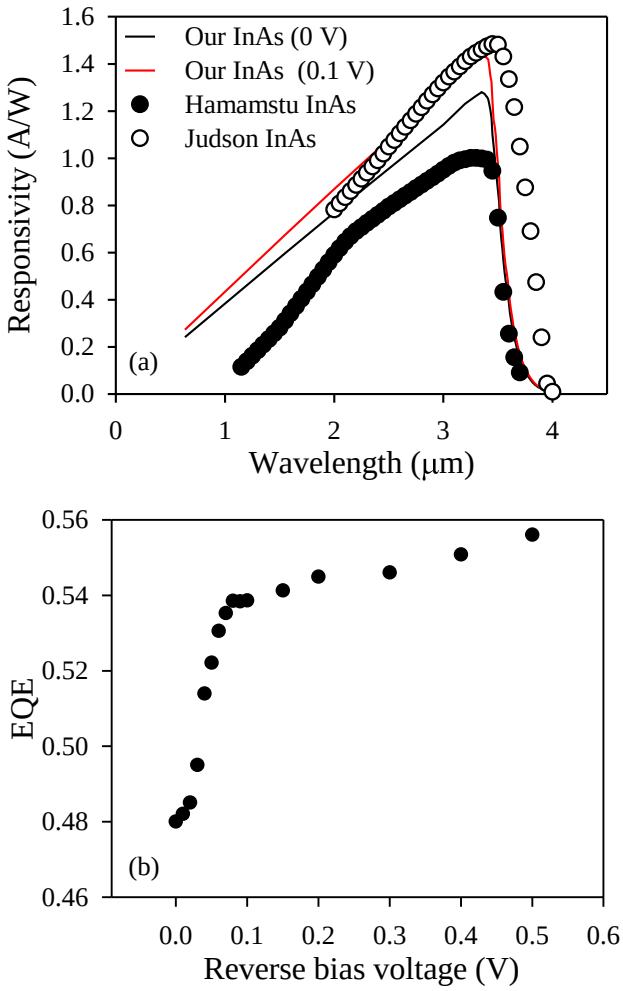

Figure 5.4 (a) Responsivity versus wavelength characteristics of InAs photodiode in this work and commercial InAs photodiodes at room temperature, and (b) External quantum efficiency, at the wavelength of 2004 nm as a function of reverse bias, of InAs photodiode with a diameter of 420 μm.

To investigate the reason for the increase of quantum efficiency with bias, the depletion width and doping profile were extracted from above *C-V* results. From Figure 5.3, the measurements suggest the diode has a depletion width of 0.95 μm only at 0 V, owing to an unintentional background doping of 6×10^{14} cm^{-3} in the i-InAs layer. At a reverse bias

of 0.1 V, the depletion width increases to 1.15 μm, improving the responsivity. However increasing the bias also increases the dark current, as shown in Figure 5.2.

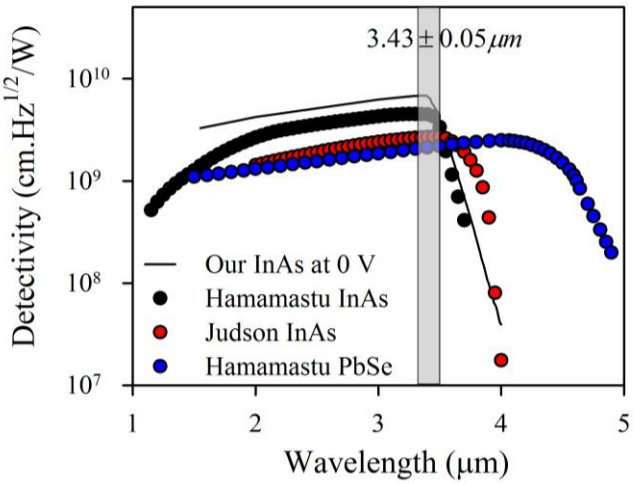

Figure 5.5 Detectivity of the InAs photodiodes in this work and commercial InAs and PbSe detectors at room temperature

The detectivity can be calculated from responsivity and dark current according to the equation (2.27). Figure 5.5 shows the room temperature detectivity comparison between the InAs photodiodes in this work and commercial InAs and PbSe detectors. The diode shows a cut-off wavelength of 3.55 μm (taken as 50% of peak response). The InAs photodiode has higher peak detectivity than both Judson and Hamamatsu InAs diodes. Compared with PbSe, InAs in this work still shows higher detectivity across the entire spectral range. The diode detectivity can be further improved by optimising the absorption efficiency (using antireflection coating and reducing the background doping in the absorption region) and by reducing the dark current (using wide band gap window layers).

5.5 Linearity and photocurrent uniformity

To evaluate the detector performance, the linearity test was also performed on InAs diodes with a diameter of 420 μm. By using the photocurrent measurement setup in Figure 3.3, the photocurrent in 2004 nm and 1550 nm as a function of incident power is shown in Figure 5.6. The InAs detector shows very good linearity in the incident power range of 2 nW - 200 μW for both wavelengths at room temperature.

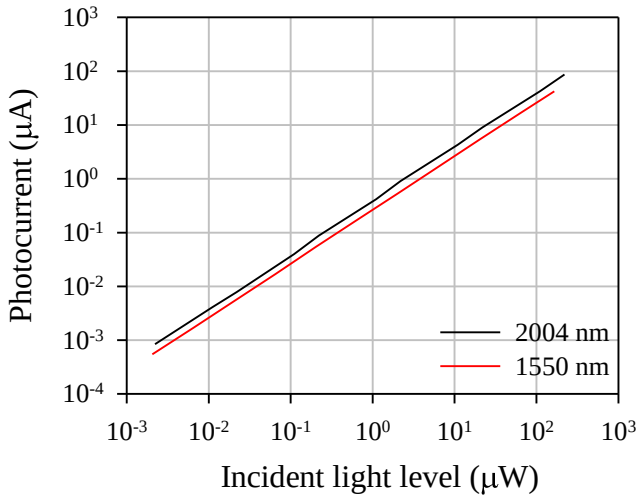

Figure 5.6 Photocurrent linearity of InAs photodiodes at 1550 and 2004 nm at 0 V

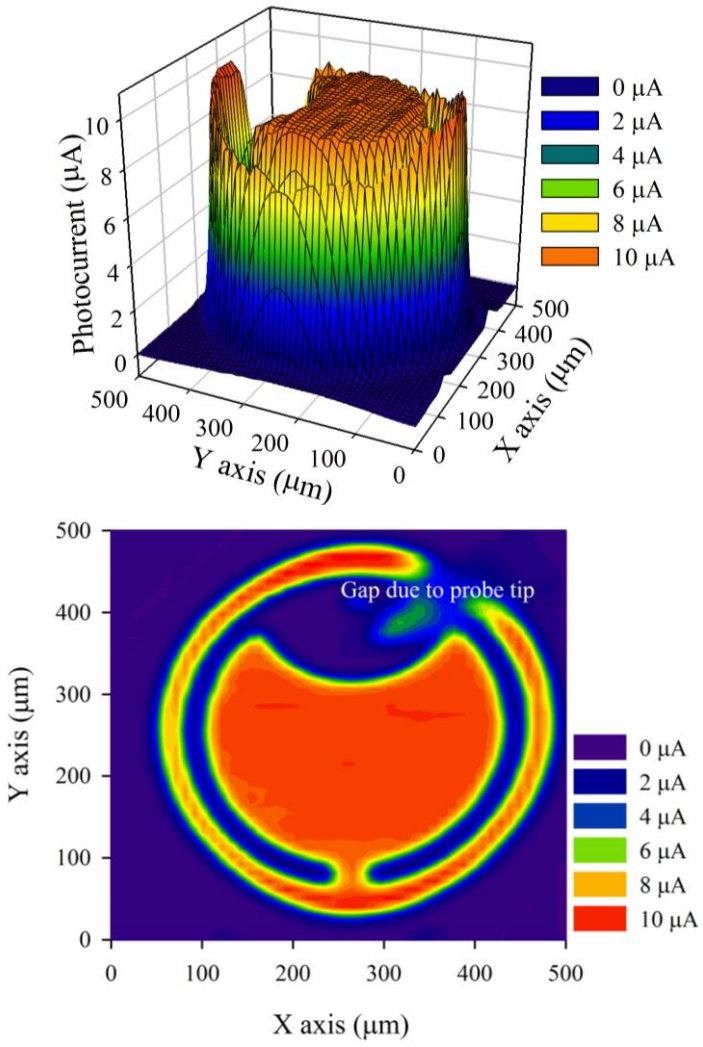

Figure 5.7 3D mesh plot of photocurrent distribution (top) at 1520 nm from InAs device at 0 V and 2D contour plot (bottom)

To assess the responsivity uniformity across the diode, a photocurrent scan was performed. Figure 5.7 shows a 3D photocurrent distribution and 2D contour plot of the InAs photodiode, measured using light from a CW 1520 nm He-Ne laser. It clearly shows high uniformity of responsivity within the centre optical windows of InAs diode.

5.6 Thermometry measurement at room temperature

Temperature measurement was performed using the setup in Figure 3.9. An aperture size of 7.5 mm was used in this measurement. As the bias increases from 0 to 0.1 V, the device dark current increases by 10 times while the peak responsivity only improves by 13%. Therefore, radiation thermometry measurements were performed at 0 V on the InAs to minimise the influence of the device dark current. A commercial P9696-03 PbSe photoconductor [23] biased at 15 V was measured to compare with InAs diode for radiation thermometry. Figure 5.8 shows the mean output photocurrent and signal to noise ratio (*SNR*) as a function of T_{BB} on both detectors. This *SNR* is defined as the ratio of mean photocurrent to the standard deviation of the output photocurrent. Each mean photocurrent value was calculated from 6 sets of data points, with each set taken over duration of 120 s using a sampling time of 0.05 s. This measurement duration was chosen so that fluctuation or drift in the photocurrent could be recorded. The InAs diode produces higher photocurrent across the temperature range. Output photocurrent and *SNR* increases with increasing T_{BB}. The rate of increase in the photocurrent becomes smaller as the T_{BB} increases due to non-linear increase in the photon flux with temperature, as described by Planck's Law. Although the InAs shows shorter cut-off wavelength, it demonstrates much higher photocurrent than PbSe due to higher responsivity. At low photocurrent values, the noise is dominated by shot noise induced by the diode's dark current and the amplifier's noise. Hence as the photocurrent increases with the T_{BB} the *SNR* also increases. However, at high photocurrent, shot noise induced by the photocurrent becomes more dominant. This, coupled with the smaller increase in the photocurrent, leads to a smaller rate of increase in the *SNR* at high T_{BB}. However, for PbSe photoconductor, the lower output photocurrent results in small steady state in *SNR* at high T_{BB}.

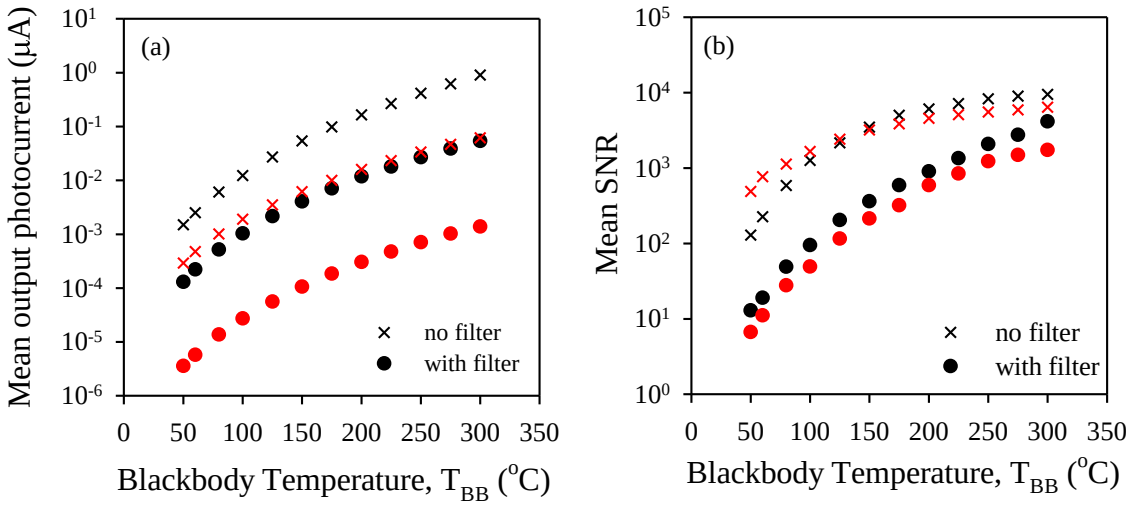

Figure 5.8 (a) Mean Photocurrent and (b) *SNR* of the InAs photodiodes at 0 V (black symbols) and PbSe photoconductor at 15 V (red symbols) measured with and without filter.

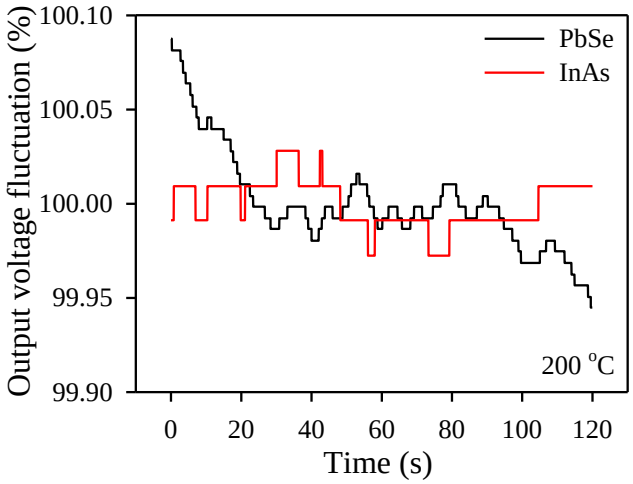

Figure 5.9 Output photocurrent fluctuations of InAs and PbSe at a T_{BB} = 200 °C

Figure 5.9 shows the output photocurrent fluctuation of both detector at a T_{BB} = 200 °C (200 °C was chosen because it is close to temperature in plastic manufacturing). It can be seen that PbSe suffers from more severe drift problem than InAs. Since InAs produces higher output photocurrent and more stable output, it is a better candidate for radiation thermometer operating at wavelengths above the detection range of InGaAs photodiodes (up to 2.6 μm).

To assess the potential of the InAs for applications at 3.43 μm, the radiation thermometry measurements as described above were repeated with a 3.43 μm narrow band filter and the data are included in Figure 5.8. The output signal increases with the T_{BB} as expected. Compared to data obtained without the narrow band filter, the output photocurrent was reduced significantly. This significant reduction is due to incomplete transmittance (76%) and 62 nm bandwidth of the filter, which blocks most of the energy from higher wavelength. As much higher photocurrent from InAs, it shows higher *SNR* than PbSe across all the measured temperature range.

Figure 5.10 shows the temperature error of InAs photodiodes and PbSe photoconductor as a function of T_{BB}. As the *SNR* increases, the temperature error reduces with increasing T_{BB}. Without the filter, InAs only shows better performance than PbSe at T_{BB} above 150 ^{o}C. At lower temperatures, energy from longer wavelengths beyond InAs spectrum can be detected by PbSe to produce a better temperature resolution. For the InAs diode the temperature error reduces from 0.17 ^{o}C at T_{BB} = 50 ^{o}C to 0.007 ^{o}C at T_{BB} = 300 ^{o}C. When the filter is included, InAs shows better performance than PbSe across the temperature range measured. The reduced signal increases the temperature errors to 1.88 and 0.018 ^{o}C at temperatures of T_{BB} = 50 ^{o}C and T_{BB} = 300 ^{o}C, respectively.

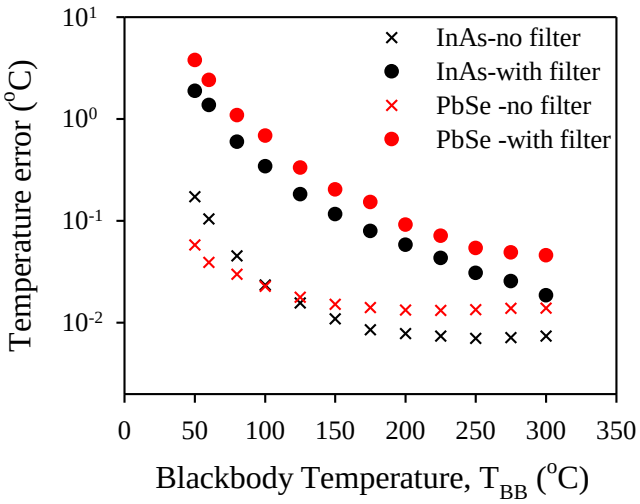

Figure 5.10 Temperature error of the InAs photodiode (black symbols) and PbSe photoconductor (red symbols) as a function of T_{BB} at 0 V with or without narrow band filter

The results clearly demonstrated the potential of using InAs photodiodes for sensing temperature close to ambient temperature. If the acceptable temperature error is set at ±2 ^{o}C (as used in thermal imagers [24]), the detectors can accurately detect target temperature of 50 ^{o}C and higher. Measured IR signals with narrow band filter in Figure 5.8 also confirm that the InAs is ideally suited for applications requiring 3.43 μm operating wavelength. Bi-axially oriented film extrusion and extrusion coating in plastics industry often works at high temperatures above 200 ^{o}C [13] where the InAs thermometers can offer temperature error less than 0.05 ^{o}C, confirming the potential of using InAs for a 3.43 μm radiation thermometer.

5.7 Temperature measurement using minimally cooled detector

To obtain more accurate thermometer, the detectors were cooled. Figure 5.11 shows the temperature dependence of dark current of InAs photodiodes with a diameter of 420 μm. The reverse dark current reduces ~ 3 orders of magnitude from 295 to 200 K which is similar to the trend in the work by Ker *et al*. [25].

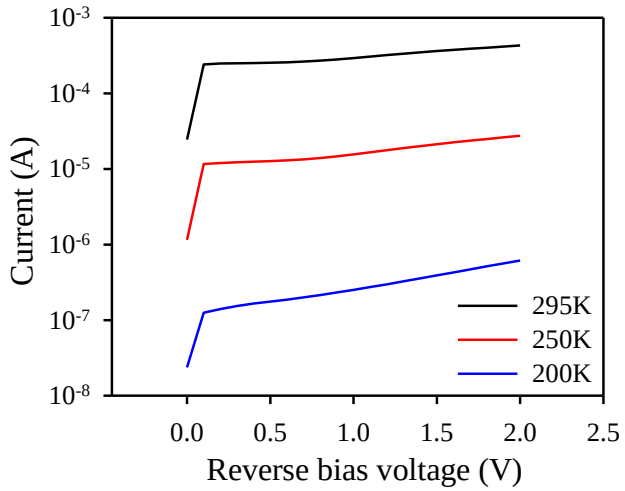

Figure 5.11 Temperature dependence of dark current of the InAs photodiodes

The temperature dependence of thermometry measurement was done using cooling system in the setup in Figure 3.8. A LANDCAL P80P blackbody source was set at temperatures between 37 and 80 ^{o}C with the detector temperature set to 295 and 200 K in these measurements. Figure 5.12 shows the mean photocurrent and *SNR* of the InAs photodiodes at 0 V. As T_{BB} increases, the photocurrent and *SNR* increases. As the

detector temperature reduces from 295 to 200 K, the output photocurrent is reduced by around 50% at all T_{BB} range. This is due to the cut-off wavelength shifting to lower wavelengths when the detector was cooled to lower temperature. The normalised InAs spectrum at diode temperatures of 295 to 77 K is shown in Figure 5.13. From Planck's curve of radiated energy from blackbody, the majority of radiated photons are at longer wavelengths which results in lower photocurrent at low detector temperature.

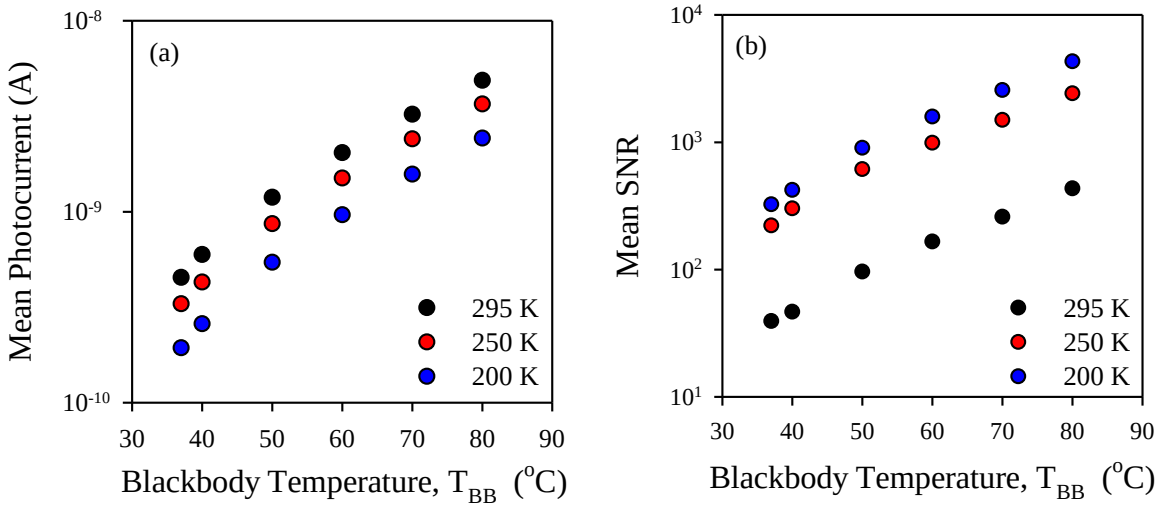

Figure 5.12 (a) Mean Photocurrent and (b) *SNR* of the InAs photodiodes at different detector temperatures at 0 V

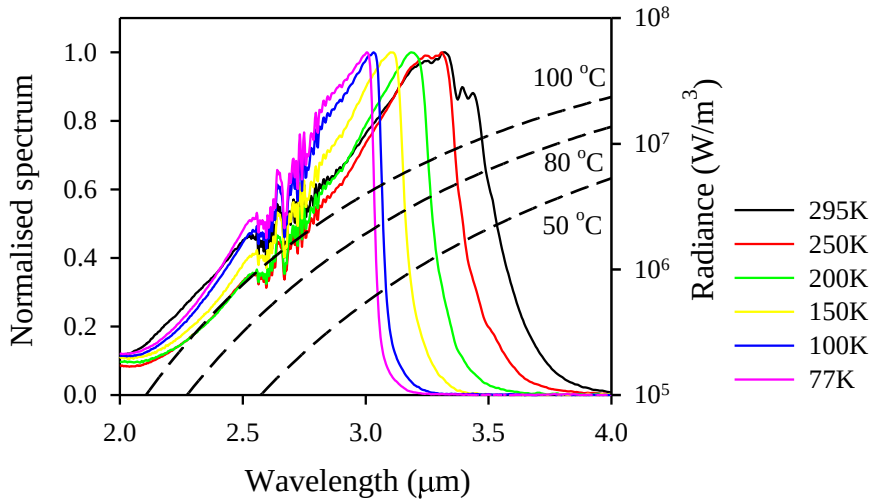

Figure 5.13 Normalised spectrums of the InAs photodiodes from FTIR at different detector temperatures from 295 to 77 K and blackbody radiance at T_{BB} = 50, 80 and 100 °C

Despite the drop in photocurrent, the *SNR* increases with decreasing detector temperature. This is because as the temperature is reduced the dark current drops much more rapidly than the photocurrent as illustrated in Figure 5.11. For instance, the photocurrent drops only 1/3 at 250 K compared to that from room temperature while the dark current drops by more than 20 times. However, the *SNR* increases much slower as the temperature reduces from 250 to 200 K. Following the *SNR* trend, the temperature error of InAs photodiodes in Figure 5.14 reduces slowly from 250 to 200 K. It is of particular interest to note that the device dark current reduces by 1000 times when the diode is cooled from room temperature to 200 K. The temperature error improves by 10 times from 0.46 to 0.048 ^{o}C at a T_{BB} = 37 ^{o}C, confirming the potential of using InAs for low temperature sensing, including human temperature sensing. As discussed in chapter 4, the amplifier noise is around 125 nV/Hz$^{1/2}$ which gives an equivalent noise current level of ~50 nA. As detector temperature reduces, the noise from dark current reduces such that the amplifier noise becomes dominant at 200 K. Therefore, a lower noise amplifier will allow the InAs photodiodes to be used for performing more accurate at lower temperature. An alternative approach is to use a smaller device to reduce the detector dark current. For instance halving the detector diameter will reduce the dark current by 4 times so that the dark current reduces to ~5 nA at 200 K. Provided that the optical coupling can be maintained, it should be possible to operate in the avalanche mode which will provided a higher *SNR* in future work.

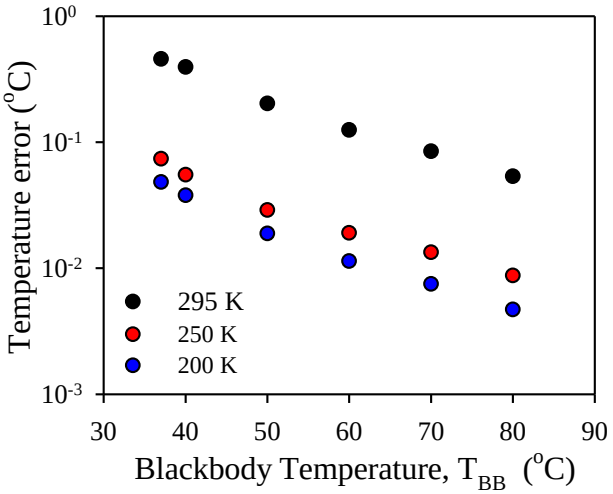

Figure 5.14 Temperature errors of the InAs photodiodes at different detector temperatures at 0 V

5.8 Conclusion

In conclusion, the electrical and optical performance of InAs photodiodes have been characterised. They show bulk dark current mechanism and high detectivity at room temperature.

The performance of InAs photodiodes for use in radiation thermometry was also evaluated. The lower temperature limit from the uncooled InAs photodiode is 50 ^{o}C with a temperature error of 0.17 ^{o}C. Using a narrow band filter, it was also demonstrated that the signal at the wavelength of 3.43 μm is sufficiently strong to perform accurate temperature measurements. Cooling the diode to 200 K enables InAs to accurate detect low temperatures down to 37 ^{o}C, demonstrating the huge potential for radiation thermometry and human body temperature sensing.

References

[1] J. Dixon, "Radiation thermometry," *J. Phys. E: Sci. Instrum.*, vol. 21, no. 5, pp. 425-436, May 1988.

[2] K. Esser, E. Haberstroh, U. Husgen and D. Weinand, "Infrared radiation in the processing of plastics: Precise adjustment-the key to productivity," *Advances in Polymer Technology*, vol. 7, no. 2, pp. 89-128, Mar. 2003.

[3] Holman, R. A., "Mold Temperature Measurement for Glass-Pressing Processes," Applications of Radiation Thermometry, ASTM STP 895, J. C. Richmond and D. P. Dewitt, Eds., American Society for Testing and Materials, Philadelphia, 1985, pp. 67-73.

[4] G. R. Peacock, "Ratio radiation thermometry thermometers in hot rolling and galvannealing of steel strip," *Proc. AIP*, vol. 684, no. 1, pp. 789-794, Sep. 2003.

[5] Z. M. Zhang, B. K. Tsai and G. Machin, "Overview of radiation thermometry," in *Radiometric temperature measurements. I. Fundamentals*, USA, Elsevier Inc., 2010, pp. 1-28.

[6] T. J. Quinn, "Radiation thermometry," in *Temperature*, London, UK, Academic Press, 1990, pp. 332-431.

[7] F. Sakuma and L. Ma, "Development of InGaAs Radiation Thermometers," in *SICE Annual Conference*, The University Electro-Communications, Japan, 20-22 Aug. 2008.

[8] "Optris GmbH, Germany, Product overview for non-contact temperature measurement [Online], Available: http://www.optris.co.uk/optris-gmbh.," Optris GmbH, [Online]. Available: http://www.optris.co.uk/optris-gmbh. [Accessed 22 Sep. 2014].

[9] G. P. Eppeldauer and H. W. Yoon, "AC-mode short-wavelength IR radiation thermometers for measurement of ambient temperatures," *Int. J. Thermophys*, vol. 29, no. 3, pp. 1041-1051, Mar. 2008.

[10] F. J. M. Meca, M. M. Quintas, F. J. R. Sánchez and P. R. Sainz, "Infrared temperature measurement system using photoconductive PbSe sensors without radiation chopping," *Sensors and Actuators A: Physical,* vol. 100, no. 2-3, pp. 206-213, Sep. 2002.

[11] V. Rudnev, D. Loveless, R. Cook and M. Black, "Temperature measurement," in *Handbook of induction heating*, New York, USA, Marcel Dekker, 2003, pp. 185-218.

[12] "LSP-HD 71-Plastic & Thermaforming datasheet," Land Instruments International Ltd, UK, 2010. [Online]. Available: http://www.landinst.com/products/lsp-hd-71-infrared-linescanner/documentation. [Accessed 22 Sep. 2014].

[13] Z. M. Zhang, B. K. Tsai and G. Machin, "Industrial applications of radiation thermometery," in *Radiometric temperature measurements. II. Applications*, USA, Elsevier Inc., 2010, pp. 2-54.

[14] P. J. Ker, A. R. Marshall, J. P. R. David and C. H. Tan, "Low noise high responsivity InAs electron avalanche photodiodes for infrared sensing," *physica status solidi (c),* vol. 9, no. 2, pp. 310-313, Feb. 2012.

[15] M. J. Hobbs, C. H. Tan and J. R. Willmott, "Evaluation of phase sensitive detection method and Si avalanche photodiode for radiation thermometry," *JINST.* , vol. 8, no. 3, p. P03016, Mar. 2013.

[16] A. R. J. Marshall, C. H. Tan, M. J. Steer and J. P. R. David, "Extremely Low Excess Noise in InAs Electron Avalanche Photodiodes," *IEEE Photonics Technology Letters,* vol. 21, no. 13, pp. 866-868, Jul. 2009.

[17] W. Sun, Z. Lu, X. Zheng, J. C. Campbell, S. J. Maddox, H. P. Nair and S. R. Bank, "High-gain InAs avalanche photodiodes," *IEEE Journal of Quantum Electronics.,* vol. 49, no. 2, pp. 154-161, Feb. 2013.

[18] I. C. Sandall, S. Zhang and C. H. Tan, "Linear array of InAs APDs operating at 2 μm," *Optics Express* , vol. 21, no. 22, pp. 25780-25787, 2013.

[19] A. R. J. Marshall, C. H. Tan, M. J. Steer and J. P. R. David, "Electron dominated impact ionisation and avalanche gain characteristics in InAs photodiodes," *Appl. Phys. Lett.,* vol. 93, no. 11, p. 111107, 2008.

[20] S. J. Maddox, W. Sun, Z. Lu, H. P. Nair, J. C. Campbell and S. R. Bank, "Enhanced low-noise gain from InAs avalanche photodiodes with reduced dark current and background doping," *Appl. Phys. Lett.,* vol. 101, no. 15, p. 151124, Oct. 2012.

[21] "InAs photovoltaic detectors," Hamamatsu Photonics K. K.,Solid State Division. Japan., [Online]. Available: http://www.hamamatsu.com/resources/pdf/ssd/p10090-01_etc_kird1099e07.pdf. [Accessed 22 Sep. 2014].

[22] "Indium arsenide detectors," Teledyne Judson Technologies LLC, USA., [Online]. Available: http://www.judsontechnologies.com/ind_ars.html. [Accessed 22 Sep. 2014].

[23] "PbSe photoconductive detectors P9696 Series," Hamamatsu Photonics K. K., Hamamstu, Japan, July 2013. [Online]. Available: http://www.hamamatsu.com/resources/pdf/ssd/p9696-02_etc_kird1073e03.pdf. [Accessed 22 Sep. 2014].

[24] G. Machin and B. Chu, "High-quality blackbody sources for infrared thermometry and thermography between -40 ºC and 1000 ºC," *Imaging Sci.,* vol. 48, pp. 15-22, 2000.

[25] P. J. Ker, A. R. J. Marshall, A. B. Krysa, J. P. R. David and C. H. Tan, "Temperature dependence of leakage current in InAs avalanche photodiodes," *IEEE Journal of quantum electronics,* vol. 47, no. 8, pp. 1123-1128, Aug. 2008.

Chapter 6 Photon-counting thermometer using a single photon avalanche photodiode

The primary motivation of photon counting thermometry is to measure the very low number of photons at short wavelength portion of the radiated blackbody spectrum. This in turn could extend the lower temperature limit of a radiation thermometer. In this chapter, the proposed photon counting thermometer using a single photon avalanche photodiode is evaluated.

6.1 Breakdown voltage definition

The experiment setup in Figure 3.11 was used for photon counting measurement. An Excelitas C30902SH-DTC Si SPAD [1] was evaluated in this work. A Keithley 2510 temperature controller was used to maintain the detector temperature at 20 ^{o}C. Figure 6.1 shows the dark current level of the Si SPAD at 20 ^{o}C, as measured by Keithley 237 SMU.

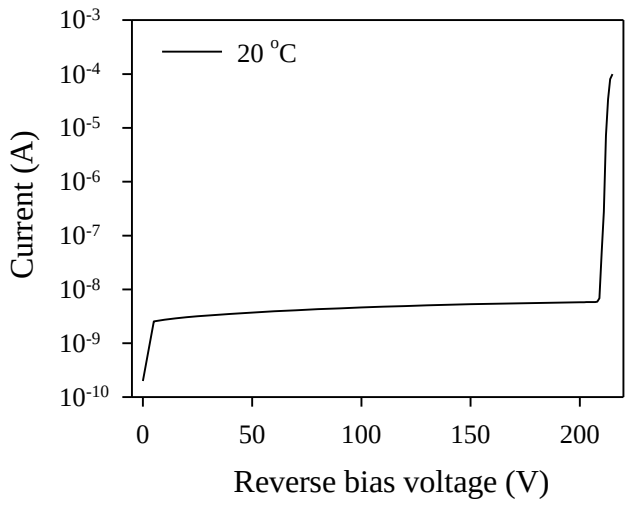

Figure 6.1 Dark current of commercial Si SPAD (C30902SH-DTC) at 20 ^{o}C

A common definition used for the breakdown voltage is the bias where the avalanche gain is infinity [2]. The reciprocal of dark current of the Si SPAD is plotted in Figure 6.2. From the dark current the breakdown voltage of 211 V can be estimated from the voltage axis when inverse of dark current approaches zero. However in the characterisation of

SPAD, breakdown voltage may also be defined as the bias voltage at which avalanche pulses with height larger than 1 mV can be measured. To measure the dark count rate (*DCR*), a ballast resistor of 47 KΩ and an amplitude threshold of 1 mV were used to quench and to register an avalanche breakdown event, respectively. Figure 6.2 also shows the *DCR* as a function of reverse bias. It can be seen that avalanche pulses start to be detected at 208.2 V which is lower than the breakdown voltage defined by the dark current. Since this chapter focuses on the photon counting mode the breakdown voltage will be defined as 208.2 V. Although the avalanche pulse can be detected at 208.2 V, the breakdown probability is very low. Therefore the average dark current is still measurable and well defined.

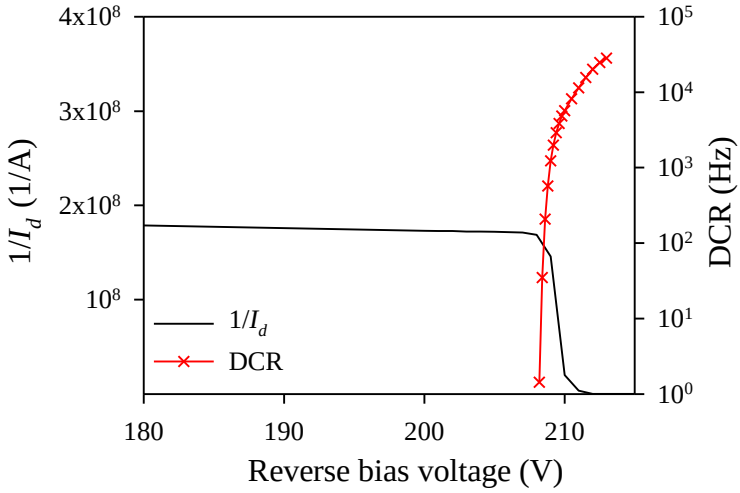

Figure 6.2 $1/I_d$ and *DCR* of Si SPAD versus reverse bias voltage at 20 ^oC

6.2 Photon counting measurement

To investigate the photon counting performance the total count rate (*TCR*) was measured when the SPAD was exposed to the blackbody with a temperature T_{BB} = 225 - 400 ^oC. For a given blackbody temperature the measurement was performed as a function of SPAD bias voltage. Each count rate measurement was registered over 10 s and 60 count rate measurements were recorded as functions of bias voltage and blackbody temperature.

As the bias increases above the breakdown voltage, both *DCR* and *TCR* increase dramatically due to increased breakdown probability. The ratio of *TCR* to *DCR* is plotted in Figure 6.3. It is clear that there are sufficient photons from the blackbody that produces

avalanche pulses even at temperature as low as 225 °C, suggesting that SPAD could be used for radiation thermometry.

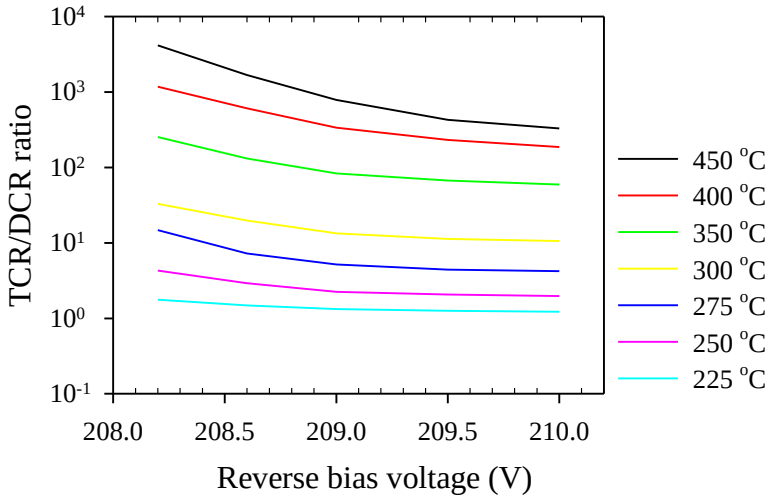

Figure 6.3 *TCR*/*DCR* count ratio as a function of reverse bias at different T_{BB}

When the bias voltage is marginally larger than the breakdown voltage, the ratio *TCR*/*DCR* increases rapidly with T_{BB} due to increased photon flux. However at higher bias voltage this ratio increases more gradually as *DCR* also increases with bias. Since the photon flux is constant at a given T_{BB}, the reduced *TCR*/*DCR* ratio suggests that the dark carrier generation rate increases with voltage to produce a faster rise in *DCR*.

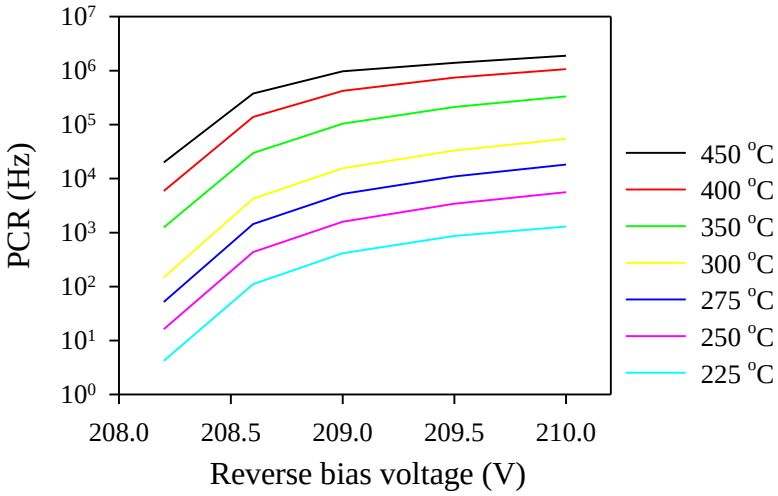

Figure 6.4 *PCR* as a function of reverse bias at different T_{BB}

To deduce the photon counting rate (*PCR*) in the free running mode, we assume [3]

$$PCR = TCR - DCR \tag{6.1}$$

Figure 6.4 shows the *PCR* at T_{BB} of 225 to 450 °C. As expected the *PCR* increases with bias due to increased breakdown probability. The *PCR* tends to saturate at high bias voltage. The rate of increase with bias also appears to be smaller at higher blackbody temperature. It is possible that the longer avalanche duration occurring at higher bias prevented the SPAD from detecting some of the arrival photons.

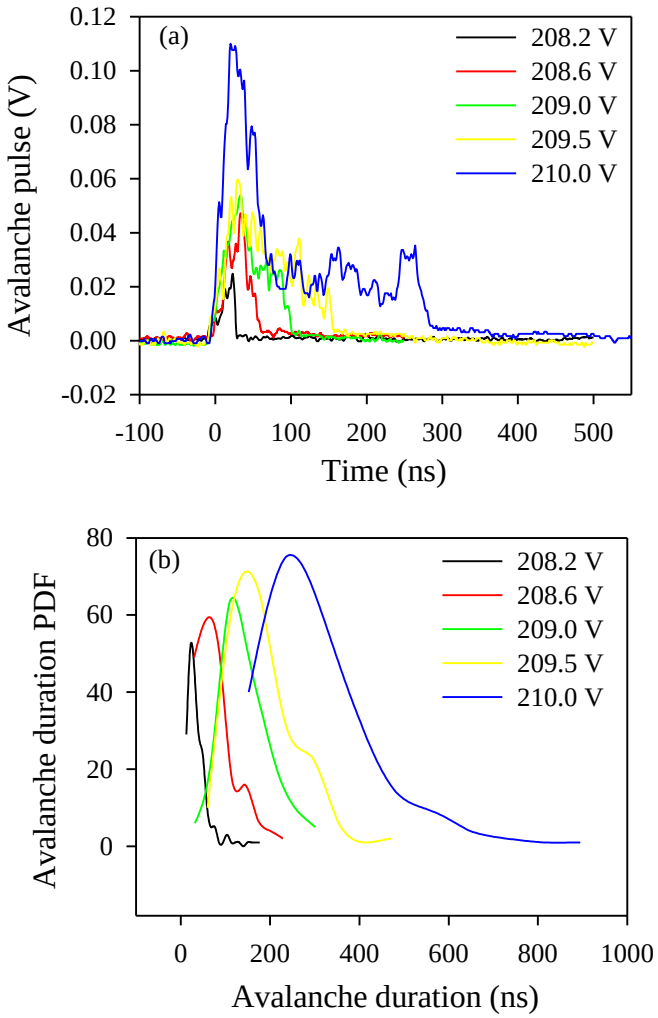

Figure 6.5 (a) Avalanche pulse and (b) avalanche pulse duration under different reverse bias at T_{BB} = 400 °C

Figure 6.5(a) shows the avalanche pulse recorded at bias voltages from 208.2 to 210.0 V. The peak current and the duration of avalanche pulse increase with bias. Within the duration of the avalanche pulse, the voltage across the SPAD fluctuates around its breakdown voltage, causing the avalanche current to fluctuate around an average value. The voltage across the SPAD will only be restored to the intended high bias when the avalanche current eventually quenches to a negligible value (due to statistical process in

impact ionisation). Therefore the SPAD will not respond to another photon before its avalanche duration is quenched and the bias voltage is restored. To further characterise the avalanche pulse duration, Figure 6.5(b) shows that the probability distribution function (PDF) of the avalanche duration derived from 200 measured pulses. At large voltages majority of the pulses are longer than 100 ns. Assuming the best case scenario with a detection probability of unity, the results imply that the SPAD tested is not designed to detect photon at a rate faster than 1 photon per 100 ns, corresponding to a rate of 10^7 photons/s. In reality the breakdown probability is much smaller than unity and the maximum detection rate will be lower than 10^7 photons/s. For instance, the breakdown probability at T_{BB} = 225 ^oC can be estimated from the ratio of *PCR* to photo-carrier generation rate (calculated using Planck's Law), giving values of 0.00036 to 0.11 at applied reverse biases of 208.2 V to 210.0 V, respectively.

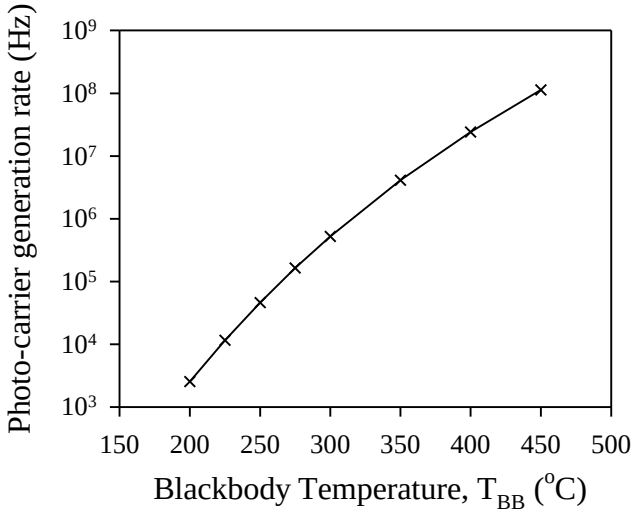

Figure 6.6 Photo-carrier generation rate, within the absorption spectral of Si, at different T_{BB}

Figure 6.6 shows the photo-carrier generation rate, within the absorption spectral of Si (400 to 1100 nm), as a function of T_{BB}. Since the number of photo-carriers is low at low T_{BB}, it is reasonable to assume that the SPAD will not be saturated by photons. However, it can be seen that there are 10^7 photons/s at T_{BB} = 375 ^oC, suggesting that the current SPAD will not be sufficiently fast to detect all the photons at higher T_{BB}, particularly when the avalanche pulse is long at large bias voltage.

The *PCR* is normalised to its value at T_{BB} = 300 ^oC (chosen to ensure minimal error in *PCR* and no photon saturation) to allow comparison to the photo-carrier generation rate

predicted using Planck's law in Figure 6.7. It is clear that at higher bias, the photo-carrier generation rate is too high, leading to saturation of the SPAD output counts at large bias and high T_{BB}. However it is also highly encouraging to note that at $T_{BB} \leq 300$ °C the *PCR* is consistent with the photon arrival rate predicted using Planck's Law. Photon counting based thermometry therefore seems to be an attractive approach to measure low temperatures.

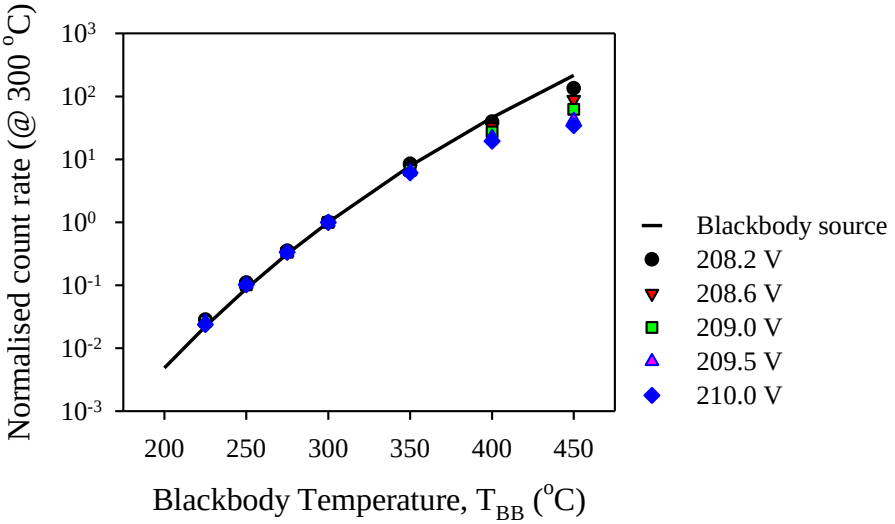

Figure 6.7 Normalised photon count rate and number of photo-generated carriers rate from blackbody source at different reverse bias

To evaluate the performance of this Si SPAD as a photon counting thermometer, the temperature error was analysed. As introduced in chapter 2, the temperature error was calculated based on the output photocurrent. The *PCR* is proportional to the number of injected photons, giving the relationship of [4]

$$PCR = \Phi \times PDE = \Phi \times \eta \times P_b \tag{6.2}$$

where Φ is the input photon flux. Thus, the *PCR* is also proportional to the photocurrent. Therefore, the temperature error, which accounts for measurement errors and the count rate fluctuation, can be defined as the temperature difference in the object that generate a signal to noise ratio, *SNR* of 1 [5]:

$$\Delta T = \frac{T_1 - T_2}{SNR} \ ℃ \tag{6.3}$$

where T_1 is object temperature and T_2 is background temperature, the *SNR* is defined as

$$SNR = \frac{PCR(T_1) - PCR(T_2)}{\sigma[PCR(T_2)]} \tag{6.4}$$

where σ[*PCR* (T_2)] is the standard deviation of *PCR* at T_2, the signal is calculated from the difference of mean *PCR*. This common scenario [6] is illustrated in Figure 6.8. In this scenario, the temperature error is the smallest detectible temperature difference as this differential signal could not be derived for *SNR* below 1.

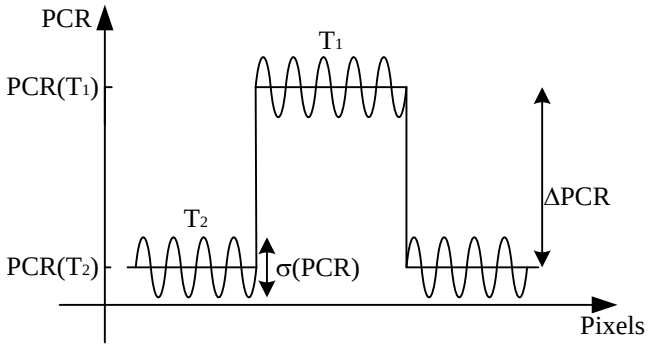

Figure 6.8 The scenario for temperature error analysis

Based on above scenario, the temperature error was calculated and plotted in Figure 6.9. As observed, the temperature error reduces with increasing T_{BB}. Due to increasing *PCR*, higher bias voltage gives lower temperature error. At a reverse bias of 210 V, this temperature error reduces from 0.16 °C at T_{BB} = 225 °C to 0.03 °C at T_{BB} = 450 °C. Assuming temperature error of 2 °C is acceptable, the results indicated that Si based photon counting thermometer can measure down to 225 °C when biased above its breakdown voltage of 208.2 V.

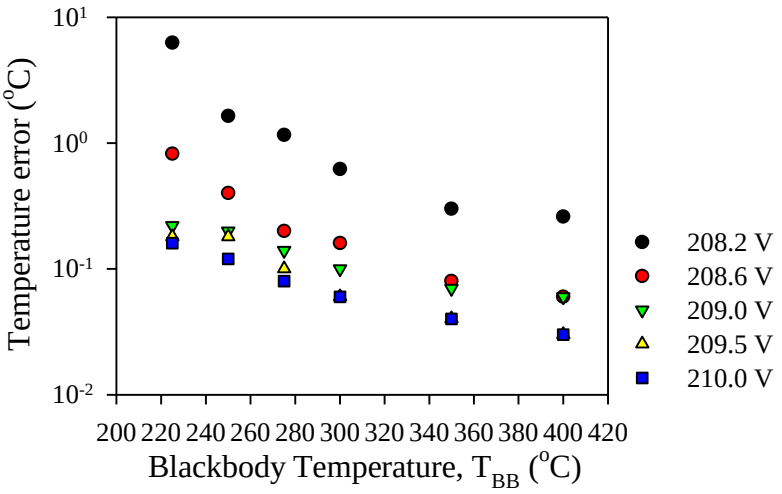

Figure 6.9 Temperature error at different reverse bias as a function of T_{BB}

6.3 Conclusion

In this chapter, we have studied a commercial Si SPAD performance as a photon counting thermometer. Assuming acceptable temperature error for photon counting thermometer is 2 ^{o}C, this Si SPAD can be measured down to 225 ^{o}C under 210 V bias operation. It was found that the photon count rate saturated at high bias and high blackbody temperature. Analysis suggests that the long avalanche duration at large bias contributed to the saturation of photon count.

References

[1] "Biomedical avalanche photodiodes: C30902SH, C30921SH, C30902SH-TC, C30902SH-DTC," PerkinElmer Optoelectronics Ltd., 2007. [Online]. Available: http://www.diyphysics.com/wp-content/uploads/2012/01/C30902S_SPAD_DATASHEET.pdf [Accessed 19 Sep 2014].

[2] F. Laforce, "Low noise optical receiver using Si APD," *Proc. SPIE*, vol. 7212, p. 721210, Feb. 2009.

[3] Hu, Chong, "Advanced devices and circuits for single photon avalanche diodes," Doctor of Philosophy in Electrical Engineering, School of Engineering and Applied Science, University of Virginia, Charlottesville, VA, 2009.

[4] M. Liu, C. Hu, J. C. Campbell, Z. Pan and M. M. Tashima, "Reduce afterpulsing of single photon avalanche diodes using passive quenching with active reset," *IEEE J. Quantum Electron.*, vol. 44, no. 5, pp. 430-434, 2008.

[5] "Standard test method for noise equivalent temperature difference of thermal imaging systems," ASTM Int'l, 8 May 2011. [Online]. Available: http://physics.ucf.edu/~ishigami/Teaching/Phys4083L/lab%20descriptions/NETD/ASTM%20for%20NETD.pdf[Accessed 19 Sep 2014].

[6] H. Budzier and G. Gerlach, "Sensor parameters," in *Thermal infrared sensors: theory, optimisation and practice*, John Wiley and Sons, Ltd, 2011, pp. 103-148.

Chapter 7 A Simple Monte Carlo model for prediction of avalanche process in silicon

7.1 Introduction

Silicon (Si) based avalanche photodiodes have been the preferred technology in detecting light with visible wavelengths due to the low cost and low excess avalanche noise. Si APD, which enhances the overall signal to noise ratio of a receiver module, has been employed to achieve high energy resolution and fast time response in X-ray detection [1,2] and used as single photon avalanche photodiodes in applications such as positron emission tomography systems [3], quantum key distribution (QKD) [4,5], photon counting time-of-flight sensor [6], non-invasive testing of VLSI circuits [7] and photon correlation spectroscopy [8]. Recently, Si APD have also been reported to provide better performance than conventional photodiodes in radiation thermometry [9].

Detailed understanding of impact ionisation process is essential for designing and modelling of high performance APDs, SPADs and Si based power devices. Equations of excess avalanche noise arising from randomness of avalanche multiplication, as derived by McIntyre [10], have been widely used. In McIntyre's equations electron and hole ionisation coefficients, α and β, which depend on the local electric field, control the excess avalanche noise factor. At electric fields below 300 kV/cm the ratio of β/α in Si is typically < 0.1 [11], leading to very low excess noise factor when electrons initiated the avalanche process. As electric field in the avalanche region increases, such as in sub-micron avalanche regions, β approaches α, which is expected to increase excess noise compared to those from thicker avalanche regions. However increase in excess noise was not observed experimentally. Pauchard *et al*. [12] and Tan *et al*. [13] showed that carriers' dead spaces, defined as the minimum distance a carrier travels to gain sufficient energy to impact ionize, keep the excess noise in thin (sub-micron) Si avalanche regions low. Significant dead spaces bring coherence in the avalanche multiplication process so the excess noise is reduced. Therefore an accurate and efficient model that includes carriers' dead spaces for avalanche multiplication modelling of sub-micron Si avalanche regions is needed.

Since the conventional local ionisation model is not suitable for submicron avalanche regions, more sophisticated models such as random path length model [14] and recurrence technique [15,16], have been used. They take into account dead space effects and hence can reproduce experimentally measured results more accurately. Both techniques require probability density functions (pdfs) of ionisation path length as inputs. Current models only describe the pdfs with reasonable accuracy in avalanche regions with slowly-varying electric field profiles. However, most practical Si APDs employ reach-through structures which have rapidly-changing electric field profiles in their avalanche regions. Thus their avalanche multiplication characteristics cannot be simulated accurately using these techniques. By contrast, the Monte Carlo technique, incorporating realistic carrier scattering mechanisms, remains one of the most accurate and powerful approaches for studying carrier transport process in APDs. A full band structure has been incorporated to study carrier transport on Si devices by Tang and Hess [17]. Fischetti *et al*. [18] also described detailed scattering effects in realistic situations in sub-micron Si devices using pseudopotential methods. Although such Full Band Monte Carlo (FBMC) models [17- 19 , 20] use realistic carrier transports in semiconductors, they require high computational power making them unattractive for device simulation, particularly for simulations of very large avalanche gain and avalanche breakdown statistics in APDs and SPADs respectively. An Analytical Band Monte Carlo (ABMC) model employed by Pop *et al*. [21] is much faster and simpler in computation. However it requires a number of material parameters, some of which are not easily verified experimentally, to reproduce experimental results accurately. More recently Plimmer *et al*. [22] have successfully replicated experimental results of GaAs by assuming an effective single parabolic conduction and valence bands in their Monte Carlo model. This Simple Monte Carlo model (SMC) using effective scattering rates as input parameters has also been developed for InAlAs [23] and InGaP [24], achieving good agreement between measured and simulated results.

This work extracted Si parameters for a SMC model by fitting the multiplication and excess noise data obtained from a range of sub-micron Si avalanche regions reported by Tan *et al*. [13,25]. It showed that the SMC model can provide good agreements with measured gain and excess noise factor on a range of Si devices with different electric field gradients. The ionisation coefficients and drift velocities for electrons and holes derived in this SMC model compare well with published values. The good agreement

achieved suggests that the Si SMC model can aid device simulation and/or design for APDs, SPADs and power devices.

7.2 Model description and validation

As in other Monte Carlo models such as FBMC and ABMC, a free carrier in a SMC model undergoes a drift motion under the influence of the electric field before encountering a random scattering mechanism. Instead of the complex band structure employed in FBMC and ABMC models, the SMC model adopts a single parabolic valley for electrons and holes. The details of the SMC model have been provided in previous publications [22-24]. Briefly the model in this work incorporates two main scattering mechanisms, intervalley phonon scattering and impact ionisation. A carrier gains energy from the electric field as it drifts during the free flight. At the end of the free flight either a phonon scattering or an impact ionisation event is selected. The effective phonon scattering rates for phonon absorption and phonon emission, R_{ab} and R_{em}, are described by

$$R_{ab} = \frac{N_F}{\lambda_m(2N_F+1)} \times \sqrt{\frac{2(E+\hbar\omega)}{m^*}} \tag{7.1}$$

and

$$R_{em} = \frac{N_F+1}{\lambda_m(2N_F+1)} \times \sqrt{\frac{2(E-\hbar\omega)}{m^*}} \tag{7.2}$$

respectively, where λ_m is an energy independent mean free path length between scatterings, E is the carrier's initial energy, $\hbar\omega$ is the phonon energy, m^* is the carrier effective mass and $N_F = (exp\left(\frac{\hbar\omega}{k_BT}\right) - 1)^{-1}$ is phonon occupation factor. After a phonon scattering the carrier's final energy is given by $E+\hbar\omega$ for phonon absorption or $E-\hbar\omega$ for phonon emission. The impact ionisation rate, R_{ii}, is included as an additional scattering mechanism and is described by the Keldysh [26] formula as

$$R_{ii} = C_{ii} \times (\frac{E-E_{th}}{E_{th}})^{\gamma} \tag{7.3}$$

where C_{ii} is a coefficient for impact ionisation rate, γ is the ionisation rate softness factor and E_{th} is the impact ionisation threshold energy. After impact ionisation the excess energy (E - E_{th}) is distributed evenly between the newly generated electron-hole pair and the original carrier [22].

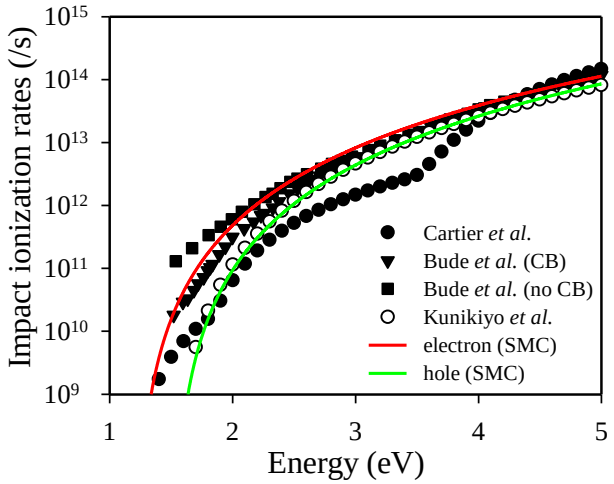

Figure 7.1 Ionisation rates for electron (solid symbols) derived by Cartier *et al*. [20] and Bude *et al*. [27] with or without collisional broadening (CB) effects, and ionisation rates for holes (open symbols) from Kunikiyo *et al*. [28]. The results calculated by SMC (lines) also showed in this work.

Since the ionisation rates in Si for electrons and holes, as shown in Figure 7.1, are well established, we have chosen to fit equation (7.3) to a number of reported rates for electrons ([20], [27]) and holes ([28]) to extract the values of R_{ii} and C_{ii}. We assumed E_{th} = 1.2 eV [29] and 1.5 eV [28] for electrons and holes respectively. A larger power exponent γ = 3.5 instead of γ = 2.0 used by Keldysh [26] to reflect the softer rise in impact ionisation rate in Si was used. The fitted ionisation rates for electrons and holes are also shown in Figure 7.1.

Next m^* and λ_m were used as the adjustable parameters in R_{ab} and R_{em}, to fit experimental mean gain and excess noise factors from a range of Si diodes [13, 25]. A single phonon energy $\hbar\omega$ of 63 meV (Fischer *et al*. [30]) was assumed. The values of $m^* = 0.6m_o$ for electrons and $0.9m_o$ for holes were found to yield good fits between experimental and simulated gain and excess noise factors, where m_o = 9.11 x 10^{-31} kg is the free electron mass. As reported by Plimmer *et al*. [22] different combinations of λ_m and m^* can produce the same effective scattering rates. The parameters used in the Si SMC model are summarised in Table 7.1.

A SMC simulation begins when an electron (or a hole) is injected into the multiplication region. Often the injection position is selected to be at either edge of the multiplication

region to give either pure electron multiplication or pure hole multiplication. The simulation ends when the multiplication chain terminates, which can only occur when the original electron, and all impact ionisation generated electrons and holes, have left the multiplication region. The total number of electrons produced at the end of this chain produces an avalanche gain, G. Due to the stochastic nature of impact ionisation, the value of G produced is different in each multiplication chain simulated. Therefore using a large number of simulations, typically at least 10 000, the mean gain, M, and the excess noise factor, $F = \langle G^2 \rangle / \langle G \rangle^2$, can be computed.

Table 7.1 Parameters used in Si SMC simulations

Parameters (unit)	Electrons	Holes
Phonon energy $\hbar\omega$ (meV)	63	63
Threshold energy E_{th} (eV)	1.2	1.5
Free path length λ_m (Å)	98	68
Impact ionisation rate coefficient C_{ii} (s^{-1})	2×10^{12}	4.4×10^{12}
Softness factor γ	3.5	3.5
Effective mass m^* (kg)	$0.6m_o$	$0.9m_o$

7.3 Drift velocity and avalanche process

The simulated electron and hole drift velocities are compared with experimental results from refs [31-33] in Figure 7.2. For holes, the simulated values are in agreement with the results of refs [31] and [32]. For electrons, SMC predicted slightly lower drift velocities than those reported in refs [31] and [33], suggesting that the Si SMC model is not yet fully optimised for simulation of temporal statistic at very low electric fields. Still, the broad agreement in carrier drift velocities, which are determined by phonon scattering rates at low electric fields, show that the phonon scattering rates in this work are reasonably realistic. Moreover, the slight underestimation in electron drift velocity is not a major concern since the Si SMC model is developed for simulations of avalanche multiplication in Si, which generally occurs at fields higher than 100 kV/cm.

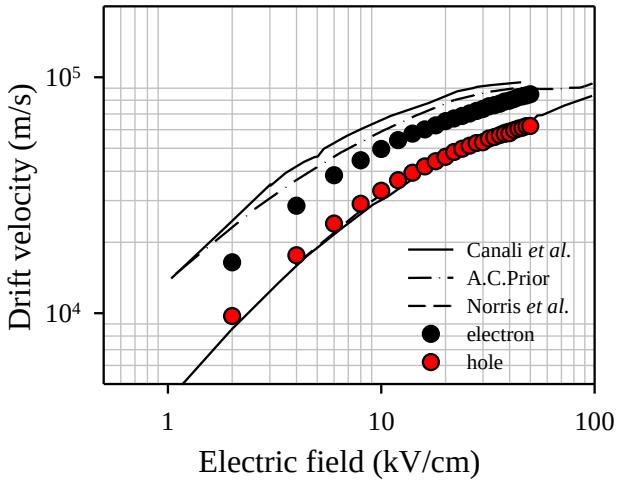

Figure 7.2 Comparison of drift velocities for electrons and holes from the SMC model (symbols) with experimental results from refs [31] and [33] (for electrons) as well as refs [31] and [32] (for holes).

7.4 Avalanche characterisation

To simulate the avalanche characteristics of the Si diodes from [13, 25], their electric field profiles were generated using doping profiles extracted from capacitance-voltage measurements, assuming a built-in potential of 1 V. The multiplication region width, w, and the doping concentrations of epilayers (N_p, N_i and N_n for p, i, and n layers, respectively) of the diodes are summarised in Table 7.2. The set of diodes includes p^+-i-n^+ and n^+-i-p^+ diodes (with w ranging from 0.082 to 0.82 μm) as well as a p^+n diode.

Table 7.2 Estimated avalanche region width and doping concentrations of the Si diodes used in this work.

Diode	structure	w (μm)	N_p (cm^{-3})	N_i (cm^{-3})	N_n (cm^{-3})
A	p^+-i-n^+	0.082	2.5×10^{18}	2×10^{16}	4×10^{18}
B	p^+-i-n^+	0.13	3.0×10^{18}	2×10^{16}	3×10^{18}
C	p^+-i-n^+	0.26	3.0×10^{18}	2×10^{16}	3×10^{18}
D	n^+-i-p^+	0.82	6.0×10^{18}	1.8×10^{16}	0.5×10^{18}
E	p^+n	-	7.5×10^{18}	-	7.5×10^{16}

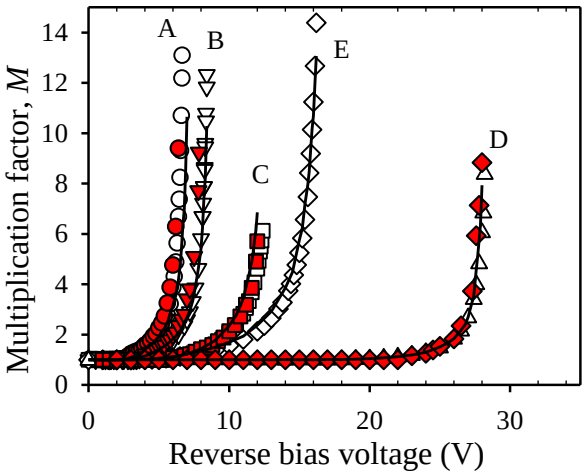

Figure 7.3 Pure electron multiplication simulated using SMC (lines) compared with experimental results obtained using 442 nm (open symbols) and 405 nm lasers (closed symbols) from [13] and [35], respectively.

Pure electron multiplication factors from SMC simulations are compared with experimental data from [13], which used 442 nm light to inject carriers into the avalanche regions, in Figure 7.3. Assuming an absorption coefficient of 4.6×10^4 cm^{-1} at 442 nm for Si [34] and using the appropriate layer thickness, 2.5% of the light penetrates into avalanche region for p^+-i-n^+ diodes while 16% of light enters the avalanche region in n^+-i-p^+ diode due to a thinner n^+ type cladding layer. A second set of avalanche gain data using a 405 nm laser [34], corresponding to less than 0.1 and 1.9% of light entering the high field regions of p^+-i-n^+ and n^+-i-p^+ diodes, respectively, was also included in Figure 7.3. The difference in the carrier generation profiles resulted in marginally lower gains in [13] compared to those in [35] for the p^+-i-n^+ diodes. The SMC simulation results are in good agreement with both sets of data. It is of particular interest to note that the SMC model accurately predicts the avalanche gain even when the electric field is highly non-uniform in the p^+n diode.

Figure 7.4 compares the excess noise factor versus multiplication factor simulated using the SMC model with data from [13], which used a 442 nm laser. For p^+-i-n^+ diodes, the excess noise factor from the model is in good agreement with the predominantly pure electron initiated excess noise. The 16% of light absorbed in avalanche region of the n^+-i-p^+ diode leads to a more mixed injection. Therefore it is not surprising that the pure hole injection initiated excess noise predicted by the SMC model is slightly higher than

the measured data under mixed injection conditions. In addition to the p^+-i-n^+ diodes, the SMC model also accurately simulated the excess noise from the p^+n diode with highly non-uniform electric field, indicating that the SMC model is appropriate for simulations of impact ionisation in devices with non-uniform electric fields.

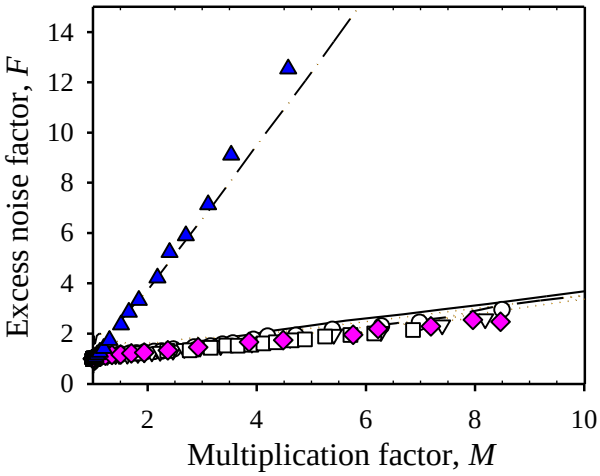

Figure 7.4 Comparison of excess noise factor versus multiplication factor simulated by the SMC model (lines) and the measured data using a 442nm laser (lines) on diodes A (○), B (▽), C (□), D (Δ) and E (◊).

In Figure 7.4, all three p^+-i-n^+ diodes had indistinguishable excess noise factors under pure electron injection. Tan *et al.* [13] suggested that the weak dependence of excess noise on avalanche region width observed experimentally is due to competing effects of the smaller ratio of α/β and the increasing dead space effects when avalanche region shrinks. To study these competing effects, without the influence of non-uniform electric field, this work simulated avalanche gains for a series of ideal p^+-i-n^+ diodes to obtain their α/β and dead space to avalanche width ratio, d/w. Figure 7.5 shows the ratios of α/β and d/w extracted for different values of w at a mean gain of 10. As w reduces from 0.3 to 0.05 μm, α/β ratio decreases from 3.42 to 1.23 while d/w ratio for electron increases from 0.19 to 0.49. The former increases the avalanche noise while the latter suppresses the avalanche noise. Hence the simulations confirmed that the competing effects of the α/β ratio and dead space significance lead to the weak dependence of excess noise on w, where at the gain of 10, F increases from 2.7 to 2.98 when w changes from 0.3 to 0.05 μm.

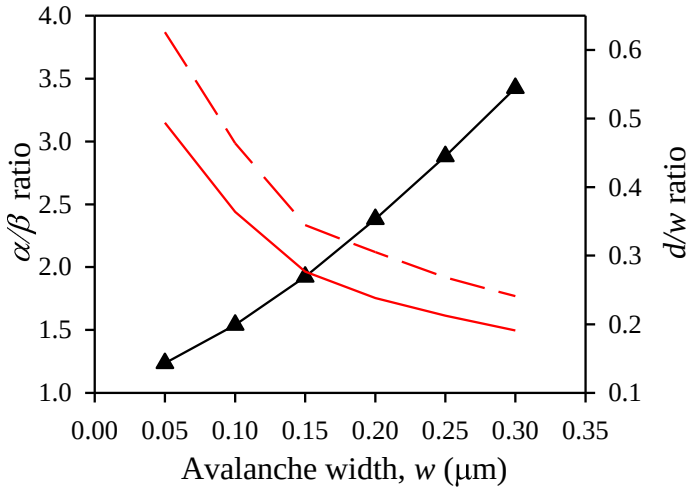

Figure 7.5 α/β ratio and d/w ratio for electrons (solid line) and holes (dashed line) in silicon diodes.

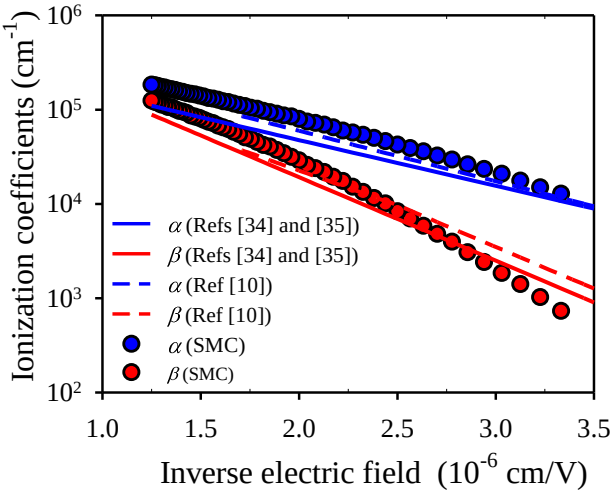

Figure 7.6 Electron and hole ionisation coefficients for Si from Massey *et al*. [35, 36] (solid lines) and Overstraeten *et al*. [11] (dashed lines), comparing with the SMC (symbols) calculated results.

The electric field dependences of α and β, deduced from the inverse of the mean distance between successive impact ionisation events, from the SMC model are shown in Figure 7.6. They are compared with experimental results reported by Massey *et al*. [35,36] and Overstraeten *et al*. [11]. Results from the SMC model are higher than experimental results at all electric fields, except for β at fields below 350 kV/cm. These discrepancies in impact ionisation coefficients between predicted and experimental results could be due to the following reasons. Massey *et al*. [35] assume that the electric field is constant in

the depletion region, although the depletion region extends into the *p* and *n* cladding regions. Consequently they overestimated the electric field in thin diodes, producing ionisation coefficients that are lower than the simulated results. Van Overstraeten and De Man [11] used a simple local ionisation theory available at the time of publication to derive the ionisation coefficients from gain measured on a series of *pn* junctions. They attempted to include the dead space effect by considering only data corresponding to bias above the ionisation threshold voltage. However it is now known that the local ionisation theory is inaccurate for modelling *pn* junctions with non-uniform electric field. This, combined with the simple but insufficient treatment of dead space effects, may have contributed to the discrepancies between their data and ours. In addition, it is possible that the hole ionisation and scattering rates are not fully optimised at low electric fields, where the impact ionisation process is dominated by electrons (due to the large α/β ratio at low electric fields). Therefore more experimental results from n^+-i-p^+ diodes with thicker avalanche regions, corresponding to lower electric fields, will be needed to verify the hole ionisation coefficient at low fields. Nevertheless slight inaccuracies in hole ionisation and scattering parameters are unlikely to have significant influence on the modelled gain.

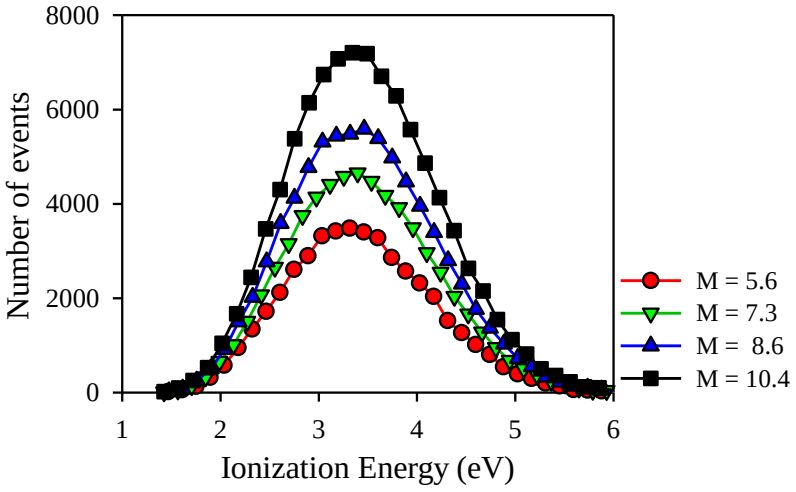

Figure 7.7 Energies of carriers occurring impact ionisation

To study the impact ionisation process in Si, the energies of ionizing carriers for different mean gain values were recorded and shown in Figure 7.7. It is clear that most carriers ionize when they acquire ~3.45 eV, approximately three times the band gap. The

Gaussian-like distribution in the hot carrier energy reflects the gradual increase in the ionisation rate in Si as shown in Figure 7.1.

7.5 Modelling of Si SPAD

As the SMC model has been proven to model APD accurately, it was used to model the avalanche process in a Si SPAD. In particular the avalanche duration which limits the photon counting rate will be analysed. The quenching resistor is known to affect the duration of the avalanche pulse. The equivalent circuit of the SPAD and a passive quenching circuit is shown in Figure 7.8 [37]. The SPAD is reverse biased through a large ballast resistor R_b. C_d and R_d are the diode capacitance and resistance respectively. The typical avalanche current pulse is also illustrated in Figure 7.8, where the peak avalanche current and self-sustaining level are given by

$$I_a(t) = \frac{V(t) - V_{bd}}{R_d} \tag{7.4}$$

$$I_s(t) = \frac{V(t) - V_{bd}}{R_d + R_b} \tag{7.5}$$

Therefore, the higher reverse bias results in higher peak current and self-sustaining current. This can be seen in Figure 6.5(a). To investigate the avalanche duration modelling of the avalanche pulse was carried out using the SMC model. In the simulation, it was assumed there is negligible voltage drop across the ballast resistor so that the avalanche current was allowed to build up to I_a. This is deem reasonable as the fast avalanche built-up current is assume to flow through the parasitic capacitor associated with the ballast resistor. Once the current reaches I_a, the voltages across the diode and the ballast resistor were updated such that the electric field in the SPAD fluctuates at a level around I_s. The avalanche pulse persists until avalanche process decayed.

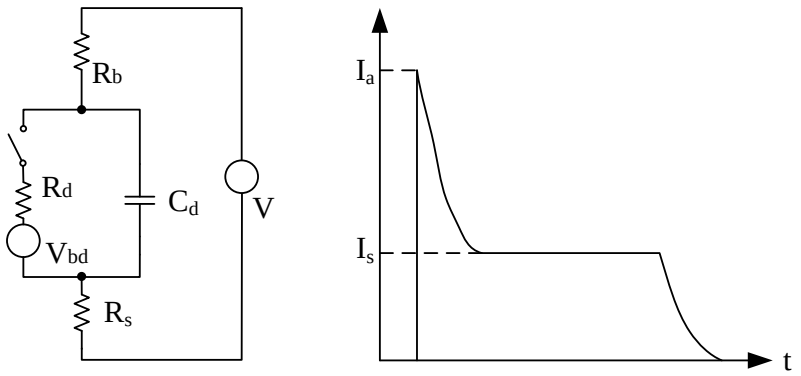

Figure 7.8 Equivalent circuit of a PQC and typical avalanche pulse

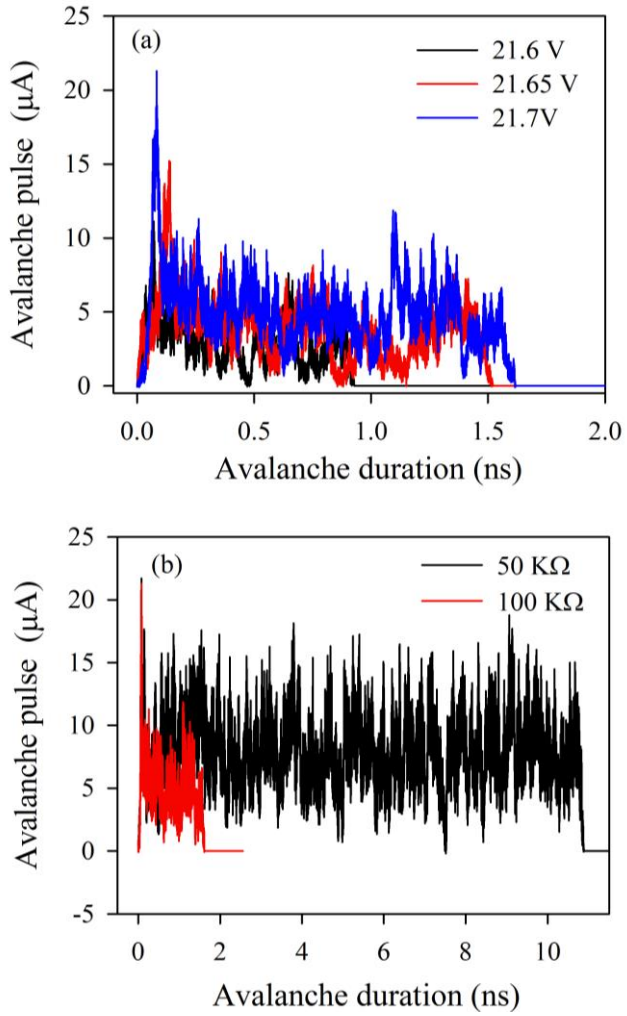

Figure 7.9 (a) Avalanche current pulse under different reverse bias by assuming a 0.5 μm *pin* diode and R_d = 10 KΩ, R_b = 100 KΩ and (b) Avalanche current pulse at 21.7 V with different ballast resistor and R_d = 10 KΩ.

Figure 7.9(a) shows the simulated avalanche pulses for a Si pin diode with and i-region of 0.5 μm, at different reverse bias. The results showed the qualitative behaviour of SPAD. The peak and self-sustaining current increases with bias, as observed experimentally. The simulated avalanche pulses with different ballast resistor at a reverse bias of 21.7 V is also shown in Figure 7.9(b). It is clear that a large ballast resistor results in a shorter avalanche duration and smaller self-sustaining current. However, the ballast resistor and diode capacitance also form a low pass filter in the circuit as shown in Figure 7.8. Larger ballast resistor gives higher RC time constant, leading to long charge and discharge cycles which is not included in the simulation. Therefore simulated avalanche duration is much shorter when compared with experimental results. The simulation

should be further developed to incorporate charging and discharging time so that optimised value of ballast resistor can be chosen to maximise the photon detection rate.

7.6 Conclusion

In this chapter, we have developed a SMC model, which requires much less computation time than FBMC and AMC models, to simulate the avalanche characteristics of Si APDs. The SMC model can accurately simulate multiplication and excess noise factors of diodes with avalanche region widths ranging from 0.082 to 0.82 μm as well as that of the p^+n diode with a highly non-uniform electric field profile. Impact ionisation coefficients of the model are comparable with experimental reports using local models. The model was also used to show that larger ballast resistor leads to shorter avalanche duration. This simple model is suitable for simulation of impact ionisation in Si APDs and SPADs.

References

[1] Y. Yatsua, Y. Kuramotoa, J. Kataokaa, J. Kotokua, T. Saitoa, T. Ikagawaa, R. Satoa, N. Kawaia, S. Kishimotob, K. Moric, T. Kamaed, Y. Ishikawae and N. Kawabata, "Study of avalanche photodiodes for soft X-ray detection below 20 keV," *Nucl. Instrum. Methods Phys. Res. A, Accel. Spectrom. Detect. Assoc. Equip.*, vol. 564, no. 1, pp. 134-143, August 2006.

[2] A. Q. R. Baron, S. Kishimoto, J. Morse and J. M. Rigal, "Silicon avalanche photodiodes for direct detection of X-rays," *J. Synchrotron Rad.* , vol. 13, no. 2, pp. 131-142, Feb. 2006.

[3] E. Roncali and S. R. Cherry, "Application of Silicon Photomultipliers to Positron Emission Tomography," *Ann Biomed Eng.*, vol. 39, no. 4, pp. 1358-1377, Apr. 2011.

[4] K. J. Gordon, V. Fernandez, P. D. Townsend and G. S. Buller, "A short wavelength gigahertz clocked fiber-optic quantum key distribution system," *IEEE Journal of Quantum Electronics*, vol. 40, no. 7, pp. 900-908, Jul. 2004.

[5] K. J. Gordon, V. Fernandez, G. S. Buller, I. Rech, S. D. Cova and P. D. Townsend, "Quantum key distribution system clocked at 2 GHz," *Optics Express*, vol. 13, no. 8, pp. 3015-3020, 2005.

[6] R. E. Warburton, A. McCarthy, A. M. Wallace, S. Hernandez-Marin, S. Cova, R. A. Lamb and G. S. Buller, "Enhanced performance photon-counting time-of-flight sensor," *Optics Express*, vol. 15, no. 2, pp. 423-429, 2007.

[7] F. Stellari, A. Tosi, F. Zappa and S. Cova, "CMOS circuit testing via time-resolved luminescence measurements and simulations," *IEEE Trans. Instrumentation and Measurement*, vol. 53, no. 1, pp. 163 - 169, Feb. 2004.

[8] M. Ghioni, S. Cova, I. Rech and F. Zappa, "Monolithic dual-detector for photon-correlation spectroscopy with wide dynamic range and 70ps resolution," *IEEE J. Quantum Electron.*, vol. 37, no. 12, pp. 1588 - 1593, Dec. 2001.

[9] M. J. Hobbs, C. H. Tan and J. R. Willmott, "Evaluation of phase sensitive detection method and Si avalanche photodiode for radiation thermometry," *JINST.* , vol. 8, no. 3, p. P03016, Mar. 2013.

[10] R. J. McIntyre, "Multiplication noise in Uniform avalanche diodes," *IEEE Trans. Electron. Dev.* , Vols. ED-13, no. 1, p. 164, Jan. 1966.

[11] R. V. Overstraeten and H. D. Man, "Measurement of the ionisation rates in diffused silicon p-n junctions," *Solid-State Electron.*, vol. 13, no. 5, p. 583–608, May 1970.

[12] A. R. Pauchard, P.-A. Besse and R. S. Popovic, "Dead Space Effect on the Wavelength Dependence of Gain and Noise in Avalanche Photodiodes," *IEEE Trans. Electron Dev.*, vol. 47, no. 9, pp. 1685-1693, Sep. 2000.

[13] C. H. Tan, J. C. Clark, J. P. R. David, G. J. Rees, S. A. Plimmer, R. C. Tozer, D. C. Herbert, D. J. Robbins, W. Y. Leong and J. Newey, "Avalanche noise measurement in thin Si p+- i -n+ diodes," *Appl. Phys. Lett.* , vol. 76, no. 26, pp. 3926-3928, Jun. 2000.

[14] D. S. Ong, K. F. Li, G. J. Rees, J. P. R. David and P. N. Robson, "A simple model to determine multiplication and noise in avalanche photodiodes," *J. Appl. Phys. 83 (1998) 3426*, vol. 83, no. 6, pp. 3426-3428, Mar. 1998.

[15] M. M. Hayat, B. E. A. Saleh and M. C. Teich, "Effect of dead space in gain and noise of double-carrier-multiplication avalanche photodiodes," *IEEE Trans. Electron. Dev.*, vol. 39, no. 3, pp. 546-552, Mar. 1992.

[16] M. M. Hayat, W. L. Sargeant and B. E. A. Saleh, "Effect of dead space on gain and noise in Si and GaAs avalanche photodiodes," *IEEE J. Quantum Elect.*, vol. 28, no. 5, pp. 1360-1365, May 1992.

[17] J. Y. Tang and K. Hess, "Impact ionisation of electrons in silicon (steady state)," *J. Appl. Phys.*, vol. 54, no. 9, pp. 5139-5144, Sep. 1983.

[18] M. V. Fischetti and S. E. Laux, "Monte Carlo analysis of electron transport in small semiconductor devices including band-structure and space-charge effects," *Phys. Rev. B* , vol. 38, no. 14, pp. 9721-9745, Nov. 1988.

[19] S. Jallepalli, M. Rashed, W.-K. Shih, C. M. Maziar and A. F. T. Jr., "A full-band Monte Carlo model for hole transport in silicon," *J. Appl. Phys.*, vol. 81, no. 5, pp. 2250-2255, Mar. 1997.

[20] E. Cartier, M. V. Fischetti, E. A. Eklund and F. R. McFeely, "Impact ionisation in silicon," *Appl. Phys. Lett.*, vol. 62, no. 25, pp. 3339-3341, Jun. 1993.

[21] E. Pop, R. W. Dutton and K. E. Goodson, "Analytic band Monte Carlo model for electron transport in Si including acoustic and optical phonon dispersion," *J. Appl. Phys.*, vol. 96, no. 9, pp. 4998-5005, Nov. 2004.

[22] S. A. Plimmer, J. P. R. David, D. S. Ong and K. F. Li, "A Simple Model for Avalanche Multiplication Including Dead space Effects," *IEEE Trans. Electron Dev.*, vol. 46, no. 4, pp. 769-775, Apr. 1999.

[23] S. C. L. T. Mun, C. H. Tan, Y. L. Goh, A. R. J. Marshall and J. P. R. David, "Modelling of avalanche multiplication and excess noise factor in $In_{0.52}Al_{0.48}As$ avalanche photodiodes using a simple Monte Carlo model," *J. Appl. Phys.*, vol. 104, no. 1, p. 013114, 2008.

[24] C. H. Tan, R. Ghin, J. P. R. David, G. J. Rees and M. Hopkinson, "The effect of dead space on gain and excess noise in $In_{0.48}Ga_{0.52}P$ p+in+ diodes," *Semicond. Sci. Technol.*, vol. 18, no. 8, pp. 803-806, Jul. 2003.

[25] C. H. Tan, J. P. R. David, G. J. Rees, R. C. Tozer and D. C. Herbert, "Treatment of soft threshold in impact ionisation," *J. Appl. Phys.*, vol. 90, no. 5, pp. 2538-2543, Sep. 2001.

[26] L. V. Keldysh, "Kinetic theory of impact ionisation in semiconductors," *Sov. Phys. JETP.*, vol. 37, pp. 509-518, 1960.

[27] J. Bude and K. Hess, "Impact ionisation in semiconductors: Effects of high electric fields and high scattering rates," *Phys. Rev. B*, vol. 49, no. 15, pp. 10958-10964, May 1992.

[28] T. Kunikiyo, M. Takenaka, M. Morifuji, K. Taniguchi and C. Hamaguchi, "A model of impact ionisation due to the primary hole in silicon for a full band Monte Carlo simulation," *J. Appl. Phys.*, vol. 79, no. 10, pp. 7718-7725, May 1996.

[29] C. L. Anderson and C. R. Crowell, "Threshold Energies for Electron-Hole Pair Production by Impact Ionisation in Semiconductors," *Phys. Rev. B*, vol. 5, no. 6, pp. 2267-2272, Mar. 1972.

[30] B. Fischer and K. R. Hofmann, "A full-band Monte Carlo model for the temperature dependence of electron and hole transport in silicon," *Appl. Phys. Lett.*, vol. 76, no. 5, pp. 583-585, Jan. 2000.

[31] C. Canali, G. Ottaviani and A. A. Quaranta, "Drift velocity of electrons and holes and associated anisotropic effects in silicon," *J. Phys. Chem. Solids.*, vol. 32, no. 8, pp. 1707-1720, 1971.

[32] C. B. Norris and J. F. Gibbons, "Measurement of high-field carrier drift velocities in silicon by a time-of-flight technique," *IEEE Trans. Electron Dev.* , Vols. ED-14, no. 1, pp. 38-43, Jan. 1967.

[33] A. C. Prior, "The filed-dependence of carrier mobility in silicon and germanium," *J. Phys. Chem. Solids.*, vol. 12, no. 2, pp. 175-180, Jan. 1960.

[34] D. E. Aspnes, "Optical functions of intrinsic Si: Table of refractive index, extinction coefficient and absorption coefficient vs energy (0 to 400 eV)," in *Properties of Silicon, EMIS Datareviews Series No 4*, London, England, INSPEC, 1988, p. 72.

[35] D. J. Massey, J. P. R. David and G. J. Rees, "Temperature Dependence of Impact Ionisation in Submicrometer Silicon Devices," *IEEE Trans. Electron Dev.* , vol. 53, no. 9, pp. 2328-2334, Sep. 2006.

[36] D. J. Massey, J. P. R. David and G. J. Rees, "Temperature dependence of avalanche multiplication in submicron silicon devices," in *Proceedings of ESSDERC*, Grenoble, France, 2005.

[37] S. Cova, M. Ghioni, A. Lacaita, C. Samori and F. Zappa, "Avalanche photodiodes and quenching circuits for single-photon detection," *Applied optics*, vol. 35, no. 12, pp. 1956-1976, Apr. 1996.

Chapter 8 Conclusion and future work

8.1 Conclusion

As temperature measurement is important in many applications, radiation thermometry are widely used in cases where contact measurement is not accessible. Photon detectors are preferred as sensor in radiation thermometers due to higher sensitivity at specific wavelength range and faster response than thermal detectors. This work reported a short wavelength two-colour detector for high temperature sensing ratio thermometer and InAs photodiode for narrow band thermometer and low temperature sensing. To further reduce the thermometer lower temperature point, a single photon detector for photon counting thermometer was therefore evaluated and a simple Monte Carlo model was demonstrated for APD/SPAD design.

An InGaAlAs-InGaAs two-colour photodetector for use in radiation thermometry was reported in chapter 4. The electrical and optical characterisation was performed and compared with a commercial two-colour Si-InGaAs photodetector. The InGaAlAs showed lower responsivity than Si but longer detection wavelengths while the InGaAs showed slightly higher response than the commercial InGaAs. In the radiation thermometry measurement, the *SNR*s were also comparable to the commercial diodes despite higher dark current. This is due to the amplifier noise dominant which is 125 $nV/Hz^{1/2}$ when the photocurrent is low. The lowest measured temperature of T_{BB} were 125 °C and 275 °C for InGaAlAs and InGaAs diode, respectively. Assuming the acceptable error is 2 °C, the InGaAlAs can be used to measure a T_{BB} = 294 °C while the InGaAs diode can measure T_{BB} = 131 °C. When employed as a ratio thermometer, the two-colour photodetector showed a temperature error of 12.8 °C at T_{BB} = 275 °C, but improves with temperature to 0.1 °C at T_{BB} = 450 °C. Although the detector is smaller than the optical spot size, the InGaAlAs-InGaAs ratio thermometer already outperformed a reported result from a Si-InGaAs. With further optimisation of the optical spot, it should be possible to further enhance the performance of the InGaAlAs-InGaAs ratio thermometer.

An InAs photodiode with a cut-off wavelength of 3.6 μm, provides higher performance than a commercial PbSe detector, confirming its huge potential in infrared sensing applications. The InAs diode in this work showed a higher detectivity than commercial InAs and PbSe detectors within the wavelength range of interest. The evaluation of InAs photodiodes for radiation thermometry was performed. When compared with PbSe, InAs showed higher signal across the entire measurement range with or without narrow band filter. Uncooled InAs photodiode can measure temperature down to 50 ^{o}C with a temperature error of 0.17 ^{o}C. With a 3.43 μm narrow band filter, the output signal was still strong enough to perform accurate temperature measurement, showing its accuracy for temperature measurement on materials with C-H bonds. To further improve the temperature resolution, cooled InAs diode was therefore studied as low temperature thermometer. From 295 to 200 K, the device dark current reduces by 3 orders of magnitude while the photocurrent drops by around 50 % due to a shorter cut-off wavelength. Thus, the *SNR* from cooled detector was significantly improved and the temperature error improved from 0.46 to 0.048 ^{o}C at a T_{BB} = 37 ^{o}C when the detector was cooled from room temperature to 200 K. This verifies the potential of using InAs for low temperature sensing including human body temperature sensing.

The performance of a photon counting thermometer using a commercial Si SPAD was also investigated. With higher internal gain, the APD and SPAD were reported to have much higher sensitivity, giving better *SNR* than a conventional photodiode. In this work, the temperature measurements were performed from 225-450 ^{o}C. As expected, the *PCR* increased with reverse bias and T_{BB} due to increasing breakdown probability and increasing number of photons respectively. However it was also found that the *PCR* tends to saturate at high bias and high T_{BB}. This was attributed to the long avalanche duration at high reverse bias which defined a maximum detection rate, limiting the *PCR* at high T_{BB}. Nevertheless if the acceptable temperature error was 2 ^{o}C, the Si SPAD can be used to measure down to 225 ^{o}C under a reverse bias from 208.6 V to 210.0 V.

Since the APD/SPAD provided better performance than photodiode, a proper model was essential for designing and modelling of APD/SPAD. A simple Monte Carlo model was developed to understand of impact ionisation process and SPAD operation. To validate the model, five Si devices were studied, including p^{+}-i-n^{+} and n^{+}-i-p^{+} diodes with

avalanche region widths ranging from 0.082 to 0.82 μm as well as a p^+n diode with a highly non-uniform electric field profile. This SMC model could accurately predict the multiplication and excess noise factor for all five diodes. It also produced comparable impact ionisation coefficients with that from local model. By modeling a simple PQC, this model was also used to simulate the avalanche current pulse from SPAD operation. It confirms that avalanche duration is longer at high biases and when the ballast resistor value is small. This demonstrates the modelling capability of the SMC for designing APD/SPADs.

8.2 Future work

As mentioned in chapter 4, the InGaAlAs diode and InGaAs diode still suffered from higher dark current than commercial devices. The leakage current from InGaAs might come from the non-optimised fabrication process and imperfect crystal. Further fabrication and growth conditions must be optimised to reduce leakage current and to achieve high quality wafer. The low responsivity from InGaAlAs quaternary could be due to poor collection efficiency caused by high defect density in thick materials. In addition the photocurrent is also blocked by InGaAs contact layer which can be removed to further improve the quantum efficiency. Anti-reflection coating needs to designed and deposited to improve device responsivity in future fabrication. Thus, device structure optimisation needs to be done to improve the detector performance. Furthermore, this structure can be fabricated into a linear array or focal plane array and tested as a ratio thermal imager incorporating a read-out circuit. As a monolithic structure, this InP lattice-matched material system can be easily to grown as a multi-colour detector by changing the composition in InGaAlAs quaternary.

The InAs photodiode studied in chapter 5 was not fabricated with an AR-coating layer. AR-coating for InAs can be utilized to maximise its quantum efficiency in future work. Currently only a InAs photodiode is evaluated as radiation thermometer in this work. This is due to exposed mesa diodes suffering from rapidly increased dark current under high reverse bias. Most research have been done related to InAs APD which can give higher sensitivity than photodiode [1,2]. However, the surface leakage still needs to be reduced for high bias operation. Passivation techniques and growth improvements have been suggested to deal with this problem. Performing the thermometry measurement

using a InAs APD could achieve better results if the dark current can be reduced significantly below the amplifier noise equivalent current. Fabrication of a InAs linear array could be done to evaluate its performance as a line-scanner in the plastic industry operating at 3.43 μm.

In chapter 6, the *PCR* shows a saturation at high reverse bias and high T_{BB} due to longer avalanche pulse duration in free running mode. As discussed, with increasing bias the *DCR* increases faster than the *PCR* in the free running mode. Consequently the SPAD cannot be operated at very high reverse bias to achieve high breakdown probability. To avoid such problems, the gated operation mode can be employed to quench the avalanche pulse efficiently and more quickly. By using high frequency and short on time gated pulse shown in Figure 8.1 the avalanche pulse duration can be reduced to increase the count rate to eliminate the count rate saturation problem. In order to get a perfect square wave, a capacitive quenching circuit [3] can be employed for the measurement. The measurement was taken over 10 s and 60 count rate under each conditions which need to be compared with short duration measurement to test the speed of measurement for achieving same stabilisation. As the Si SPAD also responds to the background visible light which requires a perfect dark environment during the measurement, the current system must be optimised to reduce background count rate.

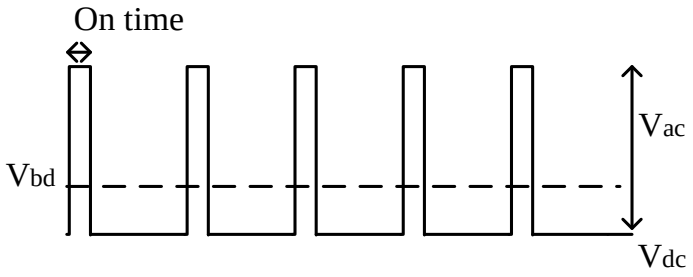

Figure 8.1 Typical gated quench operation

The SPAD simulation work based on the SMC model in chapter 7 only shows a simple PQC effect. In a passive quench circuit, the diode resistor and capacitance forms a charge loop during the avalanche build up process while ballast resistor and diode capacitance forms a discharge circuit after breakdown. However, this charge and discharge effect is not included in the SMC model, causing a much shorter avalanche pulse compare with experimental results. This is more important for time-resolved photon counting applications. An RC effect should be incorporated in the model to achieve more accurate

prediction in SPAD design. Ramirez *et al.* [4] presented a self-regulating avalanche model based on recurrence technique for SPAD simulation. Their model incorporated the charge and discharge effect through diode capacitance and ballast resistor by current evolution over a sufficiently small time duration. As a result, the instantaneous impact ionisation coefficients are recalculated in response to the voltage change on diode. In similarity, this instantaneous RC effect could also be employed in the SMC model. Furthermore, as most APD/SPAD always employ a changing electric field profile which the local model [5], recurrence technique [6] and RPL mode [7] are not appropriate. The breakdown statistics from device structures with changing electric field profiles can be predicted using the SMC.

References

[1] A. R. J. Marshall, C. H. Tan, M. J. Steer and J. P. R. David, "Electron dominated impact ionisation and avalanche gain in InAs photodiodes," *Appl. Phys. Lett.*, vol. 93, no. 11, p. 111107, Sep. 2008.

[2] A. R. J. Marshall, C. H. Tan, M. J. Steer and J. P. R. David, "Low noise InAs avalanche photodiodes for high sensitivity FPAs," *Proc. of SPIE,* vol. 7113, p. 71130H, 2008.

[3] S. J. Dimler, J. S. Ng, R. C. Tozer, G. J. Rees and J. P. R. David, "Capacitive quenching measurement circuit for geiger-mode avalanche photodiodes," *IEEE Journal of Selected Topics in Quantum Electronics,* vol. 13, no. 4, pp. 919-925, Aug 2007.

[4] D. A. Ramirez, M. M. Hayat, G. J. Rees, X. Jiang and M. A. Itzler, "New Perspective on passively quenched single photon avalanche diodes: effect of feedback on impact ionisation," *Optics Express,* vol. 20, no. 2, pp. 1512-1529, Jan. 2012.

[5] P. Yuan, K. A. Anselm, H. N. C. Hu, C. Lenox, A. L. Holmes, B. G. Streetman, J. C. Campbell and R. J. McIntyre, "A new look at impact ionisation-Part II: Gain and noise in short avalanche photodiodes," *IEEE Trans. Electron. Dev.,* vol. 46, no. 8, pp. 1632-1639, 1999.

[6] M. M. Hayat, B. E. A. Saleh and M. C. Teich, "Effect of dead space in gain and noise of double-carrier-multiplication avalanche photodiodes," *IEEE Trans. Electron. Dev.,* vol. 39, no. 3, pp. 546-552, 1992.

[7] D. S. Ong, K. F. Li, G. J. Rees, J. P. R. David and P. N. Robson, "A simple model to determine multiplication and noise in avalanche photodiodes," *J. Appl. Phys.,* vol. 83, no. 6, pp. 3426-3428, 1998.

Appendix A: Fabrication of InGaAlAs-InGaAs two-colour photodetector

The InGaAlAs-InGaAs two-colour detector fabrication assumes the wafer with similar structure in Table A1. Fabrication steps are listed here.

- Sample cleaning
- N-metal contact on substrate
- Top p-metal contact
- First mesa etch for top InGaAlAs diode
- Second mesa etch for connecting InGaAlAs-InGaAs n-p junction
- Lower contact
- Annealing for metal contacts
- Third mesa etch for bottom InGaAs diode

Many of the fabrication steps require the 3-step sample cleaning below,

1) Boil the sample in n-butyl acetate for 30 s
2) Boil the sample in Acetone for 30 s
3) Boil the sample in isopropyl alcohol (IPA) for 30 s

Table A1: Typical two-colour wafer structure grown on an n^+ substrate.

Layer number	Type	Material	Doping level (cm^3)	Thickness (nm)
7	P	$In_{0.53}Ga_{0.47}As$	2×10^{18}	50
6	P	$In_{0.53}Ga_{0.25}Al_{0.22}As$	2×10^{18}	500
5	I	$In_{0.53}Ga_{0.25}Al_{0.22}As$	u.i.d	2500
4	N	$In_{0.53}Ga_{0.25}Al_{0.22}As$	2×10^{18}	300
3	P	$In_{0.53}Ga_{0.25}Al_{0.22}As$	2×10^{18}	300
2	I	$In_{0.53}Ga_{0.47}As$	u.i.d	2500
1	N	$In_{0.53}Ga_{0.47}As$	2×10^{18}	500
0	N^+	InP	---	---

Step-by-step fabrication:

1. Sample cleaning

1) Dip cotton buds into cold n-butyl and use them to wipe sample surface to remove dust
2) 3-step sample cleaning
3) Remove the sample from IPA, keeping a complete film of solvent on the surface. Blow dry the sample using a nitrogen gun.

2. Deposit N-metal contact on substrate

1) Clean the substrate surface using an Asher for 1-2 minute before depositing metal contacts
2) Use a Sputterer to deposit Ti/Au (20/200 nm) onto the substrate to form n-contacts
3) 3-step sample cleaning

3. Deposit Top p-metal contact

1) Bake the sample using a hotplate at 100 ^{o}C for 1 minute.
2) Spin-coat top side of the sample with a positive photo-resist (BPRS100 at 4000 RPM for ~ 30 s). Then bake the sample again at 100 °C for 1 minute.
3) Align photolithography mask (**Top contact**) on the sample with hardened photo-resist. UV exposure for 4.0 s to create patterns of p-metal contacts.
4) Develop the UV-exposed photoresist by placing the sample in a solution of MF26A: DIW = 1:0.7 for 1 minute, and then rinse the sample in DIW and dry the sample.
5) Check the developed pattern under a microscope
6) Clean the surface using an Asher for 1-2 minute
7) Use a Sputterer to deposit Ti/Pt/Au (10/30/200 nm) onto the sample to form p-contact
8) Lift-off: place sample in acetone for several minutes and squirt acetone onto the sample to remove the metals outside the contact area)
9) 3-step sample cleaning

4. First mesa etch for top InGaAlAs diode

1) Bake the sample using a hotplate at 100 ^{o}C for 1 minute.
2) Spin-coat top side of the sample with a positive photo-resist (BPRS200 at 4000 RPM for ~ 30 s). Then bake the sample again at 100 °C for 1 minute.
3) Align photolithography mask (**1st Mesa**) on the sample with hardened photo-resist. UV exposure for 8.0 s to create patterns of mesas covered with photo-resist.
4) Develop the photo-resist on the sample by placing the sample in a solution of MF26A: DIW = 1:0.7 for 1 minute and rinse in DIW and dry the sample.
5) Inspect the developed pattern under microscope
6) Measure photo-resist thickness.

7) Prepare mesa etch mixture of H_2SO_4: H_2O_2: H_2O (ratio of 1: 8: 80).
8) Place the sample into the etch mixture to achieve the desired etch depth (down to Layer 4 in Table A1).
9) Once the desired etch depth is reached, remove photo-resist by placing the sample in acetone.
10) 3-step sample cleaning.

5. Second mesa etch for connecting InGaAlAs-InGaAs n-p junction

1) Bake the sample using a hotplate at 100 ^oC for 1 minute.
2) Spin-coat top side of the sample with a positive photo-resist (BPRS100 at 4000 RPM for ~ 30 s). Then bake the sample again at 100 °C for 1 minute.
3) Align photolithography mask (**2nd Mesa**) on the sample with hardened photo-resist. UV exposure for 4.0 s to create patterns of mesas covered with photo-resist.
4) Develop the photo-resist on the sample by placing the sample in a solution of MF26A: DIW = 1:0.7 for 1 minute and rinse in DIW and dry the sample.
5) Inspect the developed pattern under microscope
6) Measure photo-resist thickness.
7) Prepare mesa etch mixture of H_2SO_4: H_2O_2: H_2O (ratio of 1: 8: 80).
8) Place the sample into the etch mixture to achieve the desired etch depth (down to Layer 3 in Table A1).
9) Once the desired etch depth is reached, remove photo-resist by placing the sample in acetone.
10) 3-step sample cleaning.

6. Deposit Lower contact

1) Bake the sample using a hotplate at 100 ^oC for 1 minute.
2) Spin-coat top side of the sample with a positive photo-resist (BPRS100 at 4000 RPM for ~ 30 s). Then bake the sample again at 100 °C for 1 minute.
3) Align photolithography mask (**Lower contact**) on the sample with hardened photo-resist. UV exposure for 4.0 s to create patterns of p-metal contacts.
4) Develop the UV-exposed photoresist by placing the sample in a solution of MF26A: DIW = 1:0.7 for 1 minute, and then rinse the sample in DIW and dry the sample.

5) Check the developed pattern under a microscope
6) Clean the surface using an Asher for 1-2 minute
7) Use a Sputterer to deposit Ti/Pt/Au (10/30/200 nm) onto the sample to form ohmic contact
8) Lift-off: place sample in acetone for several minutes and squirt acetone onto the sample to remove the metals outside the contact area)
9) 3-step sample cleaning

7. Annealing for metal contacts

1) Use a Rapid Thermal Annealer to anneal the metal contacts at 420 °C for 30 seconds.

8. Third mesa etch for bottom InGaAs diode

1) Bake the sample using a hotplate at 100 ^{o}C for 1 minute.
2) Spin-coat top side of the sample with a positive photo-resist (BPRS200 at 4000 RPM for ~ 30 s). Then bake the sample again at 100 °C for 1 minute.
3) Align photolithography mask (**3rd Mesa**) on the sample with hardened photo-resist. UV exposure for 8.0 s to create patterns of mesas covered with photo-resist.
4) Develop the photo-resist on the sample by placing the sample in a solution of MF26A: DIW = 1:0.7 for 1 minute and rinse in DIW and dry the sample.
5) Inspect the developed pattern under microscope
6) Measure photo-resist thickness.
7) Prepare mesa etch mixture of H_2SO_4: H_2O_2: H_2O (ratio of 1: 8: 80).
8) Place the sample into the etch mixture to achieve the desired etch depth (down to Layer 1 in Table A1).
9) Once the desired etch depth is reached, remove photo-resist by placing the sample in acetone.
10) 3-step sample cleaning.

∗Estimated thickness for different photoresist:

BPRS100: ~ 1 μm

BPRS200: ~ 2 μm

Appendix B: Fabrication of InAs photodiodes with Newpin mask

The fabrication procedure consists of sample cleaning, back contact, top contact, mesa etch and SU 8 passivation. Detailed fabrication steps are listed below

1. Sample cleaning
    1) Cleave a small sample from InAs wafer
    2) Dip cotton buds into cold n-butyl and use them to wipe sample surface to remove dust
    3) 3-step sample cleaning (boiled in n-butyl, acetone and isopropyl alcohol for 30 s)
    4) Remove the sample from IPA, keeping a complete film of solvent on the surface. Blow dry the sample using a nitrogen gun.

2. Back contact
    1) Clean the substrate surface using an Asher for 1-2 minute before depositing metal contacts
    2) Use a Sputterer or evaporator to deposit Ti/Au (20/200 nm) onto the substrate to form back contact
    3) 3-step sample cleaning

3. Top contact
    1) Bake the sample on a hotplate at 100 ^{o}C for 1 minute.
    2) Spin-coat top side of the sample with a positive photo-resist (BPRS200 at 4000 RPM for ~ 30 s). Then bake the sample again at 100 °C for 1 minute.
    3) Align photolithography mask (**Top contact**) on the sample with hardened photo-resist. UV400 exposure for 8.0 s to create patterns of p-metal contacts.
    4) Develop the UV-exposed photoresist by placing the sample in a solution of MF26A: DIW = 1:0.7 for 1 minute, and then rinse the sample in DIW and dry the sample.
    5) Check the developed pattern under a microscope
    6) Clean the surface using an Asher for 1-2 minute
    7) Use a Sputterer or evaporator to deposit Ti/Pt/Au (20/200 nm) onto the sample to form top contact
    8) Lift-off: place sample in acetone for several minutes and squirt acetone onto the sample to remove the metals outside the contact area)

9) 3-step sample cleaning

4. Mesa etch

1) Bake the sample using a hotplate at 100 ºC for 1 minute.
2) Spin-coat top side of the sample with a positive photo-resist (BPRS200 at 4000 RPM for ~ 30 s). Then bake the sample again at 100 °C for 1 minute.
3) Align photolithography mask (**Deep Mesa**) on the sample with hardened photo-resist. UV400 exposure for 8.0 s to create patterns of mesas covered with photo-resist.
4) Develop the photo-resist on the sample by placing the sample in a solution of MF26A: DIW = 1:0.7 for 1 minute and rinse in DIW and dry the sample.
5) Inspect the developed pattern under microscope
6) Measure photo-resist thickness using DEKTEK_2_150.
7) Prepare mesa etch recipes:
   A. Phosphoric Acid: Hydrogen Peroxide: DIW (1:1:1)
   B. H_2SO_4: H_2O_2: H_2O (ratio of 1: 8: 80)
8) Using solution A to etch the InAs sample to the desired depth, then using solution B to do finish clean for 30 s.
9) Using the acetone to remove the photoresist, then dip the sample in solution A for 10 s and solution B for 20 s.

5. SU 8 passivation

1) Bake the sample on a hotplate at 100 ºC for 1 minute, spin SU 8 at 4000 RPM for 30 s
2) Bake the sample on a hotplate at 95 ºC for 15 minutes, then let it cool down for 10 minutes
3) Using UV400 mask aligner to exposure (**Mesa etch**) the sample for 50s
4) Bake the sample on a hotplate at 95 ºC for 10 minutes, then let it cool down for 10 minutes
5) Develop the sample in EC solvent for 1 minutes and then dip into isopropyl alcohol for 1 minutes and dry the sample

Appendix C: Radiation thermometry measurement procedure

This section introduces the radiation thermometry procedures using setup in Figure 3.9.

1. Assemble the setup in Figure 3.9, switch on the blackbody source, set a starting measurement temperature point using blackbody controller and allow the blackbody source to warm up for at least 40 minutes to stabilise. (For optical alignment, high temperature produces higher output signal which is easier for optical alignment)

2. Once the blackbody temperature is stable perform the alignment to make sure blackbody aperture, focusing lens and detector are in the same line of sight. First of all, the focusing lens and blackbody source distance can be kept. Then using XYZ stage to align detector position for achieving optimum alignment. This is can be monitored through output voltage readings from LIA.

3. After alignment, the setup is ready for measurements. Execute the LabVIEW program called "read_SR810.vi" to read the output voltage from LIA. This program is manually written to control LIA. Before running the program, users need to set a directory path to save the file (format .csv or .txt). Check the GPIB address is correct, corresponding to the LIA. Setting the time constant of 1 seconds in LIA and "settling time" in program as at least 8 seconds.

4. Once the program and LIA settings ready, click "Run" and "Stop" button to start and stop measurement. In the "Count" field, the number of samplings will be recorded. The sampling time is 50 milliseconds in the program.

5. This measurement is repeated at different blackbody temperature.

6. If uncooled detector need to be measured, using Helium closed cycle cryostat in Figure 3.4 for cooling detector and Land Instruments Landcal P80P blackbody source for low blackbody temperature measurement.

Blackbody source user precaution: (IR-563/301 blackbody source)

IR-563/301 blackbody source is used for high temperature measurement and its operation range is 50-1050 ºC. Once the power is on, the cooling fan is running to avoid the overheat problem. After switching off the blackbody controller, the blackbody source still need to cool down for at least 5 hours. Therefore, the power for blackbody source is always supplied through a 24 hour timer from power socket. By using a needle to set the timer, the blackbody fan can keep running for more than 5 hours before timer switched off.

Appendix D: Photon counting thermometry measurement procedure

This section lists procedure and some precautions in photon counting thermometry measurement using setup in Figure 3.11.

1. Assemble the setup in Figure 3.11. The Excelitas C30902SH-DTC Si SPAD is connected to a passive quench circuit and sealed in a homemade box. The main equipment used in this setup is listed below

   IR-563/301 blackbody source and controller
   ZFL-1000LN low noise amplifier
   Keithley 2510 TEC SourceMeter
   Keithley 6517A Electrometer/High Resistance Meter
   Keithley 2700 Multimeter/Data Acquisition System
   Canberra 512 Counter/Timer
   Lecroy Waveruuner 204X1 oscilloscope
   Discriminator
   Power supply

2. Turn on the blackbody source according to the steps in Appendix C. Turn on the TEC source meter, Electrometer and oscilloscope, witch on the power supply for amplifier and discriminator.
   A. For temperature control, the device temperature sensor type need to be checked and selected in the settings of the TEC source meter. The accurate control based on the right settings. The main operation steps are listed below
      i) Choose T : Temperature function
      ii) Press CONFIG then T to set the following operating parameters:
      PROTECTION: Enable protection, set a high temperature and low temperature point
      SENSOR TYPE: Thermistor → A = 1.1832139e-3 B = 2.33894E-4 C = 2.8919496E-7
      UNITS: Select ^{o}C
      PID: use default setting
      iii) Set current limit: Press CONFIG then I, set the value below 1.4 A

iv) Adjust set point: Use the ▲ and ▼ keys to increment and decrement set point values, set the temperature at 20 ^{o}C

v) Turn output on/off: Press ON/OFF output key

This is given by fitting the thermistor value of detector using the equation below

$$\frac{1}{T} = A + B[lnR_t] + C[lnR_t]^3$$

where the R_t is the thermistor value and the fitting results is shown in figure D.1.

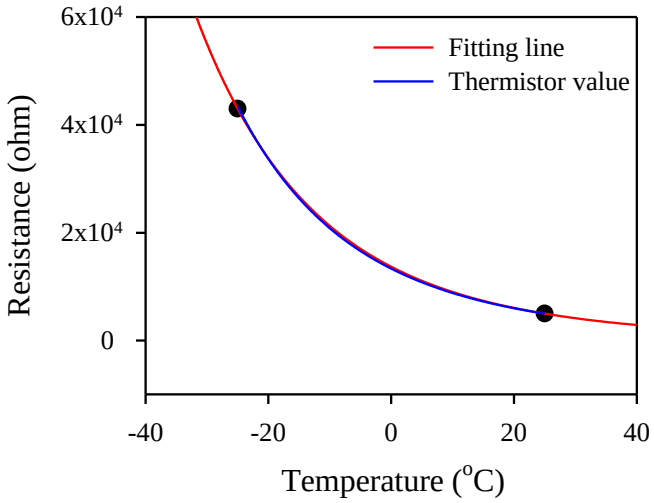

Figure D.1 Thermistor value and fitting result of Si SPAD

B. For high bias operation, the settings of Electrometer is listed

i) V-source configuration: Press CONFG then OPER (or▲ or ▼)

ii) Choose RANGE: Select V-Source range (1000 V)

iii) Press ENTER then EXIT

iv) Press OPER to turn on voltage source, using ▲ and ▼ to increment and decrement set point values

3. Using Oscilloscope to monitor the avalanche pulse. Once the avalanche pulse with amplitude of 1 mV appears (before amplified), turn on the counter to do the counting measurement. The multimeter can connect to the discriminator to monitor the voltage threshold. A small screw driver is used to adjust threshold voltage during the measurement. Before do the counting measurement, adjust threshold voltage and monitor the NIM signal generated from discriminator using oscilloscope and make sure all the avalanche pulse is detected.

A. To use Counter:

i) Input programming mode:
MODES+PROG INPUTS→ CHSEL/SCROLL→choose 2:ctr2A (if channel 2) →CHSEL/ENTER
Set pola→CHSEL/ENTER→CHSEL/SCROLL→choose Neg (-) →CHSEL/ENTER→CHSEL/SCROLL
Adjust Thre→CHSEL/ENTER→ -0.25 V (could modify)→CHSEL/ENTER→CHSEL/SCROLL→EXIT→CHSEL/ENTER→CHSEL/ENTER→EXIT→CHSEL/ENTER

ii) Preset programming mode:
MODES+PROG PRESET→StdTmr A→CHSEL/ENTER→10.0s →CHSEL/ENTER→ CHSEL/SCROLL→EXIT→CHSEL/ENTER

iii) Start/Stop counting:
COUNT/STOP (start)→ COUNT/STOP (stop) →RESET

B. Threshold voltage setting: 5.3 mV – 8 mV from 208.2 V-210 V (Adjustment due to increased self-sustaining current level)

C. During the measurement, black cloth was used to block the photons from blackbody source when measuring dark count rate.

Appendix E: A Simple Monte Carlo model description

This sections shows a flowchart of SMC program for SPAD simulation.

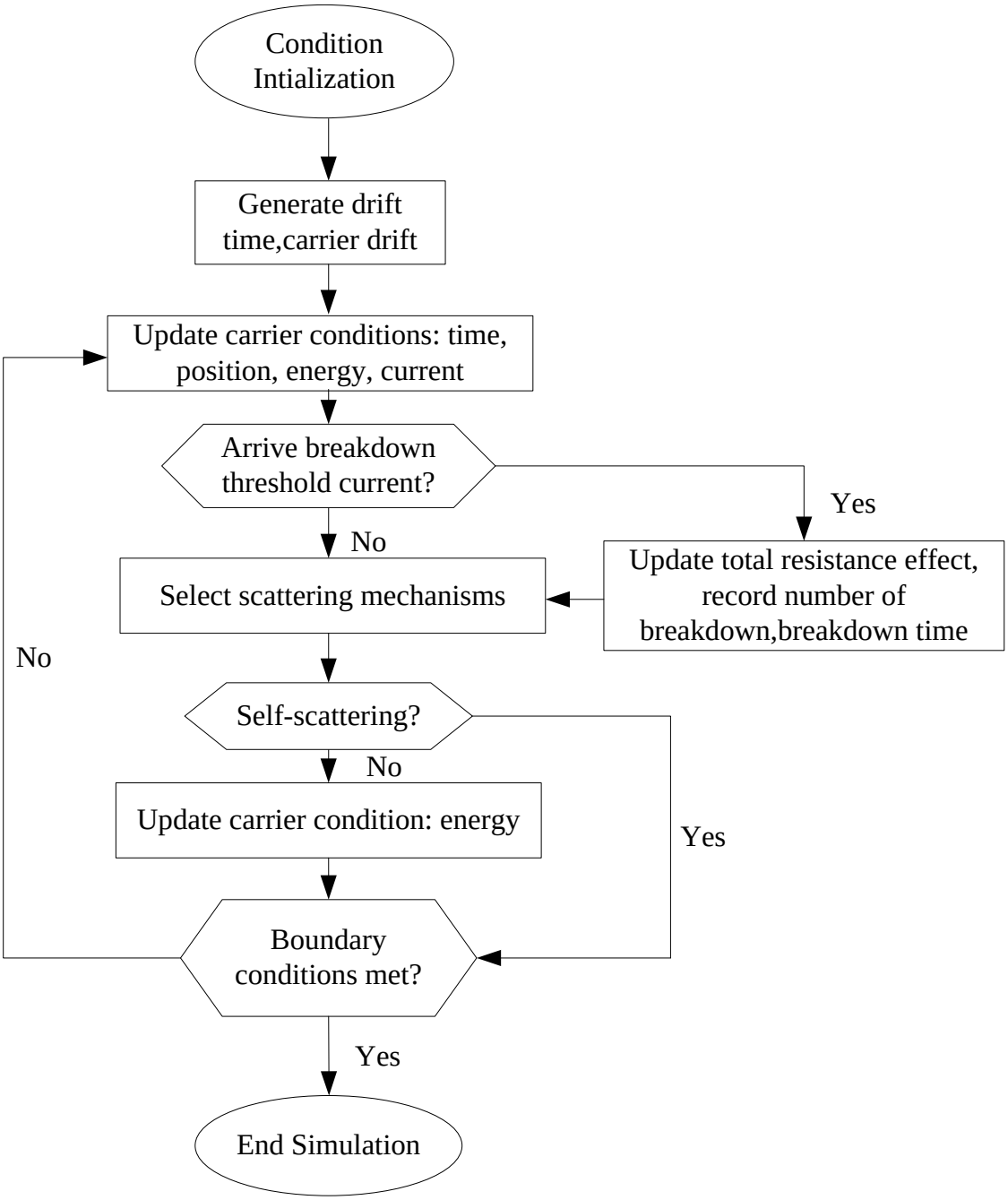

Appendix F: Instructions of monochromator control software

1. Open SynerJy V3.5
2. Collect->Real-Time Control
3. Check "Force Re-initialisation"→OK
4. Monochromator will re-calibrate itself. This process usually will take 1 minute to complete. DO NOT close the program while the hardware reconfigures itself!
5. In "Real-Time Control" window, under "General" Tab, set wavelength to visible light (Recommended 550 nm). Set Entrance slit and exit slit set as 2.0 mm (maximum slit width).
6. Move DUT to the light spot.
7. Depending on the exit used, chose "Lateral" or "Axial" exit option. If chose "Lateral", please set side_exit slit as 2 mm. Set the proper grating which have three options: 1800 g/mm blazed at 400 nm, 600 g/mm blazed at 1000 nm and 300 g/mm blazed at 2000 nm
8. Set position control to the value of DUT peak response wavelength. If necessary, change the grating under "Monos" tab.
9. Optimise the signal by moving the x-y micrometre and then the microscope objective repeatedly, then close "Real-Time Control" window.
10. To measure the device spectral response, click "Collect" then "Experiment Setup" in the menu.
11. Check the grating (under "Mono" tab), slit width, and set integration time at least 3 times of time constant in LIA (under "Detector" tab). Also enter the start, stop wavelength and increment.
12. Click "Run" button and a scan window will pop up. Wait till the scan finishes. Abort the scan by clicking "Abort" button. After scan finishes, define a project name during first scan, a default data window appears.
13. Choose "Data" tab, go to menu and click "File"→Export→ASCII, define a file name and file type